


Fall 2014

Computational study of sodium magnesium hydride for hydrogen storage applications

Fernando Antonio Soto Valle
Louisiana Tech University

Follow this and additional works at: <https://digitalcommons.latech.edu/dissertations>

 Part of the [Chemical Engineering Commons](#), and the [Nanoscience and Nanotechnology Commons](#)

Recommended Citation

Soto Valle, Fernando Antonio, "" (2014). *Dissertation*. 219.
<https://digitalcommons.latech.edu/dissertations/219>

This Dissertation is brought to you for free and open access by the Graduate School at Louisiana Tech Digital Commons. It has been accepted for inclusion in Doctoral Dissertations by an authorized administrator of Louisiana Tech Digital Commons. For more information, please contact digitalcommons@latech.edu.

**COMPUTATIONAL STUDY OF SODIUM MAGNESIUM
HYDRIDE FOR HYDROGEN STORAGE
APPLICATIONS**

by

Fernando Antonio Soto Valle, B.S., M.S.

A Dissertation Presented in Partial Fulfillment
of the Requirements of the Degree
Doctor of Philosophy

COLLEGE OF ENGINEERING AND SCIENCE
LOUISIANA TECH UNIVERSITY

November 2014

UMI Number: 3662479

All rights reserved

INFORMATION TO ALL USERS

The quality of this reproduction is dependent upon the quality of the copy submitted.

In the unlikely event that the author did not send a complete manuscript and there are missing pages, these will be noted. Also, if material had to be removed, a note will indicate the deletion.



UMI 3662479

Published by ProQuest LLC 2015. Copyright in the Dissertation held by the Author.

Microform Edition © ProQuest LLC.

All rights reserved. This work is protected against unauthorized copying under Title 17, United States Code.



ProQuest LLC
789 East Eisenhower Parkway
P.O. Box 1346
Ann Arbor, MI 48106-1346

LOUISIANA TECH UNIVERSITY

THE GRADUATE SCHOOL

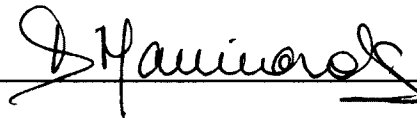
SEPTEMBER 17, 2014

Date

We hereby recommend that the dissertation prepared under our supervision by
Fernando Antonio Soto Valle, B.S., M.S.

entitled Computational Study of Sodium Magnesium Hydride for Hydrogen
Storage Applications

be accepted in partial fulfillment of the requirements for the Degree of
Doctor of Philosophy in Engineering



Supervisor of Dissertation Research

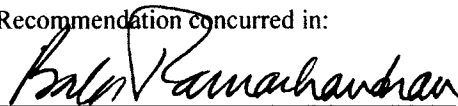


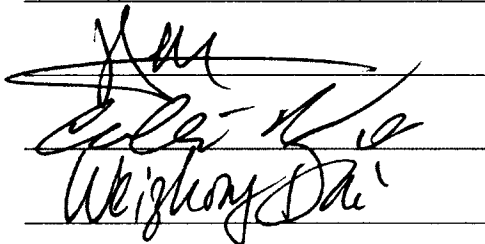
Head of Department

ENGINEERING

Department

Recommendation concurred in:






Advisory Committee

Approved:

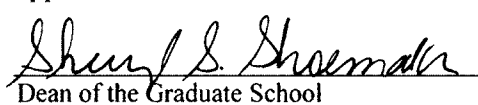


Director of Graduate Studies



Dean of the College

Approved:



Dean of the Graduate School

ABSTRACT

Hydrogen offers considerable potential benefits as an energy carrier. However, safe and convenient storage of hydrogen is one of the biggest challenges to be resolved in the near future. Sodium magnesium hydride (NaMgH_3) has attracted attention as a hydrogen storage material due to its light weight and high volumetric hydrogen density of 88 kg/m^3 . Despite the advantages, hydrogen release in this material occurs at approximately 670 K, which is well above the operable range for on-board hydrogen storage applications. In this regard, hydrogen release may be facilitated by substitution doping of transition-metals. This dissertation describes first-principles computational methods that enable an examination of the hydrogen storage properties of NaMgH_3 . The novel contribution of this dissertation includes a combination of crystal, supercell, and surface slab calculations that provides new and relevant insights about the thermodynamic and kinetic properties of NaMgH_3 .

First-principles calculations on the pristine crystal structure provide a starting reference point for the study of this material as a hydrogen storage material. To the best of our knowledge, it is reported for the first time that a 25% mol doping concentration of Ti, V, Cu, and Zn dopants reduce the reaction enthalpy of hydrogen release for NaMgH_3 . The largest decrease in the $\Delta H(298 \text{ K})$ value corresponds to the Zn-doped model ($67.97 \text{ kJ}/(\text{mol H}_2)$). Based on cohesive energy calculations, it is reported that at the 6.25% mol doping concentration, Ti and Zn dopants are the only transition metals that destabilize the

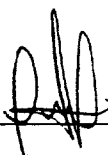
NaMgH₃ hydride. In terms of hydrogen removal energy, it is quantified that the energy cost to remove a single H from the Ti-doped supercell model is 0.76 eV, which is lower with respect to the pristine model and other prototypical hydrogen storage materials. From the calculation of electronic properties such as density of states, electron density difference, and charge population analysis schemes it is shown that the effectiveness of these two dopants is due to the modified chemical bonding induced by the overlap of *d* orbitals.

For the surface slab calculations, a key finding is that the preferred layer for the simultaneous substitution of Ti and Zn dopants at two different Na sites is the outermost layer with substitution energy values of -5.27 eV and -5.24 eV, respectively. The kinetic barrier for hydrogen desorption from the (001) surface is studied using DFT calculations, LST/QST, and NEB methods. We find that for the pristine model, the direct recombination of a H₂ molecule has a kinetic barrier of 1.16 eV. More importantly, we find that the calculated kinetic barrier of H₂ desorption when the (001) surface is co-doped with Ti and Zn is 0.42 eV. These results show that the combined use of a Ti dopant and a Zn dopant is the best mix for reducing the energy barrier to release hydrogen from the (001) NaMgH₃ surface.

APPROVAL FOR SCHOLARLY DISSEMINATION

The author grants to the Prescott Memorial Library of Louisiana Tech University the right to reproduce, by appropriate methods, upon request, any or all portions of this Dissertation. It is understood that "proper request" consists of the agreement, on the part of the requesting party, that said reproduction is for his personal use and that subsequent reproduction will not occur without written approval of the author of this Dissertation. Further, any portions of the Dissertation used in books, papers, and other works must be appropriately referenced to this Dissertation.

Finally, the author of this Dissertation reserves the right to publish freely, in the literature, at any time, any or all portions of this Dissertation.

Author  _____

Date 11/10/2014

DEDICATION

This dissertation is dedicated to my beloved parents, Lizeth De Soto and Fernando Soto Ferrera; to Ricardo Soto, my brother; to my grandparents: German Valle, Irma De Valle, Aida Ferrera, and Fernando Soto Henriquez; to my close family: Rosario Gonzalez-Cruz and Pedro Gonzalez; to Claudia Vides; and to all my family that has made the completion of this dissertation possible.

TABLE OF CONTENTS

ABSTRACT.....	iii
LIST OF TABLES.....	x
LIST OF FIGURES.....	xii
ACKNOWLEDGMENTS.....	xvii
CHAPTER 1 INTRODUCTION.....	1
1.1 Hydrogen as an Energy Vector.....	1
1.2 Solid-State Hydrogen Storage.....	7
1.2.1 Complex Metal Hydrides.....	7
CHAPTER 2 BACKGROUND.....	10
2.1 Sodium Magnesium Hydride.....	12
2.2 Transition-Metals as Doping Agents.....	16
2.2.1 Ti as Doping and Co-Doping Agent.....	17
2.2.2 Transition-Metal Doping at the Surface Level.....	18
2.3 Summary.....	21
2.3.1 Objectives.....	22
CHAPTER 3 THEORY AND SIMULATION DETAILS.....	25
3.1 Many-Body Equation.....	26
3.2 Density Functional Theory.....	27
3.2.1 First Approximations.....	27
3.2.2 Hohenberg-Kohn Theorems.....	27
3.2.3 Kohn-Sham Method.....	28

3.2.4	Exchange and Correlation Functional in DFT	31
3.2.5	Finding the Ground-State Energy	33
3.3	Periodic Systems.....	34
3.3.1	Bravais Lattice	34
3.3.2	Plane-Wave Basis Set	35
3.3.3	Atomic Pseudopotential Approximation.....	36
CHAPTER 4 DFT STUDY OF SODIUM MAGNESIUM HYDRIDE		55
4.1	Results.....	55
4.1.1	Geometry of Pristine NaMgH ₃ Crystal	55
4.1.2	Geometry of Modified-NaMgH ₃ Crystal	58
4.1.3	Electronic Structure of Pristine NaMgH ₃	61
4.1.4	Lattice Vibrations.....	64
4.1.5	Mechanical Stability	68
CHAPTER 5 DFT STUDY OF DOPANT EFFECT		74
5.1	Results.....	74
5.1.1	TM-doped NaMgH ₃ Crystal	74
5.1.2	TM-doped NaMgH ₃ Supercell.....	79
5.2	Summary	96
CHAPTER 6 DFT STUDY OF MODIFIED (001) SURFACE		99
6.1	Results.....	99
6.1.1	Single Dopant.....	99
6.1.2	DFT coupled Molecular Dynamics (DFT-MD).....	106
6.1.3	Hydrogen Removal Energy.....	110
6.1.4	Strain Effect on (001) NaMgH ₃ Surface	115
6.1.5	The Stability of Co-dopants at the (001) NaMgH ₃ Surface.....	119

6.1.6	Dehydrogenation Kinetics at the (001) NaMgH ₃ Surface	121
6.2	Summary	127
CHAPTER 7 CONCLUSIONS AND FUTURE WORK.....		131
7.1	Conclusions.....	131
7.2	Future Work.....	139
REFERENCES		141

LIST OF TABLES

<p>Table 4-1: Calculated average bond distances and lattice parameters for pure NaMgH₃, MgH₂, NaH, and KMgH₃ at the GGA-PBE theory level. Experimental information for NaMgH₃ based on Deuterium is given in parenthesis. Distance for K-Mg shown with a (*) was reported by Reshak <i>et al.</i> [21]. Experimental distances for Mg-H and Na-H bonds are taken from ref. [4]. The experimental lattice parameters are taken from Klaveness <i>et al.</i> [20].</p>	58
<p>Table 4-2: Average Hirshfeld charges of individual atoms as a function of hydrostatic pressure as obtained from DFT calculations on a NaMgH₃ crystal structure. The 0 GPa row represents the values calculated for the ground-state structure. DFT calculations are performed at the GGA-PBE theory level.</p>	60
<p>Table 4-3: Calculated elastic constants for the NaMgH₃ unit cell. Elastic constants reported by Bouhadda <i>et al.</i> [169] are listed in parentheses for comparison with the calculated values in this dissertation.</p>	69
<p>Table 4-4: Calculated Bulk and Shear Modulus for the NaMgH₃ unit cell. The calculations are calculated following the Voigt-Reuss-Hill scheme.</p>	69
<p>Table 4-5: Young's Modulus for the NaMgH₃ unit cell along its principal axes.</p>	70
<p>Table 4-6: Poisson Ratios for the NaMgH₃ unit cell along principal axes.</p>	70
<p>Table 5-1: Calculated average bond distances, lattice parameters, and cell volume for pristine NaMgH₃ and 3d TM-doped NaMgH₃ crystal models at the GGA-PBE theory level and 25% mol doping concentration.</p>	76
<p>Table 5-2: Cohesive energy per atom for the pristine and 3d-TM doped NaMgH₃ supercell.</p>	81
<p>Table 5-3: Mulliken population analysis for the TM-doped NaMgH₃.</p>	84
<p>Table 5-4: Calculated average bond lengths, point-defect energies, and hydrogen removal energies for pristine, Na-vacancy, Mg-vacancy, and Ti-doped Na₁₆Mg₁₆H₄₈ models are presented at the GGA-PBE theory level.</p>	94

Table 6-1: Average distances for the nearest neighbors for pristine and TM-doped (001) NaMgH ₃ surface models. In addition, the average Hirshfeld charges are also listed in this table.	103
Table 6-2: Hydrogen Removal Energy (ΔE_{HR}) for the strained and Ti-doped (001) surface models.	118

LIST OF FIGURES

Figure 1-1: Clean, environmentally-friendly cycle of the hydrogen-based fuel economy. In this economy, hydrogen is used as an energy carrier to replace fossil-based fuels and to sustain an infrastructure which includes hydrogen production, storage, and delivery [4].	3
Figure 1-2: Schematic design of a PEM fuel cell [6].....	4
Figure 1-3: Position of different fuels relative to volumetric energy density (MJ/L) and gravimetric energy density (MJ/kg) for several fuels [10].	6
Figure 1-4: Status of promising solid-state hydrogen storage technologies with revised DOE system targets as a function of volumetric and gravimetric hydrogen storage capacity [10].	9
Figure 2-1: Side view of the perovskite structure of pristine NaMgH ₃ unit cell containing 20 atoms. The visualization style of the NaMgH ₃ crystal employs a CPK display style with a 0.5 value [33]. Spheres colored purple (large), green (medium), and gray (small) denote Na, Mg, and H atoms, respectively. Same color convention and visualization technique are applied throughout the dissertation. For the crystal structures shown in this dissertation, atoms are made visible according to the center of geometry of the connected sets of atoms, that is, complete molecules are shown. This type of visualization method is suitable for crystalline structures.	11
Figure 2-2: Side view of the perovskite structure of a pristine KMgH ₃ unit cell. The crystal structure contains 1 formula unit of KMgH ₃ . The additional atoms in the unit cell are used to represent the crystalline nature of the material. Spheres colored pink (large) denote potassium atoms.	12
Figure 3-1: The external potential of many-particle system is determined by the electronic density, which is a function of the position, thus, the energy is a functional of the density [95, 96].....	27
Figure 3-2: Perdew's "Jacob's Ladder" of density functional approximations. This is a strategy to construct improved density functionals for the exchange-correlation energy. Notice that LDA and GGA are placed at the first and second rung in Perdew's "Jacob's Ladder," respectively [110].....	31

Figure 3-3: Schematic drawing of the atomic pseudo-potential approximation. The potential near the core electrons is replaced by a pseudopotential with smoother pseudo-wave functions with no nodes inside the cutoff radius [122].	37
Figure 3-4: Side view of the optimized four-layer (001) NaMgH ₃ surface slab consisting of 80 atoms. A vacuum slab (15 Å) normal to the surface is added to avoid interactions with periodic image in this direction. Here, purple, green, and grey spheres denote Na, Mg, and H atoms, respectively.....	47
Figure 3-5: Relaxed two-layer surface slab consisting of 40 atoms. Here, the red sphere represents the TM dopant.....	48
Figure 3-6: Schematic drawing of a TS search using the LST/QST algorithm [156].	51
Figure 4-1: Front view of the crystal structure of pure MgH ₂	56
Figure 4-2: Front view of the optimized structure of the NaH crystal structure.....	57
Figure 4-3: Average bond lengths in NaMgH ₃ as a function of hydrostatic pressure. Here, unit cell volume change vs. hydrostatic pressure is also shown. Results are calculated at the GGA-PBE theory level.	59
Figure 4-4: From bottom panel to top panel: Total DOS for NaMgH ₃ and PDOS for H, Mg, and Na atoms. Black solid and dotted lines represent <i>s</i> and <i>p</i> states, respectively.....	62
Figure 4-5: Electron density map for the NaMgH ₃ crystal. Electron rich zones and electron deficient zones are depicted in red and blue, respectively.	63
Figure 4-6: Calculated total phonon DOS for NaMgH ₃ crystal.	65
Figure 4-7: Calculated thermodynamic functions NaMgH ₃ as a function of temperature. The functions include the Free energy (top-left panel), enthalpy (top-right panel), entropy (lower-left panel) and heat capacity (lower-right panel).....	66
Figure 5-1: The 25% mol TM-doped perovskite crystal structure of NaMgH ₃ containing 20 atoms. The red sphere represents the TM at the Na lattice site.	75
Figure 5-2: The Free energies of pristine and TM-doped NaMgH ₃ functions of temperature.....	77
Figure 5-3: Calculated $\Delta H(298\text{ K})$ values for the first decomposition reaction of TM-doped NaMgH ₃ crystal structure. The solid gray line represents the calculated decomposition temperature.	78

Figure 5-4: Supercell NaMgH ₃ model. The yellow sphere represents the substituted Na atom.	80
Figure 5-5: Bond distances of the pristine and TM-doped NaMgH ₃ supercell models. Bond distances reported are for the nearest neighbors.....	82
Figure 5-6: Calculated electron difference plots for TM-doped NaMgH ₃ supercell models. Here the top-left, top-right, bottom-left, and bottom-right panels represent the electron density difference map for the Ti-doped model, Cu-doped model, V-doped model, and Zn-doped model, respectively.....	86
Figure 5-7: From bottom panel to top panel: Total DOS for Ti-doped NaMgH ₃ and PDOS for Ti, H, and Mg atoms.....	88
Figure 5-8: From bottom panel to top panel: Total DOS for V-doped NaMgH ₃ and PDOS for V, H, and Mg atoms.	89
Figure 5-9: From bottom panel to top panel: Total DOS for Cu-doped NaMgH ₃ and PDOS for Cu, H, and Mg atoms.....	90
Figure 5-10: From bottom panel to top panel: Total DOS for Zn-doped NaMgH ₃ and PDOS for Zn, H, and Mg atoms.	91
Figure 5-11: Supercell model for NaMgH ₃ . The replaced Na, and Mg atoms are shown as yellow spheres.....	92
Figure 6-1: The substitutional energies of TM (at Na sites). Black line represents TM-doped at the first layer, gray solid line represents TM-doped in the second layer. The differences between the substitutional energies of TM doped in the first layer, and those doped in the second layer are shown with dotted gray lines.	100
Figure 6-2: (a) Side view of optimized structure of TM-doped (001) NaMgH ₃ surface (b) Detailed structure of Ti-Mg _x -H _y complex in the TM-doped (001) NaMgH ₃ surface. Panels “b1”, “b2”, and “b3” show the geometry of the Ti-Mg ₄ -H ₄ , V-Mg ₅ -H ₄ , and Cu-Mg ₄ -H ₃ complexes, respectively. Panel “b4” shows the nearest neighbors of Zn in the Zn-doped model.	102
Figure 6-3: Electron density difference of (a) early TM-doped (001) NaMgH ₃ surface, and (b) late TM-doped (001) NaMgH ₃ surface. The spatial visualization of the electron density difference of (a) and (b) are taken along the (001) plane. Regions in red and blue represent electron-rich and electron-deficient regions, respectively. The range of the charge display is 0.10 e/Å to 0.20 e/Å. A reversed rainbow color scheme with 16 bands was applied.	105

- Figure 6-4: Snapshots of the Ti-doped (001) NaMgH₃ surface. Panels “a1” (300 K) and “a2” (400 K) show the structural evolution of the Ti-Mg_x-H_y complex as temperature is increased and time evolves. Snapshots “a1” and “a2” are taken at the end of the 4 ps and 8 ps simulations, respectively. Here, the red sphere represents the Ti dopant. Visualization is performed with a 0.2 CPK value..... 108
- Figure 6-5: Snapshots of Zn-doped (001) NaMgH₃ surface. Panels “a1” (300 K) and “a2” (400 K) show the structural evolution of the surface as temperature is increased, and time evolves. Snapshots “a1” and “a2” are taken at the end of the 4 ps and 8 ps simulations, respectively. Here, the red sphere represents the Zn dopant. Visualization is performed with a 0.2 CPK value. 109
- Figure 6-6: GGA-PBE relaxed structure of the pristine (001) NaMgH₃ surface, showing the positions of the H atoms being removed. Here, removed H atoms as H₂ molecules are labeled as H1, H2, and H3. Similarly, removed H atoms as single H atoms are labeled as H4 and H5. Visualization is performed with a 0.2 CPK value. 111
- Figure 6-7: GGA-PBE relaxed structure of the TM-doped (001) NaMgH₃ surface, showing the positions of the H atoms being removed as H₂ molecules. Visualization is performed with a 0.2 CPK value. 112
- Figure 6-8: Hydrogen removal energy values for pristine and TM-doped (001) NaMgH₃ surface models. 113
- Figure 6-9: The Local geometry of the Ti-doped (001) NaMgH₃ surface slab. Here, the color convention is same as previous figures. Red spheres denote the Ti substituted at the surface Na site. Visualization is performed with a 0.2 CPK value..... 115
- Figure 6-10: Total energy curves for the (001) NaMgH₃ surface when it is subjected to different strain percentages. 116
- Figure 6-11: Side view of the optimized structure of the Ti-doped-strained (001) NaMgH₃ surface. Visualization is performed with a 0.2 CPK value..... 119
- Figure 6-12: Side views of possible configurations of co-doped (001) NaMgH₃ surfaces. Here, the top-left, top-right, bottom-left, and bottom-right panels show the Ti₁Zn₂, Ti₁Zn₁, Ti₂Zn₁, and Ti₂Zn₂ configurations, respectively. 120
- Figure 6-13: The substitutional energies of TM co-doped at the NaMgH₃ (001) surface. 121

- Figure 6-14: The minimum energy path for H₂ desorption from a subsurface site at the (001) NaMgH₃ surface. The yellow spheres represent the H atoms. Visualization is performed with a 0.1 CPK value..... 123
- Figure 6-15: The minimum energy path for H₂ desorption from H recombination at the (001) NaMgH₃ surface. The yellow spheres represent the H atoms at the subsurface and the orange spheres represent H atoms at the surface. Visualization is performed with a 0.2 CPK value..... 124
- Figure 6-16: The minimum energy path for H₂ desorption from H recombination at the Ti-doped (001) NaMgH₃ surface. The yellow spheres represent the H atoms that recombine into a H₂ molecule. The red sphere represents the Ti atom. Visualization is performed with a 0.2 CPK value. 125
- Figure 6-17: The minimum energy path for H₂ desorption from H recombination at the Ti/Zn-doped (001) surface of NaMgH₃. The yellow spheres represent the H atoms that recombines into a H₂ molecule. The red sphere represents the Ti atom and the dark blue sphere represents the Zn atom. Visualization is performed with a 0.2 CPK value..... 126

ACKNOWLEDGMENTS

Above all, I would like to thank God for all His blessings.

I thank Dr. Daniela Mainardi for allowing me to be part of her research group at Louisiana Tech University. I am greatly indebted for all her support and guidance at every step of the research program. I would like to acknowledge financial support from the National Science Foundation (NSF) under the following grant: EPSCoR LA-SiGMA project under award #EPS-1003897.

I express my profound gratitude to Dr. Ramu Ramachandran, Dr. Pedro Derosa, Dr. Collin Wick, and Dr. Weizhong Dai for the courses they taught which helped develop my interest in computational materials science. I am grateful for the opportunity to work under the sponsorship of the LA-SiGMA project. I truly believe that this project made a significant impact on my research experience at Louisiana Tech University. I enjoyed participating and collaborating with every LA-SiGMA initiative. Notably, I am grateful for the opportunity to represent Louisiana Tech University at the National EPSCoR competitions.

I take this opportunity to thank all my colleagues at Louisiana Tech University. Particularly, I thank Purnima Kharidehal for all her help during graduate school. I am greatly indebted to Claudia Vides for all her support and continuous encouragement during all these years at Louisiana Tech University. I deeply appreciate her understanding and motivation in all my endeavors.

I would like to thank the Gonzalez-Cruz family, mainly, my aunt Rosario Gonzalez-Cruz for opening the doors of her house and giving me the opportunity to begin my college degree. I would like to thank my uncle Pedro Gonzalez for guiding me throughout my college career and for always being a source of advice.

Last but not least, I would like to thank my grandparents for taking care of me and being with me all my life. I would like to thank my brother Ricardo for his help and support at Louisiana Tech in these last couple of years. I am very grateful with my parents, Lizeth and Fernando Soto Ferrera, for their love and sacrifice. Words cannot express my thanks for the patience and support I have received throughout this process.

I would like to leave reflected in this document a quote attributed to Winston Churchill that I have kept in my memory during this process: "Success is not final, failure is not fatal. It is the courage to continue that counts."

CHAPTER 1

INTRODUCTION

1.1 Hydrogen as an Energy Vector

Fossil fuels have been the greatest energy resource for two centuries, being in the forefront of industrialization and the modernization of human society. However, because of the oil price crises in the 1970s, the need for low-cost energy sources became apparent. The cost of nonrenewable energy resources such as fossil fuels began to grow, and society started to consider a paradigm shift in energy utilization and economization. According to Dr. Arun Majumdar, the first director of the Advanced Research Projects Agency-Energy (ARPA-E), "In the transportation sector, today we have only one option- using gasoline or diesel as the fuel- and thereby we face future vulnerability if we do not diversify our fuel source" [1]. Furthermore, about one-quarter of the world's total energy is used as transportation and heating fuels. Despite recent advances, electricity generated from renewable sources can rarely provide an immediate response to the total energy demand. In addition, the growth of these renewable sources has brought additional problems such as network load stability and intermittent power fluctuations. A possible solution to compensate for this power fluctuation is to use a battery energy storage system. However, batteries cannot be used for storage of large amounts of energy in a small volume.

Therefore, efficient technologies such as fuel cells for on-board transportation are sought to mitigate these problems. In this respect, hydrogen-based fuel cells are making significant progress toward market penetration due to several attractive features such as: high proton conductivity, low permeability to fuel, good chemical/thermal stability, good mechanical properties, and low cost [2].

In addition, waste heat from hydrogen-based fuel cells can be used to supply the required energy for hydrogen release if the operating temperature is approximately 80-90 °C [3]. With this scope, hydrogen offers considerable potential benefits as an energy carrier because the product from operating a hydrogen-based fuel cell is just water, consequently, reducing emissions of pollutants and reducing greenhouse gases. Hydrogen as an energy carrier would help to resolve challenges associated to fluctuating oil supply and rising pollution. As a result, hydrogen is considered to be a key energy carrier and fuel source in the near future. Figure 1-1 represents the environmentally-friendly cycle for a hydrogen-based fuel economy.

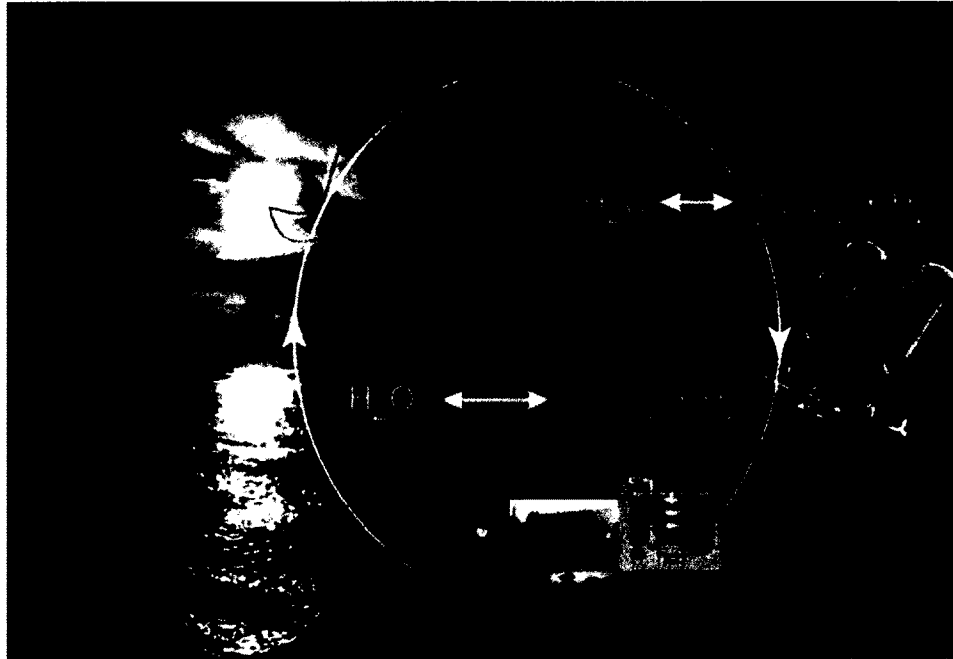


Figure 1-1: Clean, environmentally-friendly cycle of the hydrogen-based fuel economy. In this economy, hydrogen is used as an energy carrier to replace fossil-based fuels and to sustain an infrastructure which includes hydrogen production, storage, and delivery [4].

Given the technological breakthroughs developed in batteries and catalysis, it would be naive to think that the alternative energy would be based solely on hydrogen. However, despite these breakthroughs, hydrogen will still play a significant role. For instance, the proton-exchange membrane (PEM) fuel cells powered by hydrogen are proposed for vehicles where medium and long distance trips are required, with a plug-in battery reserved for short trips [5]. PEM fuel cells use pure hydrogen fuel at the anode and can operate at quite low temperatures (50-100 °C), using a catalyst to increase the reaction kinetics.

The PEM fuel cell utilizes a layer that conducts hydrogen ions from the anode to the cathode, offers high power density, high efficiency, and shows the best potential to meet future automotives high-volume cost requirements.

Figure 1-2 shows the relevant reactions in PEM fuel cells. At the PEM anode (site of oxidation), hydrogen gas ionizes, releasing protons and electrons which travel through an external circuit. Meanwhile, at the cathode site, oxygen molecules are reduced in an acidic environment by electrons from the circuit, forming water molecules after protons traveling through the membrane reach the cathode.

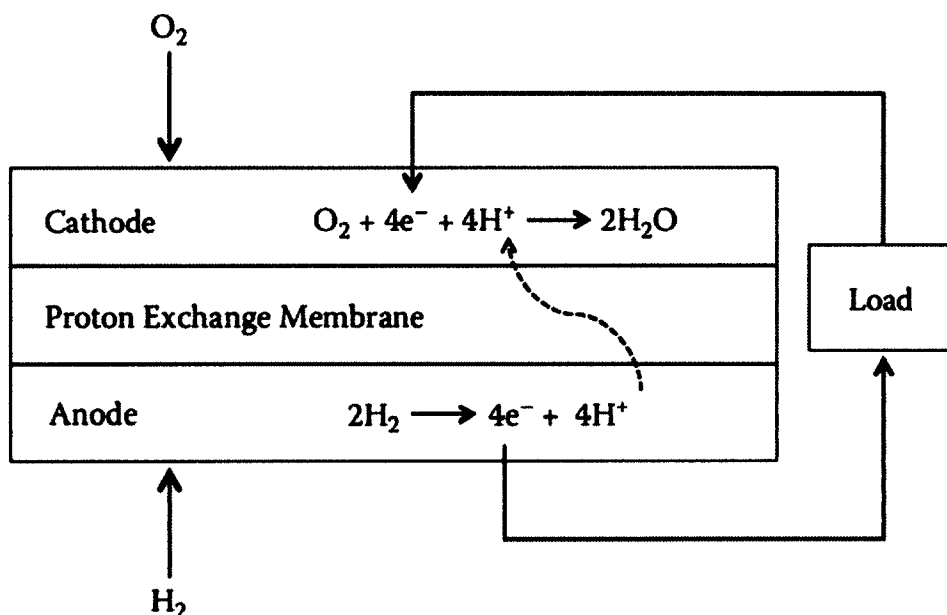


Figure 1-2: Schematic design of a PEM fuel cell [6].

In addition to on-board vehicle applications, the PEM fuel cell is proposed as a micro-power source for micro-systems, such as micro-aerial vehicles, micro-robots, and nano-satellites. However, many obstacles must be overcome to make this option possible. Specifically, storing enough hydrogen (4-10 kg) on-board a vehicle to achieve a driving range greater than 300 miles is a significant challenge. Indeed, the volumetric density of hydrogen is low, namely 0.09 kg/m^3 for H_2 gas; therefore, an unfeasible amount of space is needed to store hydrogen in its gaseous state [7].

Several methods have been considered for on-board hydrogen storage. One of these methods is storing hydrogen in high-pressure containers. However, this storage method leads to many drawbacks (safety concerns, cost of pressurization, hydrogen embrittlement of tank, and sudden drop of pressure during operation) [8]. Due to these drawbacks, pressurized hydrogen in a container is not considered an option for on-board hydrogen storage. Second, another option for storing hydrogen is to keep hydrogen in its liquid state, with a density of 70.8 kg/m^3 at 21 K. However, liquid hydrogen can only exist at the cryogenic condition (between 21-32 K at ambient pressure) [3].

Consequently, a highly insulated tank is required to prevent liquid hydrogen leakage. In addition, the energy needed to cool hydrogen to its liquid state is about one-third of the total energy stored [9]. Therefore, storing liquid hydrogen is not a viable option for on-board hydrogen storage. Figure 1-3 shows the position of compressed and liquid H_2 relative to the gasoline fuel according to their volumetric and gravimetric capacity. From Figure 1-3, it can be noticed that the volumetric energy density of these two methods is significantly lower than that of gasoline [10].

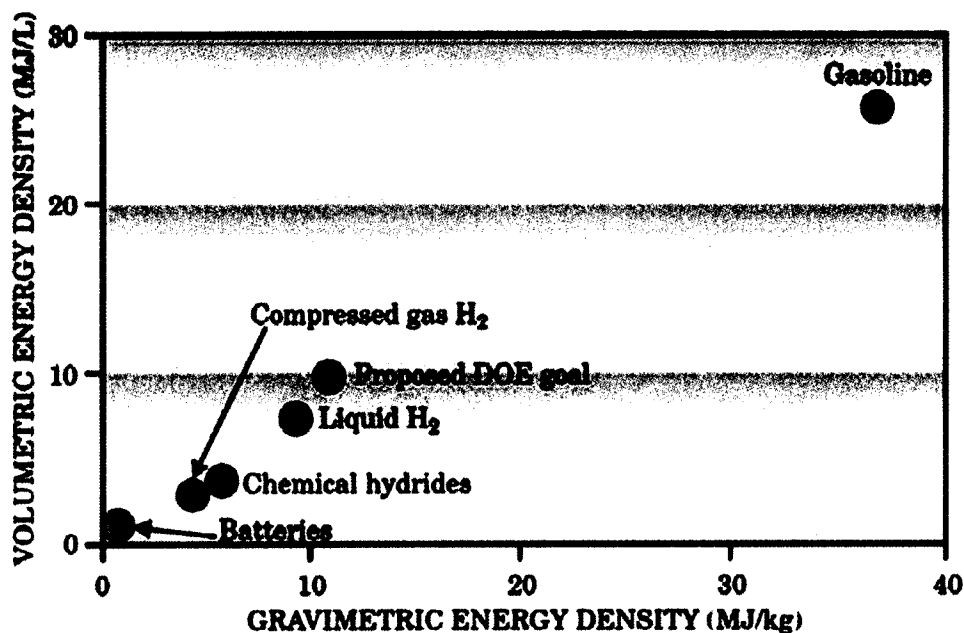


Figure 1-3: Position of different fuels relative to volumetric energy density (MJ/L) and gravimetric energy density (MJ/kg) for several fuels [10].

Major technological breakthroughs in the form of new inventions and discoveries are needed for on-board hydrogen storage to enable a travel range equivalent to that of internal combustion vehicles [11, 12]. For this purpose, significant progress has been made on the development of storage materials for hydrogen-fueled vehicles since the targets were initially established by the United States Department of Energy (US-DOE) in 2003 [13]. The efforts have been focused on the materials-based approach in three main areas. These areas are as follows [14]:

- a) Mechanisms and modeling (provides a computational driven basis for studying new materials).
- b) Materials development (new materials are synthesized and characterized).
- c) System design and materials engineering (provides the information for novel materials to be utilized as practical automotive hydrogen storage systems).

These areas address issues such as gravimetric and volumetric densities, cost, cycle life, refueling rate, and loss of operational hydrogen. The technical targets include 5.5 wt.% hydrogen content and 0.040 kg hydrogen/L in gravimetric and volumetric capacities for the year 2017, respectively [15]. For this reason, research on hydrogen storage is currently extremely thorough in order to find a material that will enable a driving range greater than 300 miles (500 km) for light-duty vehicles, while meeting packaging, safety, cost, and travel range requirements.

Storing hydrogen in solid-state, particularly in complex metal hydrides, is highly desirable due to the high gravimetric and volumetric densities these materials can achieve [16]. Furthermore, a successful solid-state reversible storage material should meet the technical requirements of high hydrogen storage, suitable thermodynamic properties, reversibility, and fast desorption kinetics. To date, no hydrogen storage system has met all the US-DOE targets [17, 18].

1.2 Solid-State Hydrogen Storage

Development of first solid-state hydrogen storage alloys was achieved with the lanthanum-nickel hydride (LaNi_5). LaNi_5 has an attractive value of the equilibrium hydrogen desorption pressure dropping in the range between 1 and 2 atm at 25 °C [8]. However, low hydrogen storage capacity (below 2.0 wt.% hydrogen content) made the application of LaNi_5 as on-board hydrogen storage material unsuccessful [19]. As a consequence of this, research shifted to hydrogen-rich, complex metal hydrides.

1.2.1 Complex Metal Hydrides

Complex metal hydrides are a promising class of hybrid ionic-covalent compounds that can serve as on-board hydrogen storage materials due to their

reversibility and thermodynamic attributes. Here, reversibility is taken as the potential for complex metal hydrides of being capable to be reversed on-board, whereas thermodynamics dictates the reasonableness of the theoretical operating temperature and pressure conditions for hydrogen discharge to be 95-105 °C and 5-3 bar, respectively [20].

However, the widespread use of complex metal hydrides for on-board hydrogen storage applications is limited by their slow kinetics and high temperatures for hydrogen desorption (exceptions are possible for individual materials) [20, 21]. Despite this bottleneck, complex metal hydrides still hold a dominant position in the race for finding a suitable hydrogen storage material. A breakthrough in the research area is mainly due to the pioneering works of Bogdanovic *et al.* [22-24], where the authors reported that reversibility and enhanced reactivity are achieved by doping alkali-metal aluminum hydrides with a few mol% of Ti compounds. Indeed, TM can act as doping agents and have catalytic effects on light-metal complex hydrides. Moreover, TM dopants can change the thermal and kinetic properties of the material, increasing the reaction rate and lowering reaction temperature.

Figure 1-4 shows promising hydrogen storage materials and their position relative to their volumetric and gravimetric densities [10]. In Figure 1-4, the dashed-line box indicates the ultimate US-DOE target for volumetric and gravimetric densities of hydrogen storage materials.

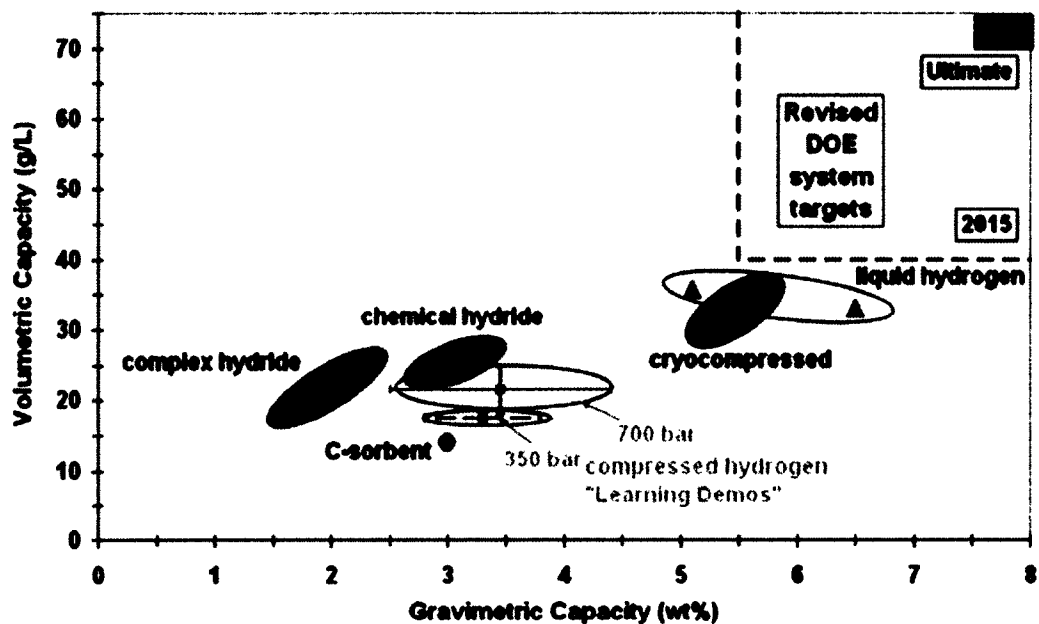


Figure 1-4: Status of promising solid-state hydrogen storage technologies with revised DOE system targets as a function of volumetric and gravimetric hydrogen storage capacity [10].

All plotted materials suffer drawbacks either from high temperatures for hydrogen release, slow kinetics for hydrogen release, or they have a lower gravimetric density compared to the target set by the US-DOE.

CHAPTER 2

BACKGROUND

Complex metal hydrides are of significant importance in the development of an optimal solid-state hydrogen storage system. Among possible complex hydrides, ABH_3 perovskites (where “A” is usually an alkali or alkaline earth metal and “B” is a metal) are being considered as strong candidates for solid-state hydrogen storage systems. Recently, the Mg-based hydrides have attracted attention as hydrogen storage materials. Sodium magnesium hydride ($NaMgH_3$) and potassium magnesium hydride ($KMgH_3$) belong to this type of material. Notably, $NaMgH_3$ has attracted attention as hydrogen storage material due to its light weight, high gravimetric hydrogen density of 6 wt.%, and high volumetric hydrogen density of 88 kg/m^3 [25]. $NaMgH_3$ is a large band gap insulator and the only Mg-based hydride containing sodium atoms [26-28].

Figure 2-1 shows the crystal structure of $NaMgH_3$. The crystal structure of $NaMgH_3$ derives from the cubic $KMgH_3$ structure by an orthorhombic distortion of its MgH_6 octahedral group that gives it a perovskite structure similar to that of $GdFeO_3$. The crystal structure of $NaMgH_3$ belongs to the $Pnma$ #62 space group with orthorhombic symmetry for the 4 to 370 K temperature range [25, 28-30]. Experimental lattice parameters corresponding to the $NaMgH_3$ unit cell are: $a = 5.479 \text{ \AA}$, $b = 7.675 \text{ \AA}$, and $c = 5.399 \text{ \AA}$ [31], Na and Mg atoms occupy the 4c (0.021, 0.250, 0.006) and 4b (0.000, 0.000, 0.500) sites, respectively.

While, H atoms occupy the 4c (0.503, 0.250, 0.093) and 8d (0.304, 0.065, 0.761) Wyckoff positions (these positions belong to a set of points for which site symmetry groups are subgroups of the space group [32]).

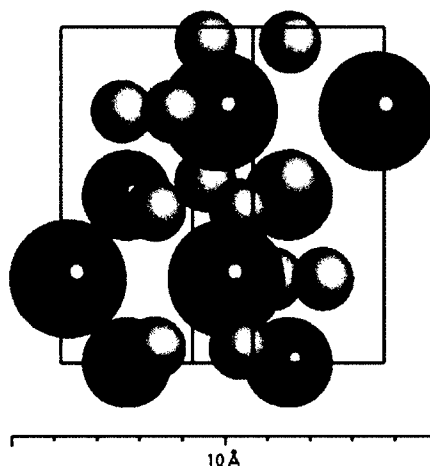


Figure 2-1: Side view of the perovskite structure of pristine NaMgH_3 unit cell containing 20 atoms. The visualization style of the NaMgH_3 crystal employs a CPK display style with a 0.5 value [33]. Spheres colored purple (large), green (medium), and gray (small) denote Na, Mg, and H atoms, respectively. Same color convention and visualization technique are applied throughout the dissertation. For the crystal structures shown in this dissertation, atoms are made visible according to the center of geometry of the connected sets of atoms, that is, complete molecules are shown. This type of visualization method is suitable for crystalline structures.

Similarly, perovskite-type KMgH_3 (Figure 2-2) is attractive as a potential hydrogen storage material due to the presence of lightweight elements and low cost production [34]. For the stable perovskite phase, hydrogen bonds are ionic with potassium and slightly covalent with magnesium. The tilting of the MgH_6 octahedra group is less pronounced in KMgH_3 [34]. KMgH_3 has an ideal cubic perovskite structure belonging to the $Pm\bar{3}m$ #221 space group. This structure contains one formula unit with

the following Wyckoff positions of the atoms: K 1a (0.000, 0.000, 0.000), Mg 1b (0.500,0.500, 0.500), and H 3c (0.000, 0.500, 0.500) [35].

The hydrogen storage properties of these materials are difficult to determine experimentally (thermodynamic and kinetic properties necessary for a viable storage material). Therefore, a computational study is necessary to determine these properties.

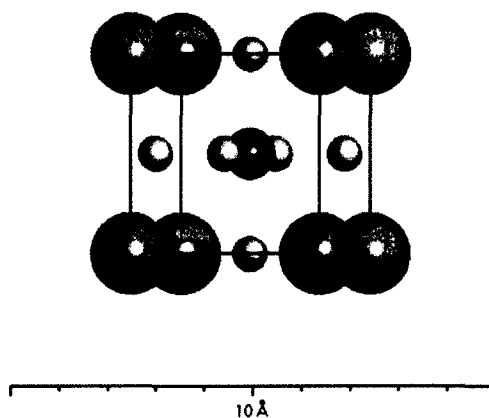


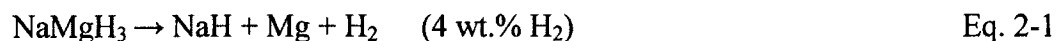
Figure 2-2 : Side view of the perovskite structure of a pristine KMgH_3 unit cell. The crystal structure contains 1 formula unit of KMgH_3 . The additional atoms in the unit cell are used to represent the crystalline nature of the material. Spheres colored pink (large) denote potassium atoms.

In the next sections, a literature review follows covering the relevant topics related to the development of NaMgH_3 as a hydrogen storage material. It is important to note that the literature review and results for KMgH_3 are only presented for comparison purposes.

2.1 Sodium Magnesium Hydride

NaMgH_3 is typically synthesized via reactive mechano-chemical means such as ball milling NaH and MgH_2 in equal mole proportions [36-38]. Hydrogen desorption in this material occurs at approximately 670 K and atmospheric pressure, which is well

above the operable range for on-board hydrogen storage applications. Therefore, NaMgH₃ is more thermally stable than MgH₂, which has a hydrogen dissociation temperature of about 550 K [26]. Possible dehydrogenation routes take place in the following manner:



Similarly, Komiya and co-workers [39] reported the decomposition of KMgH₃ to occur in a one-step reaction in the following manner:



The dehydrogenation kinetics of these materials may be affected by substitution doping (insertion of TM atoms as doping agents) of the crystalline structure. However, in the computational research carried out to date on these perovskite-type hydrides, the effects of zero-valent dopants on the energetics and structural relaxation have not been considered. In addition, full understanding of the hydrogen desorption process is limited due to the complex crystal structure and the difficulties to find the exact positions of hydrogen in these materials.

The reported enthalpy changes for reactions shown in Equation 2-1 and Equation 2-2 have been a source of debate in the literature. Ikeda *et al.* [38] reported the enthalpy change (ΔH) of the reaction shown in Equation 2-1 using van't Hoff plots to be: $\Delta H(298 \text{ K}) = 88 \text{ kJ}/(\text{mol H}_2)$. Similarly, Ikeda *et al.* [38] estimated the standard enthalpy of formation of NaMgH₃ to be -145 kJ/mol. Komiya *et al.* [39] used pressure-composite-isotherms (PCI) measurements at 673 K, 698 K, and 723 K to estimate the standard enthalpy of formation of NaMgH₃ to be $-210 \pm 17 \text{ kJ}/(\text{mol H}_2)$.

The thermodynamics and kinetics of the NaMgH₃ decomposition have been experimentally studied by Sheppard *et al.* [40] utilizing PCI measurements. The authors reported that the ΔH and change of entropy (ΔS) due to decomposition are 86.6 ± 10.0 kJ/(mol H₂) and 132.2 ± 1.3 J/(mol H₂ K), respectively. Reardon *et al.* [41] synthesized NaMgH₃ via reactive milling techniques. With this novel technique, the authors reported that the nano-structured hydride releases hydrogen in two steps with an onset temperature for the first step of 513 K.

Furthermore, Yvon *et al.* [26] reported that NaMgH₃ does not show reversible absorption/desorption kinetics. However, the NMR study performed by Shane *et al.* [36] resulted in the activation energy value of 0.98 eV for hydrogen hopping in NaMgH₃, being much lower in value than the corresponding one reported for pristine MgH₂. This lower activation energy value can explain why NaMgH₃ can be reversibly dehydrated and rehydrated [36, 42]. According to the authors, the reversibility of the reactions shown in Equation 2-1 and Equation 2-2 suggests that hydrogen atoms may be more mobile in NaMgH₃ than in MgH₂, therefore lowering the activation energy for hydrogen release [36, 42].

Density Functional Theory (DFT) [43, 44] calculations conducted by Xiao *et al.* [45] investigated the thermodynamics and electronic properties of Li_xNa_{1-x}MgH₃ ($x = 0, 0.25, 0.50, \text{ and } 0.75$). The authors suggested that Li substitution in NaMgH₃ may result in a favorable modification for on-board hydrogen storage applications. The NMR study by Shane *et al.* [36] suggests that imperfections in the NaMgH₃ crystal formed during the synthesis process are responsible for the crystal disorder that enhances hydrogen mobility. Wu *et al.* [29] reported similar findings on the crystal structure of NaMgH₃,

where the study is based on neutron powder diffraction, neutron vibrational spectroscopy, and quantum mechanical calculations. Besides reporting this similarity, Wu and co-workers [29] also suggested that an increase in the concentration of hydrogen vacancies caused by the substituting dopant (Li) can also increase the hydrogen migration, hydrogenation kinetics, and act as a destabilizing precursor for other metal hydrides.

Furthermore, Hao *et al.* [46] presented a theory-guided computational study explaining the existence of intrinsic defects in NaMgH₃. The authors reported that Schottky defects are the dominant defects in this material and that hydrogen diffusion is determined by the mobility of Schottky defects. Hao and co-workers [46] concluded that the diffusion induced by Schottky defects can be tweaked by adding suitable dopants such as Cu and Co that can adjust the Fermi level of the material. Recently, Hao and Sholl *et al.* [47] performed first-principles calculations on NaMgH₃ doped with C, Al, Si, Sc, Ti, V, Cr, Mn, Fe, Co, Ni, Cu, Ge, Zr, Nb, Mo, and Sn to enhance the hydrogen diffusion in this material. The authors found that Co can act as *n*-type dopant that increases the concentration of negatively charged interstitial H atoms, resulting in a dramatic increase in net diffusivity. However, it is also recognized that these dopants could play other roles in enhancing hydrogen desorption and uptake in this material [47]. Moreover, from first-principles calculations, Miwa *et al.* [48] have proposed that partial substitution of alkaline cations with more electronegative elements may be an effective way of lowering the dehydrogenation temperature of complex metal hydrides. Therefore, creating a neutral-alkali vacancy and introducing a metal dopant should be an effective way to destabilize the ionic-covalent compound [49].

It is important to note that the formation of NaCl has been observed during ball milling of NaAlH₄ with TiCl₃; consequently, Na vacancies can be created during the doping process [50]. In addition, Majzoub and Gross *et al.* [51, 52] have reported that Ti is dispersed in NaAlH₄, both as a substitute ion and perhaps as TiAl₃. Such a dispersed structure is consistent with x-ray diffraction studies, suggesting that Ti be substituted into bulk NaAlH₄. It is important to remark that there has been a discrepancy in the literature regarding which dopants are more active for hydrogen desorption kinetics. A study by Anton and co-workers [53] reported that early TM (Sc, Ti, and V) have better-catalytic effect for NaAlH₄ hydrogen desorption kinetics than late TM (Cu and Zn).

2.2 Transition-Metals as Doping Agents

Ti and Ti salts have been the preferred doping agents for complex metal hydrides since Bogdanovic *et al.* [22] demonstrated the reversibility of sodium alanates with these dopants. For MgH₂, Song *et al.* [54] used a plane-wave DFT method to calculate the electronic structure of the material doped with 20% mole fraction of elements such as Al, Ti, Fe, Ni, Cu, and Nb, and found that these alloying elements could enhance the dehydrogenation properties of MgH₂. Vegge and co-workers [55] found that the TM belonging to the 3*d* block of the periodic table are the most catalytically active for H₂ dissociation. However, the authors concluded that it would not be possible to solve both the slow desorption kinetics and the lower hydrogen desorption temperature of MgH₂ by doping it with single TM. Furthermore, Novaković *et al.* [56] studied Ti and Co doping of MgH₂ utilizing periodic DFT calculations and found that TM bonding with H atoms is stronger than the Mg-H bond.

Despite the use of Ti and Ti salts in other promising materials such as MgH_2 , it still has not met all of the requirements set for on-board hydrogen storage, mainly due to their high dissociation temperature [57, 58]. Hence, the search of an appropriate doping agent and a complex metal hydride capable of meeting the US-DOE targets (5.5 wt.% hydrogen content and 0.040 kg hydrogen/L by the year 2017) is still open [4].

2.2.1 Ti as Doping and Co-Doping Agent

Previous experimental and theoretical studies have shown that Ti is the doping agent that most efficiently increases the dehydrogenation rates. However, the role of the Ti dopant is still poorly understood in prototype complex metal hydrides. In the literature, there has been a discrepancy on the location of Ti in sodium alanates. For instance, in some experiments, Ti has been found to remain on the surface, and in others, Ti has occupied the bulk Na lattice site. In fact, this ambiguity of the dopant position is not exclusive to Ti and NaAlH_4 , it has also been seen for other TM and another prototype complex metal hydride materials such as LiAlH_4 [59]. In addition to this, a discrepancy also arises regarding the best way to dope complex metal hydrides with Ti (nano-cluster, oxides, and metallic).

For instance, Ti salts and Ti compounds such as TiF_3 , TiO_2 , and TiH_2 have been used as catalysts to reduce the hydrogen desorption temperature of MgH_2 [60-62]. Meanwhile, Ti metal powder, Ti nano-particles, and Ti colloids have also been shown to be an effective catalyst for NaAlH_4 [63]. Bogdanovic and co-workers [22] used $\beta\text{-TiCl}_3$ as the Ti precursor material for the doping agent. According to Ismail *et al.* [61], the catalytic activity of TiF_3 is due to in-situ formation of a microcrystalline intermetallic Ti-Al phase from TiF_3 and NaAlH_4 during ball milling or the dehydrogenation process.

Once formed, the Ti-Al phase acts as a real catalyst in the MgH_2 - NaAlH_4 - TiF_3 composite system.

Moreover, Wang and co-workers [64] revealed that Ti is dispersed in NaAlH_4 as a substitute ion by the highly exothermic formation of sodium halides; this structure is consistent with x-ray diffraction studies suggesting that Ti may be substituted into bulk NaAlH_4 . Majzoub and Gross *et al.* [51, 52] have reported that Ti is dispersed in NaAlH_4 , both as a substitute ion and perhaps as a TiAl_3 alloy. Suttisawat *et al.* [62] used TiO_2 as a co-dopant with HfCl_4 to improve the hydrogen desorption/absorption properties of NaAlH_4 . The authors explained that the high porosity and large surface area of the co-dopants would decrease the segregation of bulk Al. Kang *et al.* [63] reported that for NaAlH_4 , direct metallic Ti-doping possesses a practical advantage over other doping technologies due to the elimination of the inactive byproducts and the gas impurities that are highly detrimental to the fuel cell operation.

2.2.2 Transition-Metal Doping at the Surface Level

A study addressing the effects of TM at the surface is essential in order to achieve a deeper understanding of the relevant mechanisms that could facilitate hydrogen desorption in complex metal hydrides. Although the hydrogen storage challenge cannot be solved solely from a quantum mechanical perspective, much can be learned by focusing on trends and generalities. For example, determining the energy of hydrogen desorption from a particular surface plane can easily set a ceiling on the hydrogen removal energy, that is, establish the maximum energy cost for dehydrogenation regardless of the decomposition pathway. Despite the promising role of NaMgH_3 for the

storage of hydrogen, an understanding of the effect of modifying the surface of NaMgH_3 is still lacking.

The stability of the TM-doped hydrides is rarely verified so as to know whether they prefer to replace the host metal from the surface or subsurface layers. For the experimental work, it is noteworthy to mention that the performance of TM-doped hydrides is highly dependent on preparation conditions (milling atmosphere, milling time, and heating of solid) [65-67]. Furthermore, as mentioned previously, Vegge and co-workers [55] concluded that it would not be possible to solve both the slow desorption kinetics and the lower hydrogen desorption temperature of MgH_2 by doping it with single TM. Thus, the use of co-dopants is considered as a possible solution to create synergistic effects that would improve the hydrogen storage properties of complex metal hydrides. Wang and co-workers [68] performed a systematic analysis effect of co-dopants on the dehydrogenation kinetics of freshly doped and ball milled NaAlH_4 samples with chlorides of Ti, Zr, and Fe as the catalysts. The authors reported that the dehydrogenation kinetics improves with the addition of Ti in a co-doped sample, whether it is a binary or ternary system.

Moreover, experimental and computational studies have addressed the possibility of improving hydrogen storage properties through strain engineering [69-71]. Tang and co-workers [72] investigated the biaxial strain effects on MgH_2 and proposed that the biaxial strain tuned dehydrogenation could provide a route for improving the efficiency of the Mg-H system. This destabilization strategy is also attractive because it can solve some of the drawbacks produced by TM doping: i) no addition of weight to the overall hydride system; consequently, the hydrogen capacity is not reduced, and ii) no production

of toxic byproducts [71]. It is important to note that no study on the effect of strain or co-dopants on NaMgH₃ is available in the literature.

Furthermore, for hydrogen storage applications, an enthalpy of dehydrogenation near 40 kJ/(mol H₂) is sought, assuming a ΔS value in the range of about 120 J/(K mol H₂) [73]. It is interesting to note that for a hydride with an equilibrium pressure of 1 atm, a 10 kJ/(mol H₂) variation in ΔH results in about an 80 K change in the decomposition temperature [14]. It is necessary to remark that the activation energies (E_a) values for hydrogen release from complex metal hydrides are typically ≥ 100 kJ/(mol H₂), but dopants such as TM can reduce this energy barrier (to tens of kJ/mol) [74-77].

Recently, there have been studies devoted to the dehydrogenation barriers on complex metal hydrides. However, attention has been mainly focused on MgH₂ and NaAlH₄ systems [78-80]. Here, due to its similarity with NaMgH₃, some results on hydrogen desorption from MgH₂ are reported. For instance, experimental data on the activation barrier for H₂ desorption from pure MgH₂ range from 145 to 323 kJ/(mol H₂) [78]. Wu *et al.* [81] performed a first-principles calculation on a (110) MgH₂ surface slab and reported activation energies in the range between 1.58 eV and 1.64 eV for H₂ recombination. The authors concluded that the rate-controlling step is a recombination of H₂ on the MgH₂ surface. Similarly, Tsuda *et al.* [82] conducted a computational investigation of H₂ desorption from a MgH₂ cluster. The authors reported a substantial activation barrier of 3.30 eV for H₂ desorption. The authors linked this high activation barrier to the strength of the Mg-H bond. Also, Du *et al.* [83] employed first-principles calculations to study the low-index (001) and (110) MgH₂ surfaces. The authors found

that the desorption barriers vary depending on the specific H atom sites involved. Nonetheless, the desorption barrier for H₂ recombination is high (172 kJ/(mol H₂)).

Regarding the use of TM as doping agents, Hanada *et al.* [84, 85] investigated the catalytic effect of TM and some metal oxides in the form of nano-particles on the hydrogen storage properties of MgH₂. They suggested that the main reason for using nano-particle additives is to make the catalysts distribute homogeneously on the surface of MgH₂ and reduce the milling time to avoid severe internal strains. In addition, computational studies by Li *et al.* [86] and Dai *et al.* [87] also showed weakening of the local Mg-H bonds upon TM doping. Wang *et al.* [78] used *ab-initio* studies to obtain the hydrogen desorption barrier from a (110) MgH₂ surface upon Ti doping. The authors reported that a single Ti substitution impurity can effectively lower the kinetic energy barrier by 0.41 eV and the catalytic effect of Ti dopant comes from the concerted atomic processes of synchronized bulk H diffusion and H₂ surface desorption.

It is important to note that no theoretical calculations have been performed for NaMgH₃ to illustrate the mechanism of hydrogen desorption from the (001) surface. These calculations are crucial since the exact mechanism for H₂ desorption is unclear. This H₂ desorption mechanism is complicated since it involves surface desorption, bulk diffusion, metal nucleation, and interface migration [78].

2.3 Summary

Several conclusions are drawn from the literature presented. Hydrogen storage properties (thermodynamics and kinetics) may be improved by modifying the crystalline structure of NaMgH₃. Consequently, there has been considerable effort in studying the hydrogen storage properties in order to facilitate the release of H₂ at moderate technical

conditions. Despite all these experimental and theoretical investigations found in the literature, much research still needs to be done in order to answer the question: How can we improve the hydrogen storage properties? In this work, the focus is directed towards the structural, electronic, thermodynamic, and kinetic properties of NaMgH₃ as a hydrogen storage material.

2.3.1 Objectives

The emerging field of computational materials science has seen great success in materials design, particularly with the rapid updates of high-performance computing. As a synergic research process which now involves computing, as well as theory and experiment, this field can predict various properties of materials at much lower costs, therefore, shortening the research and development period. In this dissertation, NaMgH₃ is studied from a scientific perspective, as a hydrogen storage material, which has the potential to lead the transformation of energy consumption towards the hydrogen fuel. The following fundamental aspects of hydrogen storage properties are addressed:

1. The structural, electronic, vibrational, vibrational-based, and mechanical properties of the pristine NaMgH₃ crystal structure.
2. The effect on thermodynamics, electronic structure, and energetics of TM acting as doping agents at two different doping concentrations.
3. Effect of selected TM-doping the on (001) NaMgH₃ surface. Particular focus is directed towards the preferred TM and co-dopant combination to be inserted into the surface, dynamic evolution at high temperatures of the TM-doped (001) NaMgH₃ surface, effect of applied strain on hydrogen storage

properties, and hydrogen desorption from the pristine and modified (001) NaMgH₃ surface.

The following chapters in this dissertation cover the topic areas of thermodynamic, electronic, vibrational, kinetics, and structural properties of hydrogen storage materials. Also, literature review from similar hydrogen storage materials is presented in order to clarify key topics and provide details into a particular topic.

In Chapter 3, the methodology and simulation techniques employed are explained. Chapter 4 presents the results of the pristine NaMgH₃ crystal structure using DFT calculations focusing on the structural, electronic, vibrational, thermodynamic, and mechanical properties. In Chapter 5, simulation results obtained from decomposition reactions due to TM doping (at 25% mol concentration) are discussed. Also, DFT calculations to obtain the cohesive energy values of the TM-doped NaMgH₃ supercell (6.25% mol concentration) are reported for the entire 3*d* TM series. Details of bonding and electronic structure of NaMgH₃ supercell due to insertion of selected TM impurities are shown in this chapter as well.

The effect of point-defects on the lattice structure of the NaMgH₃ supercell is quantified in terms of hydrogen removal energy. The preferred Ti insertion site at the NaMgH₃ supercell is determined by means of substitution energy analysis. In Chapter 6, improvement of hydrogen storage properties (release and removal of hydrogen) from the (001) NaMgH₃ surface is investigated by means of TM-doping and applied mechanical strain. The preferred site for TM insertion and TM co-doping insertion is presented and determined by means of substitution energy. Also, the dynamic evolution of the Ti-doped and Zn-doped (001) NaMgH₃ surface models is investigated at PEM fuel cell operating

temperatures. In addition, a hydrogen desorption mechanism from the (001) NaMgH_3 surface is explained. Finally, Chapter 7 includes a conclusion of the work performed and future outlook of this research field.

CHAPTER 3

THEORY AND SIMULATION DETAILS

In recent decades, molecular modeling has been employed in materials science due to advances in computational power and integrated modeling software packages. Numerical experimentation provides an understanding of complex material at low cost; hence, computational simulations provide much more significant value as screening tools and guidance for experiments [88]. With the increasing demand for materials with improved performance for energy applications, industry, and research communities have become increasingly involved in studying novel materials at the molecular level. The structure of materials is linked to the types of bonding between the constituent atoms (metallic, covalent, and ionic bonding). To obtain a fundamental description of bonding requires a calculation of the electronic distribution. These types of methods that yield such information are called electronic structure methods [89]. Electronic structure methods are the most accurate way to calculate the structure, energy, and properties of a molecule or group of molecules [90].

This chapter outlines the theoretical basis for Density Functional Theory (DFT) [43, 44], which is at the core of computational materials science and one of the most successful electronic structure methods. This chapter also describes its use as implemented within the CASTEP and Dmol³ codes [91-94] from Accelrys, Inc.

3.1 Many-Body Equation

The Schrödinger equation is the equation for Quantum Mechanical calculations of the electronic structure of materials [89]. This equation was proposed by the Austrian physicist Erwin Schrödinger in 1926 and is presented in its time-independent form by:

$$H\Psi(r) = E\Psi(r) \quad \text{Eq. 3-1}$$

Here, H is the Hamiltonian operator corresponding to the total energy of the system (Quantum Mechanical operator that describes all interactions of particles); Ψ is the wave function (the function of all spatial coordinates of all electrons and ions in the system) [95]. E stands for the total energy of the many-particle system, which is the eigenvalue of H . Here, r represents the position vectors of each of the electrons and nuclei. It is important to note the following convention is used in this dissertation: atomic units are used in all equations, the equations are given for the spin-restricted case, the operator notation is omitted, and the coordinate notation includes the 3-dimensional position. This wave equation predicts analytically and precisely the probability of events. However, obtaining the information from the wave functions of this equation becomes nearly impossible due to its many-body nature (consequence of Pauli's exclusion principle and Heisenberg's exclusion principle). Therefore, simplifications such as DFT are necessary.

Due to the rapid growth on the number of DFT methods, a complete overview of DFT becomes impossible. This dissertation describes the essential elements of DFT.

3.2 Density Functional Theory

3.2.1 First Approximations

A first approximation to the many-body Schrödinger equation started with the Born-Oppenheimer (BO) approximation. In this approximation, the electrons' movement is decoupled from the nuclei (with the nuclei effectively having zero kinetic energies). Following the BO approximation, in 1964, Hohenberg and Kohn [13] proposed a new approach to model the many-body equation, which is to define the ground-state energy of a given molecular system in terms of its electron density. As mentioned previously, a fundamental description of bonding requires a calculation of the electron density (see Figure 3-1).

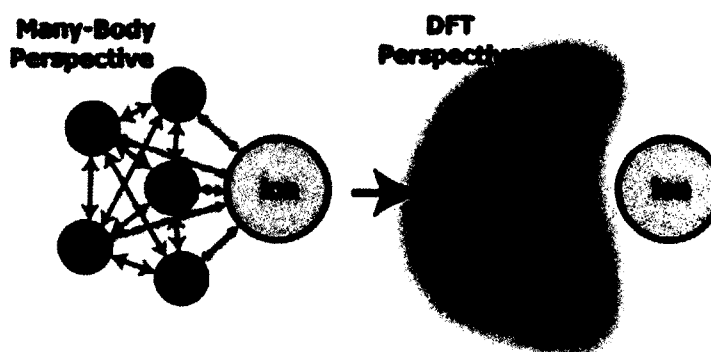


Figure 3-1: The external potential of many-particle system is determined by the electronic density, which is a function of the position, thus, the energy is a functional of the density [95, 96].

3.2.2 Hohenberg–Kohn Theorems

In the late 1920s, Thomas and Fermi came up with a procedure for calculating the energy of an electronic system, exclusively in terms of the electron density by minimizing the energy with respect to the density [96-99]. The proof that the ground-state

could be established through such a minimization was an assumption that was not proven until 1964 with the Hohenberg-Kohn (HK) theorem [100-102]. It is important to mention that the HK-based DFT is based on two theorems: i) the external potential (mainly electron-electron interaction energy) is solely determined by the electron density $\rho(r)$, besides a trivial additive constant and ii) it is possible to define the total energy functional of the density. Therefore, the ground-state density is found at the minimum of the total energy. The total energy is written as follows:

$$E(\rho) = F(\rho) + \int V_{\text{ext}}(r)\rho(r)dr \quad \text{Eq. 3-2}$$

Here, $F(\rho)$ is a universal functional of the electron density, which makes the minimum of Equation 3-2 equal to the ground-state energy of the electrons for an arbitrary external field $V_{\text{ext}}(r)$, given that the number of electrons is conserved. However, the HK theorem fails to describe how to obtain the functional. It is important to note that the knowledge of $F(\rho)$ imply the knowledge of the solution of the full many-particle equation. Moreover, the second theorem allows the treatment of the electron density as a variational parameter in the search for the ground-state energy [100]. Therefore, these two theorems form the mathematical basis of the HK-based DFT.

3.2.3 Kohn-Sham Method

A more general approach which helps to solve the many-particle problem was developed by Kohn and Sham (KS) in 1965 [44]. Kohn and Sham introduced a reference system consisting of non-interacting electrons that produce the same electron density of the interacting system.

Therefore, according to the KS method, the ground-state total energy of the many-particle system can be re-written according to Equation 3-3:

$$E\rho(\mathbf{r}) = E_{EP}\rho(\mathbf{r}) + E_H\rho(\mathbf{r}) + E_{XC+KE}\rho(\mathbf{r}) \quad \text{Eq. 3-3}$$

Here, the first term represents the external potential; the second term represents the Hartree energy (classical electron-electron Coulomb interaction). The third term describes the non-interacting kinetic energy of the electrons and the exchange-correlation energy of their interactions, respectively. It is important to note that the electron density of the many-particle system can be expressed according to Equation 3-4 (under the constraint that the molecular orbitals are orthonormal):

$$\rho(\mathbf{r}) = \sum_i^N |\phi_i(\mathbf{r})|^2 \quad \text{Eq. 3-4}$$

Here, according to the molecular orbital theory, $\phi(\mathbf{r})$ are one-electron functions or molecular orbitals. It is important to note that the Levi constrained search [103, 104] guarantees the chosen orbitals can construct the exact anti-symmetric wave function for the reference system of non-interacting electrons; that is, this search eliminates the possibility of unphysical densities. These orbitals are just a mathematical expression instead of the real wave function of electrons. Then, Equation 3-3 can be interpreted as the ground-state of a fictitious density of non-interacting electrons in an effective potential.

Therefore, after applying variational principles, a single-particle KS Hamiltonian is obtained:

$$\left(-\frac{1}{2}\nabla^2 + V_{eff}\right)\phi(r) = \varepsilon\phi(r) \quad \text{Eq. 3-5}$$

Here, ϕ are the eigenstates and ε the eigenvalues of the Kohn-Sham Hamiltonian.

The KS effective potential V_{eff} is further defined, and it includes the external potential, the Coulomb interaction, and the exchange-correlation contribution. The definition for the KS effective potential is shown in Equation 3-6. It is important to note that the application of Equation 3-6 leads to the solution of a system of equations for non-interacting particles moving in an effective external potential.

$$V_{eff}\rho(r) = V_{ext}(r) + V_{Hartree}(r) + V_{XC}(r) \quad \text{Eq. 3-6}$$

Here, $V_{ext}(r)$ is the total electron-ion potential. It is important to remark that the Hartree potential in Equation 3-6 includes a self-interaction contribution, so part of $V_{Hartree}(r)$ includes a Coulomb interaction between the electron and itself. However, this self-interaction is nonphysical, and the correction for this effect can be found in the exchange-correlation contribution [105]. Now that all the terms in the KS equation are known, it becomes an iterative problem, which can be solved in a self-consistent way on the condition that the exchange-correlation functional can be obtained. Specifying the exchange-correlation functional is the critical complication in the KS equations [105]. It is important to remark that the form of the exchange-correlation functional is simply not known. The exchange-correlation energy is less than approximately 10% of the total energy, but it is actively involved in the determination of material's properties, such as bonding, spin-polarization, and band gap formation [106]. Fortunately, this has been an

area of intense research during the last 30 years and several approximations are employed. The aim is to search for consistent approximations to the exchange and correlation terms where both terms are treated in a similar manner. This search is the main problem in modern DFT [107, 108].

3.2.4 Exchange and Correlation Functional in DFT

Perdew and co-workers [109] have characterized the description of the Quantum Mechanics of the electron within a Jacob's ladder of approximations (see Figure 3-2) with the goal of obtaining an accurate density.

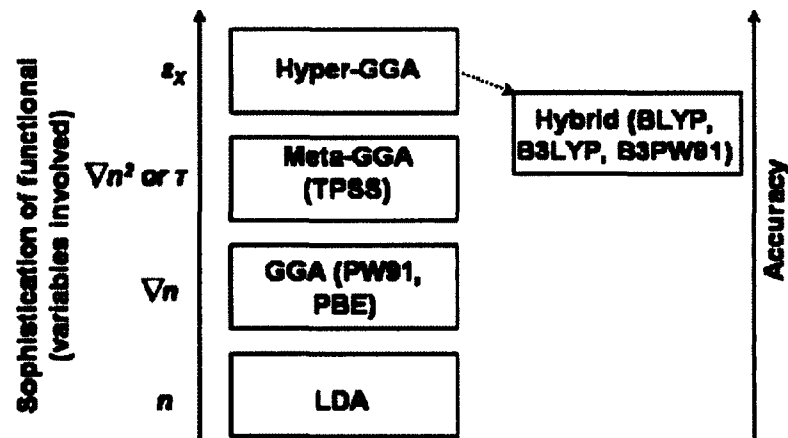


Figure 3-2: Perdew's "Jacob's Ladder" of density functional approximations. This is a strategy to construct improved density functionals for the exchange-correlation energy. Notice that LDA and GGA are placed at the first and second rung in Perdew's "Jacob's Ladder," respectively [110].

Typically, two kinds of approximations are used: they are, the Local Density Approximation (LDA) and the Generalized Gradient Approximation (GGA) [44]. As mentioned previously, the form of the exchange-correlation functional is not known. Therefore, this is where approximations must be made to obtain a suitable method [100].

Fortunately, the exchange-correlation functional can be derived accurately for the uniform electron gas.

Therefore, the exchange-correlation energy of a non-uniform electron density can be approximated as a sum of contributions from small volume elements each characterized by a uniform electron density [101]. Therefore, the LDA can be defined as the average of energy density:

$$E_{XC}^{LDA}[\rho(r)] = \int \rho(r) \epsilon_{xc}^{LDA}[\rho(r)] dr \quad \text{Eq. 3-7}$$

Here, $E_{XC}^{LDA}[\rho(r)]$ is the energy density that only depends on the local electron density; that is, the exchange-correlation energy in a local site is considered as the same as that of an electron gas with the same density as in a local site. Currently, the most commonly used fit for deriving the associated exchange-correlation effective potential is the one made by Vosko and co-workers [111, 112]. Therefore, this approximation provides a way to define Equation 3-7. This approximation has achieved great success for different types of systems (atoms, molecules, and clusters) because of the spherical average of the exchange-correlation hole [113]. A direct consequence of this is that, while LDA exchange-correlation energies are in accordance with the experiments, the exchange-correlation potential is not acceptable for chemical applications. Moreover, the LDA has some additional limitations such as:

1. Electronic densities of atoms in the core regions are localized; leading to a failure to cancel the self-interaction.
2. In metallic surfaces, the exchange-correlation potential decays exponentially into the vacuum region; leading to weak adsorption.

3. Overestimation of the cohesive energy, bond dissociation, and adsorption energy, as compared with the experimental work.

In order to address these limitations, a follow up approach consists of introducing an electron-density gradient in the dependence of the exchange-correlation on the charge density [43]. Therefore, this approach retains the correct features of the LDA and combines them with the energetically most important features (gradient corrected non-locality) [114]. This approach is the aforementioned GGA; non-local functionals depend on the gradient of density in space [115, 116]. The GGA can be defined as:

$$E_{xc}^{GGA}[\rho(r)] = \int \rho(r) \epsilon_{xc}^{GGA}[\rho(r), \nabla \rho(r)] dr \quad \text{Eq. 3-8}$$

The most commonly proposed functionals in literature, mainly between 1986 and 1996, are those by Becke (B88) [117], Perdew and Wang (PW91) [112], and Perdew, Burke, and Ernzerhof (PBE) [114]. Also, among another exchange-correlation functionals of the GGA form that take into account empirical information up to a certain extent are B86, G96, RPBE, and mPBE [96].

3.2.5 Finding the Ground-State Energy

As explained before, Hohenberg and Kohn established that there is one-to-one mapping between the ground-state density of the system and its potential. Kohn and Sham found an approximation to obtain the ground-state density. Then, from this ground-state density, many properties of the system can be determined. These features include equilibrium crystal structures, elastic constants, dielectric, and magnetic susceptibility.

However, how is this ground-state reached? The procedure for identifying the charge density can be summarized as follows:

1. Define an initial electron density.
2. Solve the KS equations to find the KS wave functions.
3. Calculate the electron density from the obtained KS wave function.
4. Compare the calculated electron density with the trial electron density. If the two densities are the same within a given tolerance, then the ground-state density has been found.

3.3 Periodic Systems

3.3.1 Bravais Lattice

When studying solids, the biggest challenge is that solid materials are made up of many atoms. As stated before, it is impossible to solve any equations of motion (classical or quantum) in a direct manner. Therefore, it is crucial for the description of electronic and vibrational properties of solids to take advantage of the crystal symmetry of the solid [118]. A fundamental definition to understand the periodicity of a solid is that of the Bravais lattice [119]. The Bravais lattice (R) is defined as an infinite periodic array of geometric points in space and is defined in Equation 3-9:

$$R = n_1a_1 + n_2a_2 + n_3a_3 \quad \text{Eq. 3-9}$$

Here, n and a are integers and vectors, respectively. Therefore, given the Bravais lattice, a primitive unit cell can be set. A primitive unit cell is any volume of space that, when translated through all the vectors of the Bravais lattice, fills all the space without any overlaps [118]. A standard primitive unit cell is the Wigner-Seitz cell [120]. The Wigner-Seitz cell is defined as the region of points closer to a given lattice point than to

any other lattice point. It is important to note that the primitive cell has the full symmetry of the lattice. Having defined the Bravais lattice, a crystal can be described by a Bravais lattice and a basis. The basis is considered to be a collection of atoms that are placed on every Bravais lattice site. Then, having the Bravais lattice and basis as a starting point, the reciprocal lattice is defined as the set of vectors G that result in the plane-waves with the periodicity of the Bravais lattice. Note, the importance of the reciprocal space is that it is a more appropriate environment in which to describe wave properties. The following relation holds if G is part of the reciprocal lattice of the Bravais lattice with points R :

$$e^{iG \cdot (r+R)} = e^{iG \cdot r} \quad \text{Eq. 3-10}$$

It is important to note that the G vectors also form a Bravais lattice:

$$G = n_1 b_1 + n_2 b_2 + n_3 b_3 \quad \text{Eq. 3-11}$$

Here, n and b are integers and vectors, respectively. Therefore, the use of the reciprocal lattice allows solid-state problems to use crystal symmetry and to be solved in a much simpler way (mainly due to the use of the plane-waves).

3.3.2 Plane-Wave Basis Set

The wave functions for electrons in a periodic crystal (considered as “free-electrons”) can be expanded in plane-waves [96]. The plane-wave method is based on the Bloch’s theorem [102].

According to the Bloch's theorem, the unit cell of crystals is extended using plane-waves with reciprocal lattice vectors G (due to space group symmetry):

$$\phi_G^k(r) = \frac{1}{\Omega} e^{i(k+G)r} \quad \text{Eq. 3-12}$$

Here, the exponential term is a plane-wave of wave vector k . In general, k is any complex vector. Therefore, with the Bloch's theorem, the problem of calculating a large number of plane-waves is avoided. Instead, a reduced number of plane-waves for an infinite number of k -points over the G vectors are used. This simplification (referred to as k -point sampling) is achieved by considering that the change in the wave function with k becomes negligible for k -points that are closely spaced from each other; hence, a finite number of plane-waves is calculated. Consequently, the electronic wave function at each k -point is expressed in terms of a finite number of plane-waves (referred to as plane-wave basis set). The plane-wave basis set is truncated in order to cover plane-waves with smaller kinetic energy than a particular cut-off energy.

3.3.3 Atomic Pseudopotential Approximation

The atomic pseudopotential approximation differentiates the outer electrons (valence electrons) from the core electrons and replaces the ionic potential of the nucleus and the core electrons with an effective atomic potential. Therefore, this atomic pseudopotential approximation reduces the number of plane-waves used (only valence electrons are considered in the calculations). On the other hand, for the core electrons, a pseudo-wave function is approximated.

It is important to note that there are other pseudopotential approximations such as the norm-conserving pseudopotentials, Troullier-Martin's pseudopotentials and Rappe *et al.* pseudopotentials (RRKJ) [96]. However, all calculations performed in this work are

done using ultrasoft pseudopotentials as proposed by Vanderbilt [121]. With ultrasoft pseudopotentials, it is possible to select a large cutoff radius (see Figure 3-3) well beyond the maximum of the radial wave function [96]. Therefore, for larger cutoff radii, the derivative of the wave function is smaller, avoiding sharp peaks in the pseudo-wave function and resulting in smoother wave functions.

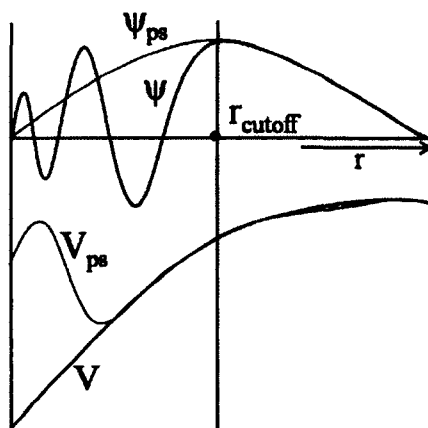


Figure 3-3: Schematic drawing of the atomic pseudo-potential approximation. The potential near the core electrons is replaced by a pseudopotential with smoother pseudo-wave functions with no nodes inside the cutoff radius [122].

3.3.4 Brillouin-Zone Sampling

Due to the application of the Bloch's theorem, the integrals in real space over the crystal are replaced by a discrete number of integrals over the Brillouin Zone (BZ) in the reciprocal space. In order to reduce the number of *k-points* used to sample the BZ, different approaches have been developed [123]. For instance, the Monkhorst-Pack scheme generates a grid of *k-points* spaced evenly throughout the BZ. When a supercell is used, a single *k-point* may be enough to describe any property in the BZ. This point is referred to as the *gamma-point*.

3.3.5 Electronic Properties

In solid-state physics, the density of states (DOS) of materials represents the number of states per interval of energy. Therefore, the DOS ($S_v(E')$) is defined such that $g(E) dE$ is the number of states in the energy interval E to $(E+dE)$ per unit volume of the sample [119]. The DOS is defined in Equation 3-13:

$$S_v(E') = \int_0^{E'} g(E) dE \quad \text{Eq. 3-13}$$

The DOS provides an electronic insight regarding the bonding within solids and assists in the classification of matter as metallic, semiconductor, or insulators [119]. A high DOS at a particular energy interval indicates that there are many states occupied or available for occupation. A DOS of zero means that no states can be occupied at that energy level (band gap). Recall that metals or semi-metals have delocalized electrons and no separation between valence and conduction band. On the other hand, solids with a band gap larger than 3 eV are called insulators, whereas materials with a smaller gap are categorized as semiconductors. It is important to note that the band gap calculated with DFT is usually underestimated (mainly because the approximations do not compensate satisfactorily for the self-interaction present in the Hartree term) [105]; however, the general trends of DOS are well reproduced when compared with experimental measurements [124].

Another important method to study the electronic properties of materials is the charge density. The charge density represents the charge distribution in real space; it is a physically measurable quantity [100]. When applied as a reference for the discussion of bonding, the charge density allows for a direct analysis and physical picture. For instance,

in covalent bonding, the charge density is distributed over the bonds and the electron density is represented by a smeared cloud that is shared equally between the bonds. Similarly, in ionic bonding, the charge density is localized in the region of the nucleus. It is important to note that within this bonding scheme, the localized density exerts the attractive force which binds both nuclei. For a quantitative description of charge distribution, the Hirshfeld charge analysis and Mulliken scheme are used [125, 126]. The Hirshfeld scheme creates a charge density for an ideal reference system from the ground-state atomic densities of the isolated atoms and weighs each point in space according to its contribution to this density [100, 125]. On the other hand, population analysis in CASTEP is performed using a projection of the plane-wave states onto a localized basis using a technique described by Sanchez-Portal *et al.* [127]. Then, the population analysis of the resulting projected states is performed using the Mulliken scheme. Furthermore, charge density difference provides a view of the molecular charge redistribution. The charge difference is calculated by the integration of the molecular densities minus free atoms' density.

3.3.6 Lattice Vibrations

According to the kinetic molecular theory, the atoms in a solid material are oscillating about their lattice position by stretching and compressing their bonds [128]. These oscillations are considered to be simple harmonic (quantum harmonic oscillator) in order to be considered in thermal equilibrium. It is important to note that a simple harmonic motion is a periodic motion where the force is directly proportional to the displacement in one direction (resembling Hooke's law). This linear relationship shows that the oscillation frequency of the mass is independent of the amplitude of the

displacement. Hence, it provides a starting point for the description of complicated motions by decomposing and rebuilding trigonometric functions. The following equation shows the harmonic approximation to the potential energy $V(x)$:

$$V(x) = \frac{1}{2} \beta \times x^2 \quad \text{Eq. 3-14}$$

Here, β is a spring constant. In order to obtain a description of these lattice vibrations, approximations are made. First, it is assumed that the mean equilibrium position of each ion form a Bravais lattice. Secondly, it is assumed that the amplitude of atomic displacements is small compared to interatomic distances. In modern physics, the energy of the harmonic oscillator must be calculated using Equation 3-14 in the Schrödinger Equation (Equation 3-1 in this dissertation). The solution of the Schrödinger Equation shows that the energy of the harmonic oscillator is quantized:

$$E_n = (n + \frac{1}{2}) \hbar \omega \quad \text{Eq. 3-15}$$

Here, ω is the angular frequency of the vibrations and n is a quantum number. From Equation 3-15, it is apparent that the minimum energy of the oscillator can never be zero; this energy is called the Zero-Point Energy (ZPE). It is well-known that atomic vibrations are coupled. The coupled vibrations lead to waves that involve a combined vibration of several atoms and cannot be described by the movement of individual atoms. Therefore, as an atom oscillates, it transfers its energy to nearby oscillating atoms, and these coupled-vibrations produce traveling waves in the crystal. It is important to note that for materials with a more complicated crystal structure more complicated processes can occur simultaneously. In this dissertation we present an equation describing the

displacement in a two-dimensional case. The displacement U_r of an atom in equilibrium at x_r can be represented by a traveling-wave:

$$U_r = A e^{j(k x_r - \omega t)} \quad \text{Eq. 3-16}$$

Here, A is the amplitude, k is the wave vector, and ω is the angular frequency.

This lattice wave equation corresponds to a harmonic oscillator with a frequency ω .

Therefore, the energy of this lattice vibration is quantized in the same way the energy of the harmonic oscillator is quantized. This quantum of a lattice vibration is called a phonon ($\hbar\omega$). From these equations, it can be seen that the frequency of vibrations and the wave vector K are coupled. The equation that couples them is called the dispersion relation:

$$\omega = 2\left(\frac{\beta}{M}\right)^{\frac{1}{2}} \left| \sin \frac{1}{2} Ka \right| \quad \text{Eq. 3-17}$$

The importance of the phonon interpretation of lattice vibrations is due to the large number of physical properties that can be understood in terms of phonons. In this dissertation, the focus is on the phonon DOS. Phonon DOS ($S_v(\omega')$) is computed in a similar fashion as the electronic DOS:

$$S_v(\omega') = \int_0^{\omega'} g(\omega) d\omega \quad \text{Eq. 3-18}$$

Here, $g(\omega)$ is the number of modes per unit frequency; then, $g(\omega) d\omega$ is the density of vibrational states or modes. Therefore, $g(\omega) d\omega$ is the number of states in the range of $d\omega$. Results from phonon DOS are used to calculate thermodynamic functions such as enthalpy (H), Free energy (G), entropy (S), and heat capacity (C_m) as functions of temperature [129, 130].

Temperature dependent enthalpy is given by adding the total energy and the sum of ZPE corrections:

$$H(T) = E_{elec} + E_{ZP} + \int \frac{\hbar\omega}{\exp(\frac{\hbar\omega}{kT}) - 1} G(\omega) d\omega \quad \text{Eq. 3-19}$$

The Free energy can be defined as the amount of work a system can perform. In order to determine if a reaction will be favorable and release energy, the Free energy is calculated. It is important to note that the experimental application of this function is limited to conditions where temperature, volume, and pressure are held constant. The Free energy as a function of temperature is given by:

$$G(T) = E_{elec} + E_{ZP} + kT \int G(\omega) \ln \left[1 - \exp\left(-\frac{\hbar\omega}{kT}\right) \right] d\omega \quad \text{Eq. 3-20}$$

Entropy is given by:

$$S(T) = k \left[H(T) - \frac{G(T)}{T} \right] \quad \text{Eq. 3-21}$$

The Free energy as a function of temperature can also be calculated in the following way:

$$G(T) = H(T) - TS \quad \text{Eq. 3-22}$$

3.3.7 Mechanical Properties

Stress and strain tensors accurately describe the response of a solid material to an external load. This is important for the hydrogen storage research since the materials need to be evaluated under various internal and external load conditions.

In a simplistic approach, if a normal stress is applied in the x direction, the deformation (stress) of the material can be described by the following equation:

$$\varepsilon_{xx} = \frac{1}{Y} \sigma_{xx} \quad \text{Eq. 3-23}$$

Here, Y is the Young's Modulus and σ_{xx} is the applied strain in the x direction.

The above equation is the Hooke's law for the elastic strain. In order to describe the state of deformation due to an arbitrary stress applied to the solid, elastic constants are used. These elastic constants are generally represented by a tensor of rank 4 (C_{ijkl}), where each index takes three values corresponding to x, y, and z. In this work, a contracted version is used (C_{ij}), which takes six indexes according to the Voigt notation [102]. The following identification of indexes is made in order to make a connection between the two sets of elastic constants:

$$1 = xx, 2 = yy, 3 = zz, 4 = yz, 5 = zx, 6 = xy \quad \text{Eq. 3-24}$$

The contracted elastic constants relate stress to strain in the following manner:

$$\begin{aligned} \sigma_{xx} &= C_{11}\varepsilon_{xx} + C_{12}\varepsilon_{yy} + C_{13}\varepsilon_{zz} + C_{14}\varepsilon_{xy} + C_{15}\varepsilon_{yz} + C_{16}\varepsilon_{zx} \\ \sigma_{yy} &= C_{21}\varepsilon_{xx} + C_{22}\varepsilon_{yy} + C_{33}\varepsilon_{zz} + C_{24}\varepsilon_{xy} + C_{25}\varepsilon_{yz} + C_{26}\varepsilon_{zx} \\ \sigma_{zz} &= C_{31}\varepsilon_{xx} + C_{32}\varepsilon_{yy} + C_{33}\varepsilon_{zz} + C_{34}\varepsilon_{xy} + C_{35}\varepsilon_{yz} + C_{36}\varepsilon_{zx} \\ \sigma_{yz} &= C_{41}\varepsilon_{xx} + C_{42}\varepsilon_{yy} + C_{43}\varepsilon_{zz} + C_{44}\varepsilon_{xy} + C_{45}\varepsilon_{yz} + C_{46}\varepsilon_{zx} \\ \sigma_{zx} &= C_{51}\varepsilon_{xx} + C_{52}\varepsilon_{yy} + C_{53}\varepsilon_{zz} + C_{54}\varepsilon_{xy} + C_{55}\varepsilon_{yz} + C_{56}\varepsilon_{zx} \\ \sigma_{xy} &= C_{61}\varepsilon_{xx} + C_{62}\varepsilon_{yy} + C_{63}\varepsilon_{zz} + C_{64}\varepsilon_{xy} + C_{65}\varepsilon_{yz} + C_{66}\varepsilon_{zx} \end{aligned} \quad \text{Eq. 3-25}$$

These equations are valid if the solid deformation is sufficiently small, consequently, implying that the deformation is linear in the applied stress.

3.4 Types of Simulation

In this work calculations have been performed using the Cambridge Sequential Total Energy Package (CASTEP) [91, 92, 131] program within the Materials Studio version 6.0 software from Accelrys, Inc. CASTEP is a first-principles quantum mechanical program to perform calculations based on KS-DFT. The electronic wave functions are treated as plane-waves, and the core electrons are represented by ultrasoft pseudopotentials as described by Vanderbilt [121]. For this dissertation, the exchange-correlation contribution to the total energy is implemented through the use of the GGA-PBE approximation to the exchange and correlation functional. Among some of the GGA functionals available in the CASTEP code (Wu-Cohen [132] and PW91 [112]), the PBE functional remains superior for the energetics of covalent and non-covalent bonds [133]. Moreover, the mean absolute deviation of binding energies between plane-wave PBE and a Gaussian basis set rarely exceeds 1 kcal/mol [134]. It is important to mention that the use of pseudopotentials may change the equilibrium bond length by up to 0.05 Å.

A self-consistent field method is applied to manipulate the electronic density in order to reach the ground-state energy. The convergence criteria for the plane-wave is set to 2.0×10^{-6} eV/atom. The kinetic energy cutoff of 370 eV (for geometry optimization calculations) is determined through initial single-point energy calculations. Similarly, for phonon calculations, the geometry of the models is optimized with a kinetic energy cutoff of 625 eV. The Brillouin Zone is integrated using the Monkhorst-Pack grid of 0.04 1/Å . Geometries are optimized without any symmetry constraints using the quasi-Newton minimization method of Broyden, Fletcher, Goldfarb and Shannon (BFGS) [135]. For this minimization procedure, density mixing is used. Density mixing produces a new estimated electron density utilizing a linear combination of the input charge densities

from a previous history of electron densities. Fast Fourier Transforms (FFT) is used within CASTEP to transform various entities (wave functions and potentials) from real to reciprocal space and back.

In general, these are algebraic manipulations to solve the matrix problem efficiently. Typically, the Hamiltonian matrix is projected, approximated, preconditioned, or spanned in subspace. With geometry optimizations, errors arise due to the change of the reciprocal space. It is important to note that plane-waves are treated in reciprocal space. The solution for this is to fix the cut-off energy allowing the set of plane-waves to vary along the length of the reciprocal space. The partial occupancies of the wave functions are described by a Gaussian smearing method set to 0.1 eV. This smearing method heats up the material by including fictitious thermal energies. This method does not reproduce fine features of the DOS, but it adequately reproduces the general trend of the DOS [106]. In order to obtain accurate forces during the optimization step, a convergence tolerance of 0.03 eV/Å on residual forces on each atom is established. For the phonon calculations, a convergence tolerance of 0.02 eV/Å on residual forces on each atom is established. In order to understand electronic effects within the material, DOS plots and charge analysis schemes are applied [125, 136, 137].

For Chapter 4, the computational approach employed is commonly used by the computational materials science community to determine the structure and energetics of NaAlH₄ and Ti-doped NaAlH₄ [138-148]. Typical CASTEP calculations reported here show bond length values accurate to three significant figures [92]. Finite-difference method or Supercell method as implemented in CASTEP by Montanari *et al.* [149] is used to calculate phonon frequencies. This method involves slightly perturbing the

positions of the atoms and calculating the reaction forces due to this perturbation. From this perturbation a force constant matrix is calculated, which is obtained by differentiating the Hellmann-Feynman forces on the atoms, with respect to the ionic coordinates. To perform this calculation, it is necessary to expand the original unit cell and convert them into supercells. However, Klaveness *et al.* [150] reported that a $2 \times 1 \times 2$ cell is sufficient to calculate the phonon contributions in crystal NaMgH_3 , that is, the forces beyond the $2 \times 1 \times 2$ cell are assumed to be zero. The main advantage of this is that there is no need to switch to a norm-conserving pseudopotential. Instead, ultrasoft pseudopotentials are used with a higher kinetic energy (625 eV). From this force, constant matrix is possible to obtain the phonon DOS. Similarly, the elastic constants are calculated by setting the strain amplitude to a finite value (0.003) and performing four steps for each strain.

For Chapter 6, as a preparation step for the slab construction, the original crystal structure of NaMgH_3 as reported by Klaveness *et al.* [31] is optimized and serves as the input for the surface model calculations. In order to model the pristine and the modified surfaces, surfaces with four-layer slabs (see Figure 3-4) are used consisting of sixteen formula units. The vacuum space normal to the surface is 15 Å to guarantee a sufficient separation between the periodic images. The top two layers in each slab are relaxed to a 0.03 eV/Å residual force convergence, whereas the bottom two layers are fixed at their bulk configurations.

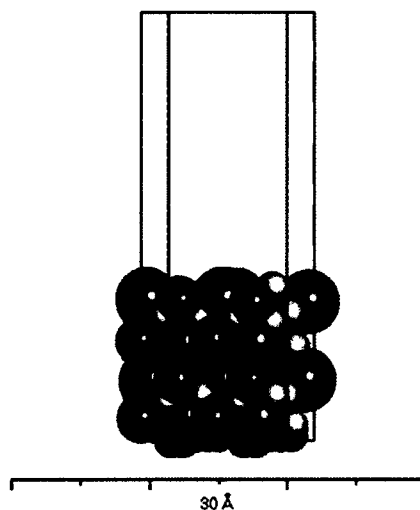


Figure 3-4: Side view of the optimized four-layer (001) NaMgH_3 surface slab consisting of 80 atoms. A vacuum slab (15 Å) normal to the surface is added to avoid interactions with periodic image in this direction. Here, purple, green, and grey spheres denote Na, Mg, and H atoms, respectively.

Then, neutral TM (Ti, V, Cu, and Zn) are introduced at the Na lattice site. These dopants are located at the outermost and subsurface layers. Neutral TM are selected over other oxidation states because experimental work on NaAlH_4 by Felderhoff *et al.* [151] showed that after Ti-doping, a zero-valent Ti species is formed which remains virtually unchanged during the course of the cycle test. Full relaxation of atoms (all atoms are allowed to relax) is performed for the Ti-doped model to determine the influence of strain effect due to freezing of the two-bottom layers. The energy difference between these two models is almost negligible in the Ti-doped structure (0.003 eV/atom), implying that the strain effect is negligible on the atomic configurations in the relaxed TM-doped (001) NaMgH_3 surface layers. In addition, *ab-initio* molecular dynamics simulations are carried out with two dopant types: Ti-doped and Zn-doped (001) NaMgH_3 surface slab models. These simulations are carried out in order to investigate the structure of these models at the finite temperatures of 300 K and 400 K (room temperature and the typical

temperature of PEM fuel cell). In order to avoid the computational cost of a four-layer slab, DFT-MD simulations are carried out on a reduced two-layer surface slab model with a 10 Å vacuum slab (see Figure 3-5). A similar computational approach is applied by Dathar *et al.* [21] in the study of Ti-doped (001) NaAlH₄ surface slab models.

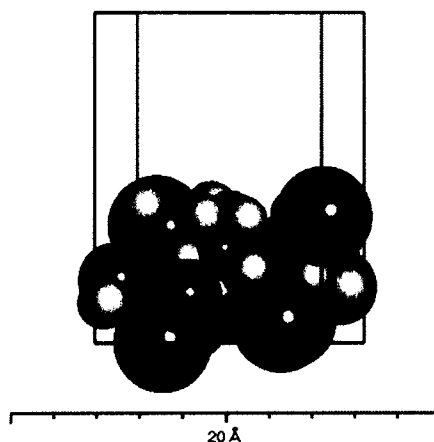


Figure 3-5: Relaxed two-layer surface slab consisting of 40 atoms. Here, the red sphere represents the TM dopant.

The initial structure is taken from the geometry optimization of the corresponding four-layer slab model. Therefore, only the top two outermost layers are considered for the *ab-initio* molecular dynamics simulations. For the co-dopant models, four different combinations of Ti and Zn-doped (001) NaMgH₃ surface slab models are used. Here, the naming convention “TM_{n₁/n₂}TM_{n₁/n₂}” is used to indicate that the TM replaces Na at the outermost surface site (n₁) or the subsurface site (n₂). The configurations considered in this study are the following: Ti₁Zn₂, Ti₂Zn₂, Zn₁Ti₁, and Zn₁Ti₂.

For the strain-effect models, this dissertation follows a similar approach to the one implemented by Zhang *et al.* [152] and Hussain *et al.* [153] using GGA-PBE periodic calculations. Here, the application of a homogeneous biaxial strain $\Delta \leq 5\%$ is considered

by varying the lattice parameter “ a ” and setting it equal to the “ b ” lattice parameter ($a=b$) to give Equation 3-26:

$$\Delta = [(a-a_0)/a_0] \times 100\% \quad \text{Eq. 3-26}$$

Here, “ a_0 ” is the ground-state lattice parameter, and “ a ” is the lattice parameter due to the applied strain. It is important to remark that the biaxial strain is applied to the crystal by modifying the lattice parameter with respect to its DFT-geometry optimized equilibrium value.

3.4.1 Transition-State Search

A common strategy to search for a transition-state (TS) is to set up a simulation that attempts to obtain a TS between two configurations (typically referred to as reactant and product configurations). To obtain this structure, a set of images that connect the reactant and product structures are needed. Materials Studio 6.0 performs this by using the “Reaction Preview” tool that interpolates the atomic coordinates between the reactant and product configurations. Then, with this functionality of Materials Studio 6.0, the atoms are mapped between the reactant and product models. The atoms are mapped according to the Principle of Least Motion (PLM) [154]. According to this principle, the least distance moved by each atom is the most probable to occur within the model.

In this dissertation, Equation 3-27 describes how the intermediate structure based on atom pairing is achieved:

$$r_{ab}^i(i) = (1-f)r_{ab}^R + fr_{ab}^P \quad \text{Eq. 3-27}$$

Here, $r_{ab}^i(i)$ is the interpolated intermediate, r_{ab}^R and r_{ab}^P are the inter-nuclear distances between the pair of atoms a and b in the reactant and the product, respectively. Also, f is a proportion parameter that varies between 0 and 1 [155]. It is important to note

that the initial configuration of these images influence the overall direction and speed of the search. Furthermore, in the case of the chemical process related to kinetic calculations, the TS energy is called the activation energy. The TS energy is obtained through linear interpolation between the energies of the geometry-optimized reactants and products models. The PES of a reaction is obtained through a linear synchronous transit (LST) method in conjunction with a quadratic synchronous transit (QST) calculation and conjugate gradient (CG) search as implemented in CASTEP. Here, with these methods, the PES of a reaction is obtained by bracketing the maximum between the reactant and the product and performing energy minimization of the obtained maximum in the reaction pathway. Notice, for the LST algorithm, the extrapolation equation to find an initial equation is linear. Similarly, for QST algorithm, the extrapolation equation is quadratic.

The combined LST/QST algorithm starts with the LST approach. First, the LST maximum on the PES is found (see Figure 3-6, where the LST maximum is shown by the green dot). Then, a QST search in conjunction with a CG minimization (see Figure 3-6, where the red dot shows the QST/CG minimization) is performed until the search convergence is obtained. It is important to remark that the TS represents the maximum point along the lowest energy pathway between the reactants and products. Also, this TS energy is determined by geometry optimizing the TS activated complex found at this maximum point.

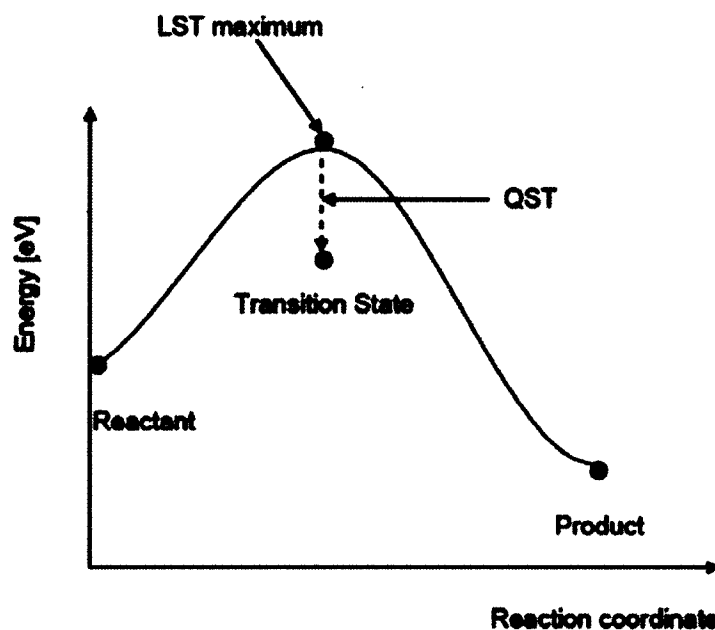


Figure 3-6: Schematic drawing of a TS search using the LST/QST algorithm [156].

Therefore, based on this definition, the activation energy in this work is calculated according to the following equation:

$$E_{act} = E_{TS} - E_{reactant} \quad \text{Eq. 3-28}$$

Here, E_{TS} is the energy of the TS structure (H_2 desorbed 5 Å normal to the (001) NaMgH_3 surface) and $E_{reactant}$ is the energy of the reactant model (pristine and TM-doped (001) NaMgH_3 surface models). In order to thoroughly investigate the reaction paths, the Nudged Elastic Band (NEB) method is used as implemented in the “transition-state confirmation tool” of the DMol³ module [93] from Accelrys, Inc. The NEB method belongs to the chain-of-states methods [96], in which several images of the system are connected by tracing the path for the transition process. The NEB method is not only used to search for reaction paths but also to establish a minimum energy path (MEP) for a given transition process when both the initial and the final states are guessed beforehand.

When applying the NEB method, the search begins with a number of models of the system that are connected by artificial springs. These images represent a particular configuration of the system along the path between the initial and the final states. The method works by means of linear interpolation of images between the known initial and the final states, and by minimizing the energy of these images. During the minimization process, the distance between the neighboring images is kept equal. Once the energy of each image is minimized, the MEP is found. Hence, the method can provide both the TS configuration and insights into the characteristics of the PES landscape.

3.4.2 DFT coupled Molecular Dynamics (DFT-MD)

DFT coupled Molecular Dynamics (DFT-MD) simulations are employed in order to study the evolution of the systems at high temperatures. The forces acting on the atoms are obtained through electronic structure calculations. In DFT-MD, the biggest challenge is the computational cost. The long computational time required to calculate the forces that are acting on the ions limits the simulations to a few tens of atoms. In Born-Oppenheimer molecular dynamics, the calculation of the forces acting on the atoms and the trajectory of the nuclei are treated separately. Therefore, for this method, the time step is determined by the dynamics of nuclei instead of those of electrons. That is, at each step, the forces have to be calculated while the atoms are fixed at this time, therefore creating an expensive computational calculation. A few approximations can be made to minimize this expense.

For instance, wave function extrapolation [157] and charge density extrapolation [158] methods between steps are applied to provide a reasonable starting configuration, therefore minimizing the time spent on the electronic minimization. To account for the

temperature effect, micro-canonical (NVE-constant number of particles, constant volume, and constant energy) and canonical ensembles (NVT-constant number of particles, constant volume, and constant temperature) are used for DFT-MD simulations. The NVE ensemble is used to investigate the dynamics of the systems in a constant-energy conformational space. Meanwhile, the NVT ensemble is used to study the dynamics of systems under the influence of fixed temperature by keeping the volume of the system fixed. It is important to remark that at the start of the DFT-MD simulations, there will be oscillations of terms such as total energy and temperature. Also, it is important to determine when the simulation is equilibrated. The equilibration is achieved by looking at the convergence of properties such as: total energy, forces, velocities, and atomic positions.

Typically, there are three different levels for DFT-MD methods. First, the Ehrenfest Molecular Dynamics (EMD), in which the equations of motion and the electronic Schrödinger equation are solved simultaneously. Due to the computational demands, this method is unfeasible for many practical applications. Next, the Car-Parrinello Molecular Dynamics (CPMD) avoids the solution of the Schrödinger equation in each step. Instead, fictitious particles are allowed to evolve with the equations of motion for a specific number of steps. In this dissertation, the third method, the Born-Oppenheimer Molecular Dynamics (BOMD) method is employed. As the name suggests, this method uses the BO approximation and employs two different and decoupled timescales (corresponding to the nuclei and the electrons). Consequently, this can be considered a static problem, where the Schrödinger equation is solved with the fixed nuclei. Then, the equations of motion for the nuclei moving in a PES (generated by the

electrons) is solved. It is important to note that this adiabatic approximation allows for the solution of larger time-steps than the EMD method [159].

In addition, in the BOMD method, the nuclei are treated as classical particles. Therefore, each step of the BOMD method involves solving the Schrödinger equation by using the KS-based DFT approximation. Solving of this equation is followed by calculating the forces exerted on the nuclei (due to electrons and other nuclei). Finally, the integration of the nuclear dynamics due to the forces exerted is performed. It is important to note that the force exerted on the nuclei by the electrons is calculated from the electron density (as obtained from the KS-based DFT calculations). Therefore, this is a computationally expensive approach due to the optimization of the electronic wave function at each step.

Moreover, in order to generate an NVT ensemble, a modification must be introduced in order to account for the effect of the thermal bath. In this dissertation, the Nosé-Hoover chain thermostat is employed [160]. The Nosé-Hoover chain thermostat technique assures ergodic sampling of phase space even for the harmonic oscillator. In this thermostat, degrees of freedom are added to the system to mimic a reservoir representing the properties of the desired NVT ensemble. The ergodicity is assured by coupling the original thermostat with several thermostats.

CHAPTER 4

DFT STUDY OF SODIUM MAGNESIUM HYDRIDE

A computational study has been performed on the pristine crystalline structure of NaMgH₃. First, the geometry of the crystalline structure of this material is determined via first-principles calculations; then, the optimized-crystalline model is used to study the mechanical, electronic, and vibrational-based properties. Since the fundamental properties of this material have not been widely studied and clarified from an experimental standpoint, this study provides the necessary knowledge for energy and hydrogen storage applications.

4.1 Results

4.1.1 Geometry of Pristine NaMgH₃ Crystal

A model representing the NaMgH₃ unit cell (Figure 2-1) that contains four formula units (20 atoms) is built, and its geometry optimized using DFT. The calculated lattice parameters a, b, and c are obtained by allowing all atomic positions to relax to a minimum energy. The optimized lattice parameters obtained at the GGA-PBE theory level shows a remarkably close agreement with experimental findings, leading to a small deviation between the experimental and the DFT-predicted unit cell volume (see Figure 4-3) [25, 160-162].

Similarly, the crystal structures of KMgH₃, MgH₂, and NaH hydrides are built according to their experimental crystallographic information presented in the work of

Klaveness and co-workers (see Figure 2-2, Figure 4-1, and Figure 4-2) [31]. Then, the geometry of the crystal structures are optimized at the GGA-PBE theory level. It is important to note that the crystal structures of KMgH_3 , MgH_2 , and NaH belong to the $Pm3m$, $P42/mnm$, and $Fm3m$ space groups, respectively.

From these results, one can see that the calculated lattice parameters are in close agreement with the experimental values reported by Klaveness *et al.* [31]. Consequently, due to the accuracy of these simulations, it is possible to investigate the interaction among the atoms in the crystal.

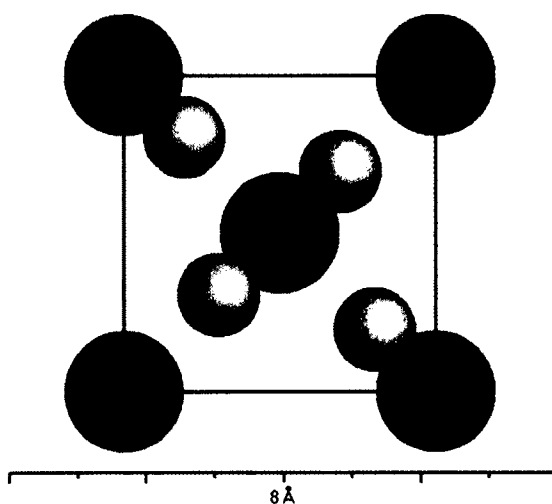


Figure 4-1: Front view of the crystal structure of pure MgH_2 .

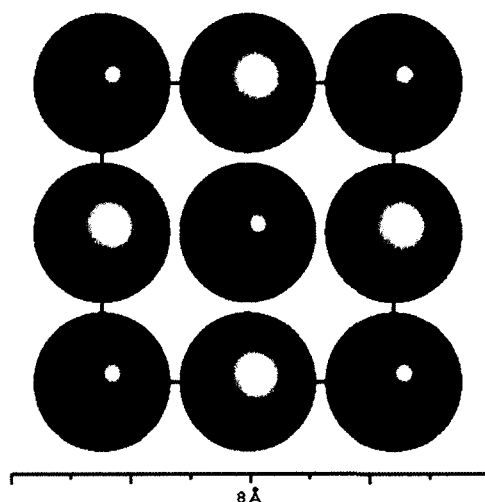


Figure 4-2: Front view of the optimized structure of the NaH crystal structure.

It is necessary to note that the majority of the experimental work conducted so far on NaMgH₃ has focused on the hydrogen interaction, therefore neglecting the Na-Mg interaction. Also, it is important to measure the bond distances between the constituent atoms of NaMgH₃ to validate the DFT predictions. Rönnebro *et al.* [161] compared the bonding distances in the hydride and fluoride phases of NaMgX₃. Here, X represents deuterium (D) or fluorine (F) atoms. Rönnebro and co-workers [161] showed that the Na-D distances are more distorted than the Mg-D distances; that is, the Na-D distances vary over a range of 2.26-2.47 Å for Na-D bonds and 2.30-2.69 Å for Na-F bonds. Similarly, bond distances are 1.96-1.98 Å for Mg-D bonds and 1.98 Å for Mg-F bonds. The calculated average for the nearest neighbors bond distances of Na-Mg, Mg-H, and Na-H bonds are 3.33 Å, 1.98 Å, and 2.28 Å, respectively (see Table 4-1). The average Na-Mg-Na angle is calculated to be approximately 68°. The tilting angle of the MgH₆ octahedral group in the optimized unit cell is 13.68°.

Table 4-1: Calculated average bond distances and lattice parameters for pure NaMgH₃, MgH₂, NaH, and KMgH₃ at the GGA-PBE theory level. Experimental information for NaMgH₃ based on Deuterium is given in parenthesis. Distance for K-Mg shown with a (*) was reported by Reshak *et al.* [21]. Experimental distances for Mg-H and Na-H bonds are taken from ref. [4]. The experimental lattice parameters are taken from Klaveness *et al.* [20].

Bond Length (Å)	NaMgH ₃	MgH ₂	NaH	KMgH ₃
Na/K-Mg	3.33			3.48 (*3.49)
Mg-H	1.98 (1.96-1.98 Å)	1.97		2.01
Na/K-H	2.28 (2.26-2.47 Å)		2.43	2.84
Lattice Parameters (Å)				
<i>A</i>	5.463 (5.479)	4.877 (4.517)	4.544 (4.890)	4.020 (4.029)
<i>B</i>	7.703 (7.675)			
<i>C</i>	5.411 (5.399)	3.029 (3.020)		

The calculated Na-H average bond length (2.28 Å) is well in agreement with the Na-D bond length found in ref. [161], and the Mg-H average bond length value in this work (1.98 Å) corresponds remarkably well to the experimental value found in ref. [162].

4.1.2 Geometry of Modified-NaMgH₃ Crystal

Although a large number of first-principles calculations of the properties of promising hydrogen storage materials has been reported during the last years, atomic calculations using innovative techniques for NaMgH₃ hydrogen storage research are insufficient. Hence, a DFT study of the NaMgH₃ crystal under hydrostatic pressure is conducted in this work. The NaMgH₃ lattice parameters as functions of external pressure are calculated by optimizing the pristine crystal structure subjected to hydrostatic pressures in the range of 10 to 40 GPa. The relative Mg-H and Na-H average bond

distances and the corresponding change of volume (V/V_0) in the NaMgH_3 crystal with pressure are shown in Figure 4-3. For hydrogen storage applications, the focus is on the Mg-H bond. At the 10 GPa pressure, the Mg-H average bond distance is shortened to 1.87 Å, whereas at the 40 GPa pressure the Mg-H average bond distance is even shorter at an average distance of 1.72 Å.

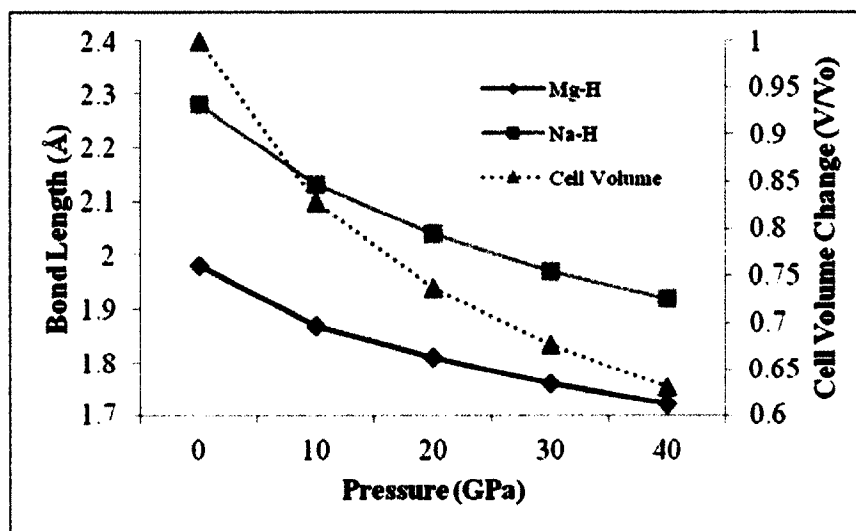


Figure 4-3: Average bond lengths in NaMgH_3 as a function of hydrostatic pressure. Here, unit cell volume change vs. hydrostatic pressure is also shown. Results are calculated at the GGA-PBE theory level.

These results demonstrate that the applied hydrostatic pressure creates a contraction of all relevant bond distances and causes considerable volume change in the NaMgH_3 crystal. A procedure like this one could be used to increase the hydrogen density/mobility in the material [163]. The calculated average atomic charges with the Hirshfeld scheme supports that there is transfer of electrons to H for the pressure range 10-40 GPa (see Table 4-2). It is important to note that positive values correspond to the

amount of accumulated electrons and the negative values correspond to accumulated holes.

Table 4-2: Average Hirshfeld charges of individual atoms as a function of hydrostatic pressure as obtained from DFT calculations on a NaMgH₃ crystal structure. The 0 GPa row represents the values calculated for the ground-state structure. DFT calculations are performed at the GGA-PBE theory level.

Hirshfeld Analysis (<i>e</i>)			
Pressure (GPa)	Na	Mg	H
0	0.24	0.27	-0.17
10	0.24	0.25	-0.16
20	0.25	0.22	-0.16
30	0.25	0.22	-0.16
40	0.25	0.22	-0.16

The decreasing positive value of the Hirshfeld charge of Mg in the pristine NaMgH₃ crystal is due to the increased association with H atoms (as indicated by the Mg-H bond contraction). Thus, the redistribution of the electron charge is attributed to the chemical bonding between the Mg and H atoms at this pressure range. Meanwhile, the Na atoms are more cationic and in line with their larger size when compared to the Mg atoms.

Even though it can be deduced that applying hydrostatic pressure to the material would compress its size, the exact magnitude of this compression has not been calculated for this material. In addition, from the results it can be speculated that the hydrostatic pressure can change the interaction between constituent atoms that can, consequently, lead to distinctive changes in the structural and electronic properties of the NaMgH₃

crystal. Indeed, Lozano *et al.* [164] in their study of NaAlH₄ reported that even at high compaction levels and low initial porosities, hydrogen absorption and desorption kinetics can proceed comparatively fast in compacted material. These results indicate that the hydrostatic pressure effect can play a pivotal role in the hydrogen desorption process from this material by varying the chemical bonding nature of the Mg-H bond.

4.1.3 Electronic Structure of Pristine NaMgH₃

The properties related to electronic structure, including the DOS and the PDOS of the pristine NaMgH₃ unit cell are also calculated at the GGA-PBE theory level. The plots for the DOS and PDOS shown in Figure 4-4 show that the crystal structure of NaMgH₃ has a band gap value of approximately 3.50 eV.

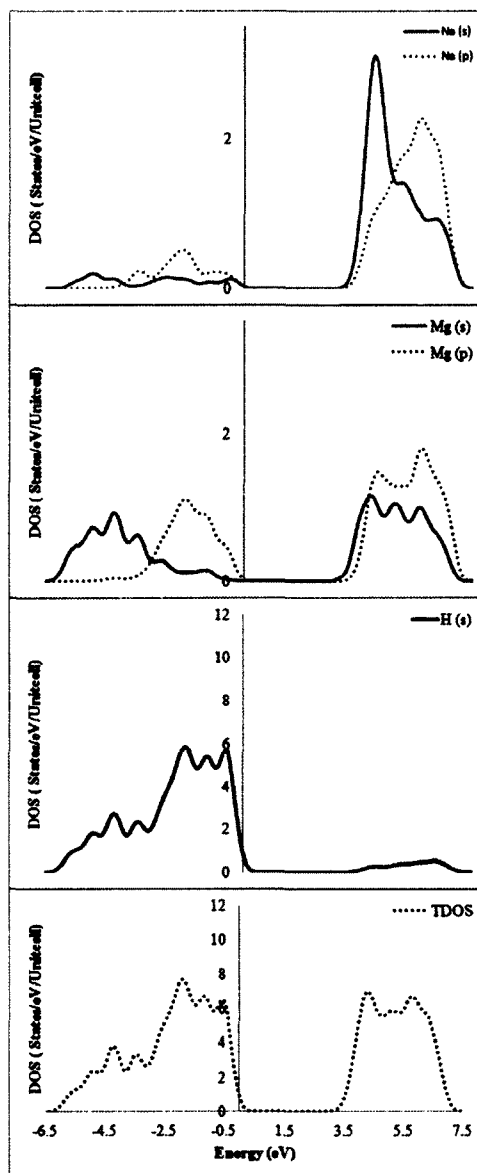


Figure 4-4: From bottom panel to top panel: Total DOS for NaMgH₃ and PDOS for H, Mg, and Na atoms. Black solid and dotted lines represent *s* and *p* states, respectively.

In Figure 4-4, the valence band for pristine NaMgH₃ is shown to consist mainly of the H (*s*) and Mg (*s*) and (*p*) states, with the H (*s*) states and Mg (*s*) states contributing to the lower region of the valence band, which ranges from -3.00 eV to -6.50 eV. On the other hand, a stronger interaction due to (*s-p*) hybridization takes place at the higher region of the valence band, which extends from -3.00 eV up to the Fermi level (set at 0

eV). Therefore, the overlap of H and Mg (*s*), and (*p*) orbitals at the same energy range indicate a stronger interaction between H and Mg atoms.

Figure 4-4 shows a large concentration of H (*s*) orbitals and Mg (*s*) and (*p*) orbitals within the valence band and empty states of Mg (*s*) and (*p*) orbitals in the conduction band. Furthermore, the Na anti-bonding states span over the empty conduction band. The electron density map (see Figure 4-5) and PDOS corroborate the results previously reported by Bouhadda *et al.* [177]; that is, the interaction between Na⁺ and MgH₃⁻¹ species is ionic in nature, and the bonding between Mg and H atoms involves both ionic and covalent schemes.

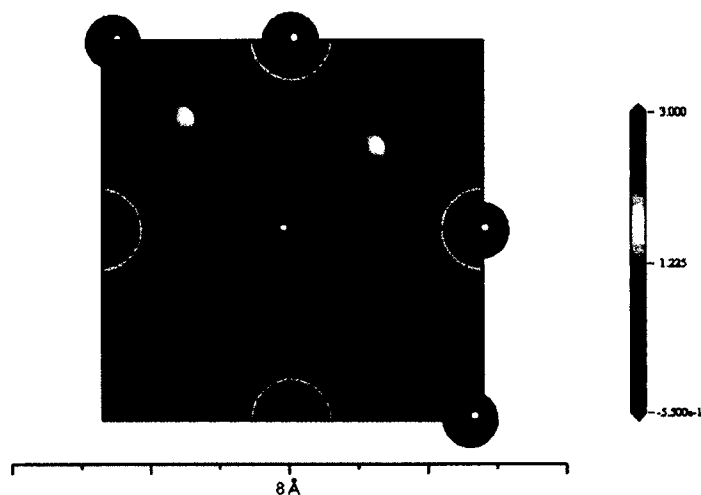


Figure 4-5: Electron density map for the NaMgH₃ crystal. Electron rich zones and electron deficient zones are depicted in red and blue, respectively.

In addition, the bonding characteristic of the NaMgH₃ constituent atoms can be quantified by using the Hirshfeld charge scheme [115]. These charges can corroborate some trends regarding chemical bonding. However, it is important to note that due to the numerical integration precision, the sum of the Hirshfeld charges may deviate from the

analytical net total charge of the structure. For the pristine NaMgH₃ structure, these average charges are as follows: Mg (+0.27), Na (+0.24), and H (-0.17) in pristine NaMgH₃ (see Table 4-2). The positive value of the charges for Mg atoms in NaMgH₃ crystal can be attributed to the electron transfer towards the H atoms, resulting in a negative value of the H atomic charge. This redistribution of the electron cloud is due to the ionic-covalent nature of the chemical bonding between the Mg and the H atoms.

4.1.4 Lattice Vibrations

In the study of solids, not only electronic properties are of importance, but also the lattice movement due to the oscillation of atoms even at 0 K. Particularly, it is of interest to understand the lattice dynamics of NaMgH₃. To the best of our knowledge, the lattice dynamics of NaMgH₃ have seldom been studied from first-principles calculations [165].

As mentioned previously, the vibrational properties such as phonons DOS are calculated based on the finite-difference method as implemented in CASTEP by Montanari *et al.* [149]. The total phonon DOS for NaMgH₃ is presented in Figure 4-6. First, it is important to note that the phonon DOS indicates a stable NaMgH₃ crystal (no imaginary frequencies). The total phonon DOS is plotted as a function of frequencies (cm⁻¹) where three frequency bands can clearly be seen. The lowest frequency band with frequencies in the range of 0-300 cm⁻¹ is dominated by the motion of the heavy atoms (Na and Mg) in the NaMgH₃ crystal. The middle-frequency band with frequencies spanning approximately from 310 cm⁻¹ to 870 cm⁻¹ is attributed to the MgH₆ octahedral group tilt (also referred as librational modes) [25]. This behavior can be expected since it follows changes in the ionic framework of the crystal.

The higher frequency bands in the range between 1030 cm^{-1} and 1390 cm^{-1} are dominated by H vibrations due to the symmetric and asymmetric Mg-H stretch. These vibrational modes agree well with the experimental reported vibrations of 1101 cm^{-1} for the Mg-H stretch [41].

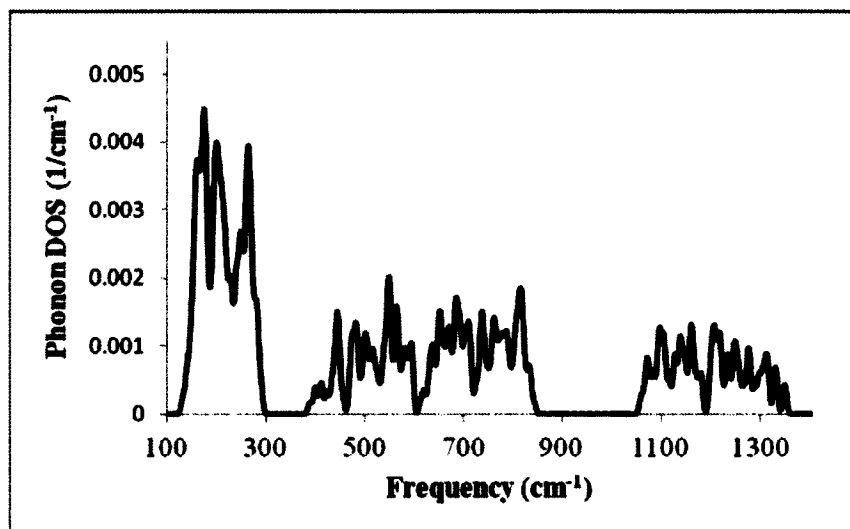


Figure 4-6: Calculated total phonon DOS for NaMgH_3 crystal.

It is important to note that phonon calculations based on first-principles calculations are an accurate and efficient method to investigate the structural and thermodynamic properties of NaMgH_3 hydride.

In addition, the results of a vibrational analysis calculation can be used to compute relevant thermodynamic properties such as H , G , S , and C_m as functions of temperature. The values for these thermodynamic properties of the NaMgH_3 crystal are plotted as a function of temperature in the range of 5 K to 1000 K (see Figure 4-7). It is important to note that contributions from the volume change are neglected as the total change in volume with temperature is negligible in solids for hydrogen storage

applications [166]. The calculated ZPE contribution for the NaMgH₃ crystal structure is 2.1 eV/unit cell.

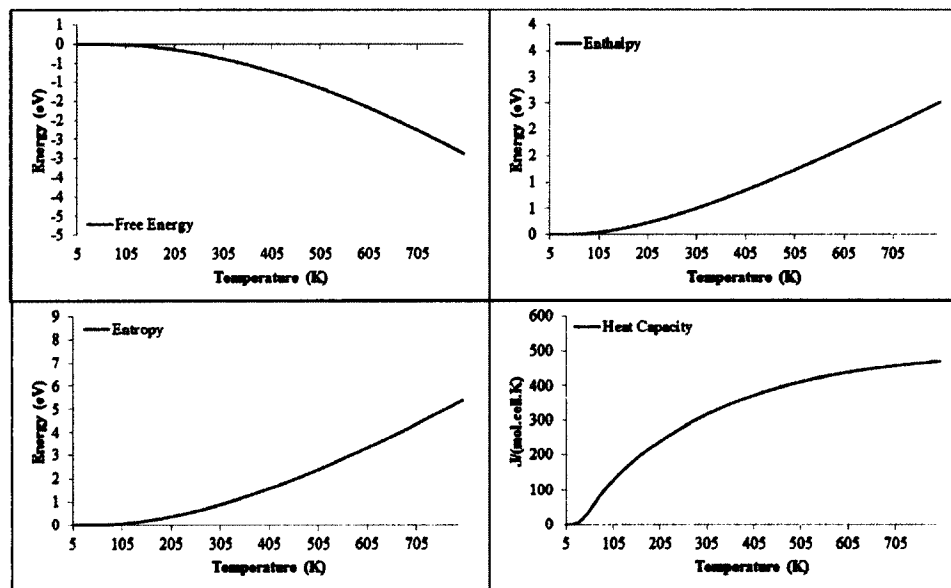


Figure 4-7: Calculated thermodynamic functions NaMgH₃ as a function of temperature. The functions include the Free energy (top-left panel), enthalpy (top-right panel), entropy (lower-left panel) and heat capacity (lower-right panel).

From Figure 4-7, the calculated Free energy value decreases as the temperature of the crystal is increased from 5 K to 800 K. On the other hand, H and S values increase continuously as the temperature is increased. The heat capacity at high temperatures tends to approach the $490 \text{ J mol}^{-1} \text{ K}^{-1}$ value. This result is in accordance with the Dulong-Petit rule for solids [128]. According to this rule, heat capacity value is approximately $3R$ per atom (where R is the universal gas constant). That is, the molar heat capacity is proportional to the number of atoms per formula unit. Therefore, for this solid (20 atoms in the unit cell), the calculated heat capacity value ($490 \text{ J (mol}^{-1} \text{ K}^{-1})$) deviates just by 2% from the expected value from this rule ($500 \text{ J (mol}^{-1} \text{ K}^{-1})$).

In addition to the thermodynamic properties, the efforts to develop adequate hydrogen storage materials requires knowledge of their structures and the thermodynamics of dehydrogenation reactions and formation enthalpy [45]. The change in reaction enthalpy and formation enthalpy (ΔH) is calculated based on the following definition:

$$\Delta H = \sum_{product} E - \sum_{reactant} E \quad \text{Eq. 4-1}$$

Here, E is the total energy of one of the structures belonging to either the product or reactant side. The ZPE correction is obtained through the calculation of vibrational modes. For the pristine crystal, the dehydrogenation route considered is the following:



It is important to remark that the calculated total energy of Mg has also been computed from its optimized ground-state structure. The Mg crystal structure is built from the experimental information reported by Klaveness *et al.* [167]. Similarly, the energy of H_2 is obtained by placing it in a 1 nm cube, optimizing its bond length, and adding the contribution of vibrational modes to its total energy. The calculated ΔH for Equation 4-2 is 81.43 kJ/(mol H_2). Furthermore, the standard enthalpy of formation of NaMgH_3 is calculated to be -139.8 kJ/mol. These ΔH results are well in agreement with the reported values by Ikeda *et al.* [38]. The temperature of dehydrogenation can be estimated by $\Delta H = T\Delta S$. Overall, for complex metal hydrides, ΔS is directly connected to the evolution of molecular hydrogen with a value of 132.2 J/(K mol) [41]. Based on this, the dehydrogenation temperature can be calculated with reliable accuracy. For this reaction, the calculated decomposition temperature (T) is 664 K.

However, considering that a hydrogen desorption enthalpy value of 40 kJ/(mol H₂) is needed for on-board hydrogen storage applications, it seems that modifications are required to bring NaMgH₃ closer to this type of applications [168].

4.1.5 Mechanical Stability

The knowledge of the elastic constants of complex metal hydrides is necessary for many practical applications related to the mechanical properties of the material (specific heat, Debye temperature, and melting point) [169]. The elastic properties of NaMgH₃ are discussed in this section. According to its space group symmetry, orthorhombic NaMgH₃ has nine independent elastic constants: C_{11} , C_{22} , C_{33} , C_{44} , C_{55} , C_{66} , C_{12} , C_{13} , and C_{23} [170]. Depending on the crystal structure, further restrictions on the elastic constants C_{ij} are imposed. The mechanical stability criteria for orthorhombic symmetry is [169]:

$$(C_{22} + C_{33} - 2C_{23}) > 0 \quad \text{Eq. 4-3}$$

$$(C_{11} + C_{22} + C_{33} + 2C_{12} + 2C_{13} + 2C_{23}) > 0 \quad \text{Eq. 4-4}$$

$$C_{11} > 0, C_{22} > 0, C_{33} > 0, C_{44} > 0, C_{55} > 0, C_{66} > 0 \quad \text{Eq. 4-5}$$

The calculated elastic constants are shown in Table 4-3. All the elastic constants satisfy the mechanical stability criteria; hence, NaMgH₃ is mechanically stable at ambient pressure. The acquired elastic constants are in agreement with the available theoretical values (obtained with a linear response method [171]) reported by Bouhadda *et al.* [169].

Table 4-3: Calculated elastic constants for the NaMgH₃ unit cell. Elastic constants reported by Bouhadda *et al.* [169] are listed in parentheses for comparison with the calculated values in this dissertation.

Elastic Constant (GPa)
$C_{11} = 77.95$ (76.23)
$C_{22} = 71.29$ (67.42)
$C_{33} = 81.90$ (80.28)
$C_{44} = 33.68$ (33.34)
$C_{55} = 24.52$ (23.40)
$C_{66} = 33.35$ (33.59)
$C_{12} = 20.92$ (19.80)
$C_{13} = 12.59$ (10.10)
$C_{23} = 21.54$ (19.94)

Furthermore, from the results of the elastic stiffness, the bulk modulus (B), shear modulus (G), Young's Modulus (E), and Poisson's ratio (ν) are calculated using the Voigt-Reuss-Hill average scheme [172]. The Voigt-Reuss-Hill scheme computes an average value for the elastic constants. The calculated properties are shown in Table 4-4, Table 4-5, and Table 4-6.

Table 4-4: Calculated Bulk and Shear Modulus for the NaMgH₃ unit cell. The calculations are calculated following the Voigt-Reuss-Hill scheme.

Elastic Constants (GPa)	Voigt	Reuss	Hill
Bulk Modulus	37.92	37.90	37.91
Shear Modulus	30.05	29.39	29.72

Table 4-5: Young's Modulus for the NaMgH₃ unit cell along its principal axes.

Axis	Young's Modulus (E) (GPa)
x	71.30
y	61.55
z	74.85

Table 4-6: Poisson Ratios for the NaMgH₃ unit cell along principal axes.

Axis	Poisson Ratios (ν)
E_{xy}	0.268
E_{yx}	0.231
E_{zx}	0.08
E_{xz}	0.08
E_{yz}	0.22
E_{zy}	0.27

The calculated values are in agreement with the work of Bouhadda *et al.* [169] and Vajeeston *et al.* [173]. It is important to note that no experimental information is available for direct comparison. The value of Young's Modulus for the [001] direction is the highest of all directions. The value of Young's Modulus shows that orthorhombic NaMgH₃ exhibits a large elastic anisotropy along this plane. This large elastic anisotropy is considered to be closely related to the inter-atomic bonding strength [174].

Indeed, this is corroborated by calculating the shear anisotropic factors, where these factors provide a measure of the degree of anisotropy in the bonding between atoms in different planes [175]. The shear anisotropic factors are calculated as follows:

$$A_1 = \frac{4C_{44}}{(C_{11} + C_{33} - 2C_{13})} \quad \text{Eq. 4-6}$$

$$A_2 = \frac{4C_{55}}{(C_{22} + C_{33} - 2C_{23})} \quad \text{Eq. 4-7}$$

$$A_3 = \frac{4C_{66}}{(C_{33} + C_{33} - 2C_{33})} \quad \text{Eq. 4-8}$$

Here, A_1 , A_2 , and A_3 define the shear anisotropic factors for the (100), (010), (001) shear planes, respectively. The calculated values are as follows: $A_1 = 1.00$, $A_2 = 0.89$, and $A_3 = 1.24$. Similar to Young's Modulus result, the shear anisotropy factors indicate that the elastic anisotropy for (001) plane (shear planes between [110] and [010] directions) is larger than for the rest [169]. Indeed, the (001) plane in NaMgH₃ is composed of a mix of Na and Mg atoms, therefore contributing to its stability.

4.2 Summary

In this chapter, first-principles calculations of structural, electronic, thermodynamic, and elastic properties of the NaMgH₃ crystal structure are investigated. The optimized lattice parameters of crystalline NaMgH₃, KMgH₃, NaH, and MgH₂, are obtained at the GGA-PBE theory level. The values for the calculated lattice parameters are well in agreement with experimental findings. The relevant atomic bonds are calculated to validate the GGA-PBE theory level for these materials. The calculated average distance for Na-Mg, Mg-H, and Na-H bonds are 3.33 Å, 1.98 Å, and 2.28 Å,

respectively. The average Na-Mg-Na angle is calculated to be approximately 68° . The tilting angle of the MgH_6 octahedral group in the optimized unit cell is 13.68° .

Moreover, a DFT study of the NaMgH_3 crystal under hydrostatic pressure is conducted in this chapter. The NaMgH_3 lattice parameters as functions of external pressure are investigated by optimizing the pristine crystal structure subjected to hydrostatic pressures in the range of 10 to 40 GPa. At the 10 GPa pressure, the Mg-H average bond distance is shortened to 1.87 Å, whereas at the 40 GPa pressure the Mg-H average bond distance is even shorter at an average distance of 1.72 Å. This shortened bond distance is due to the increasing association of Mg with H atoms. This bond contraction is corroborated by the Hirshfeld charge analysis.

Furthermore, the plots for the DOS and PDOS show that the crystal structure of NaMgH_3 has a band gap value of approximately 3.50 eV. From the DOS and PDOS plots, a stronger interaction due to (*s-p*) hybridization is visible at the higher region of the valence band, which extends from -3.00 eV up to the Fermi level. From the Hirshfeld analysis, the charges for Mg atoms in NaMgH_3 crystal can be attributed to the electron transfer towards H atoms; resulting in a negative value of the H atomic charge. This redistribution of the electron cloud is attributed to the ionic-covalent nature of the chemical bonding between the Mg and H atoms.

From the vibrational analysis, three frequency bands are identified. The lowest frequency band is dominated by the motion of the heavy atoms, the middle-frequency bandwidth is attributed to the MgH_6 octahedral group tilt, and the higher frequency bands are dominated by H vibrations due to the symmetric and asymmetric Mg-H stretch. Relevant thermodynamic properties such as H , G , S , and C_m are reported as functions of

temperature. Here, the calculated Free energy values are reported from the 5 K to 800 K temperature range. In this study, Free energy values decrease as the temperature of the crystal is increased from 5 K to 800 K. On the other hand, H and S values increase continuously as the temperature is increased.

The heat capacity at high temperatures tends to approach a value that is in accordance with the Dulong-Petit rule for solids ($490 \text{ J mol}^{-1} \text{ K}^{-1}$). From the thermodynamics of the first-step decomposition, the enthalpy change and standard enthalpy formation are calculated. The values for the enthalpy change and standard formation are calculated to be $81.43 \text{ kJ}/(\text{mol H}_2)$ and -139.8 kJ/mol , respectively. From these values, the calculated decomposition temperature is calculated to be 664 K. From the study of mechanical properties, it is determined that the NaMgH_3 crystal exhibits large anisotropy along the (001) plane due to the intercalated bonding of Na, Mg, and H atoms along this plane. These results are relevant since they provide a starting reference point for future calculations with the goal of producing a material suitable for on-board hydrogen storage applications.

CHAPTER 5

DFT STUDY OF DOPANT EFFECT

As mentioned previously, NaMgH₃ is a promising hydrogen storage material with a high volumetric hydrogen density. However, its high temperature of hydrogen desorption limit its wide-scale application. In this chapter, the influence of addition of dopants (25% mol and 6.25% mol doping concentrations) on the structure and electronic properties of NaMgH₃ is studied via first-principles calculations. The thermodynamics of the first dehydrogenation step due to doping is addressed. In addition, the effect of point-defects on the hydrogen storage properties of NaMgH₃ is studied.

5.1 Results

5.1.1 TM-doped NaMgH₃ Crystal

Figure 5-1 shows the TM-doped unit cell of NaMgH₃, whereas it has been mentioned previously, the crystal unit cell contains 20 atoms. Here, spheres in green, purple, red, and gray represent Mg, Na, TM, and H atoms, respectively. Note, the red spheres show the position where the Na atom was substituted by a TM. This substitution indicates a 25% mol doping concentration.

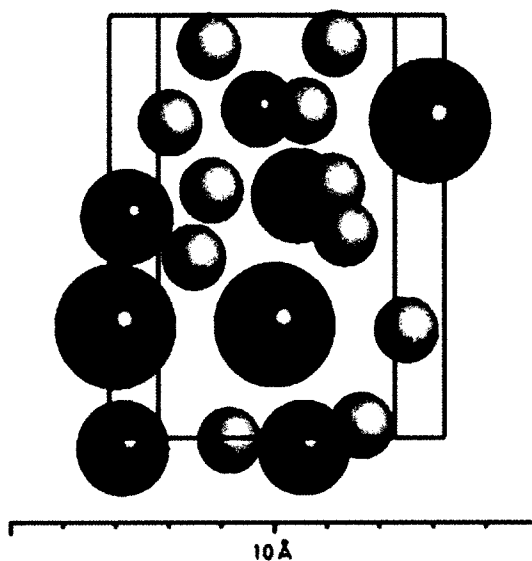


Figure 5-1: The 25% mol TM-doped perovskite crystal structure of NaMgH_3 containing 20 atoms. The red sphere represents the TM at the Na lattice site.

The optimized lattice parameters of $\text{Na}_{3/4}\text{TM}_{1/4}\text{MgH}_3$ (TM = Ti, V, Cu, and Zn) are given in Table 5-1. It is important to note that 1 TM substitution per 4 formula units of NaMgH_3 results in 25% mol TM doping concentration per 1 mole of NaMgH_3 . Based on these lattice parameters values of the doped structures, it is shown that the replacement of $\frac{1}{4}$ of Na atoms by Ti, V, Cu, and Zn dopants do not lead to a significant change of the unit cell volume (maximum change is reported for the Ti-doped model with an approximate 6% decrease in unit cell volume). The Ti dopant attracts one hydrogen atom from each of the adjacent Mg atoms and the corresponding Mg-H average bond length is increased to 2.05 Å. Therefore, the Ti dopant becomes coordinated to six H atoms with an average bond distance of 1.90 Å in an octahedral configuration. Notice that the Ti-H bond length is shorter than the original Na-H bond distance causing the volume to decrease. Similarly, for the V-doped structure, the V dopant becomes coordinated with an additional H atom when compared to the Ti-doped model with an average bond length

of 1.81 Å. This results in an average Mg-H bond length of 2.04 Å. On the other hand, for the Cu-doped model, the Cu dopant is only coordinated to three H atoms with an average bond distance of 1.73 Å. Despite this reduced interaction, the average Mg-H bond length is 1.95 Å. Finally, the Zn-doped model shows the Zn dopant coordinating with six neighboring H atoms with an average Zn-H bond length of 1.94 Å and an average elongation in the Mg-H bond of approximately 2.03 Å.

Table 5-1: Calculated average bond distances, lattice parameters, and cell volume for pristine NaMgH₃ and 3d TM-doped NaMgH₃ crystal models at the GGA-PBE theory level and 25% mol doping concentration.

Bond Length (Å)	Models				
	Pristine	Ti	V	Cu	Zn
Na-Mg	3.33	3.43	3.47	3.12	3.44
Mg-H	1.98	2.05	2.04	1.95	2.03
Na-H	2.32	2.23	2.29	2.25	2.28
TM-H		1.90	1.81	1.73	1.94
TM-Mg		3.03	2.95	2.69	3.19
Lattice Parameters (Å)					
<i>a</i>	5.463	5.285	5.483	5.580	5.484
<i>b</i>	7.703	7.173	7.724	7.713	7.724
	5.411	5.654	5.364	5.274	5.364
<i>c</i>					
Cell Volume, V (Å ³)	227.12	213.82	212.069	226.694	225.65
V/V ₀	1	0.941	0.934	0.998	0.993

Next, the Free energy (G) is used to describe the thermodynamic stabilities of the pristine and TM-doped NaMgH₃ crystal at elevated temperatures. Figure 5-2 shows the

calculated Free energy values for pristine NaMgH₃, Ti-doped NaMgH₃, V-doped NaMgH₃, Cu-doped NaMgH₃, and Zn-doped NaMgH₃ as a function of temperature from 300 K to 700 K. From Figure 5-2, it can be seen that the Free energy values gradually decreased according to the following sequence: Cu > Ti > V > Zn > Pristine. Therefore, the smaller the Free energy value is, the better the thermal stability of the material is. Hence, the calculated Free energy values show that the thermal stabilities of the doped crystal gradually decrease in the following order: Pristine < Zn < V < Ti < Cu. Therefore, based on this plot, it is possible to destabilize the crystal with addition of TM dopants. At this doping concentration, Ti and Cu are the most useful.

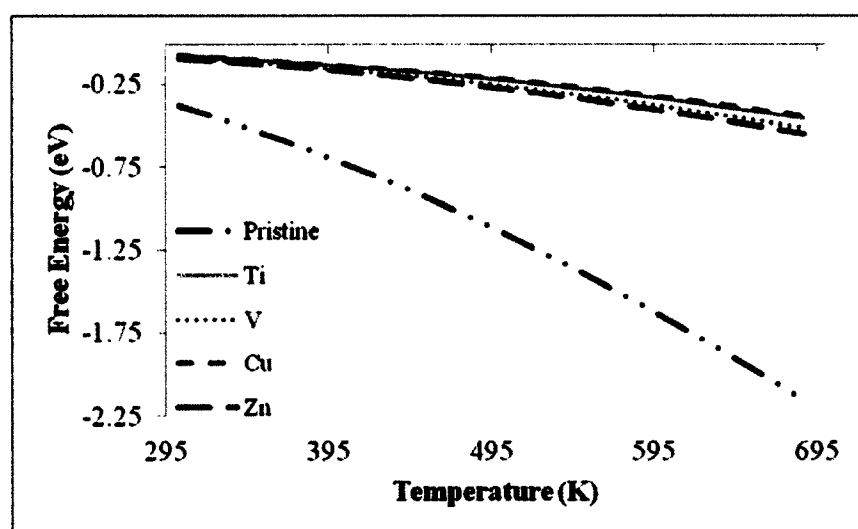


Figure 5-2: The Free energies of pristine and TM-doped NaMgH₃ functions of temperature.

Moreover, the enthalpies of decomposition (at 298 K including ZPE) for the first dehydrogenation step are obtained by calculating the energy difference between the calculated total energy of the TM-doped NaMgH₃ crystal and the calculated total energy

of the reactants (NaH, Mg, and H₂). The $\Delta H(298\text{ K})$ values and calculated temperature for the first dehydrogenation step are presented in Figure 5-3.

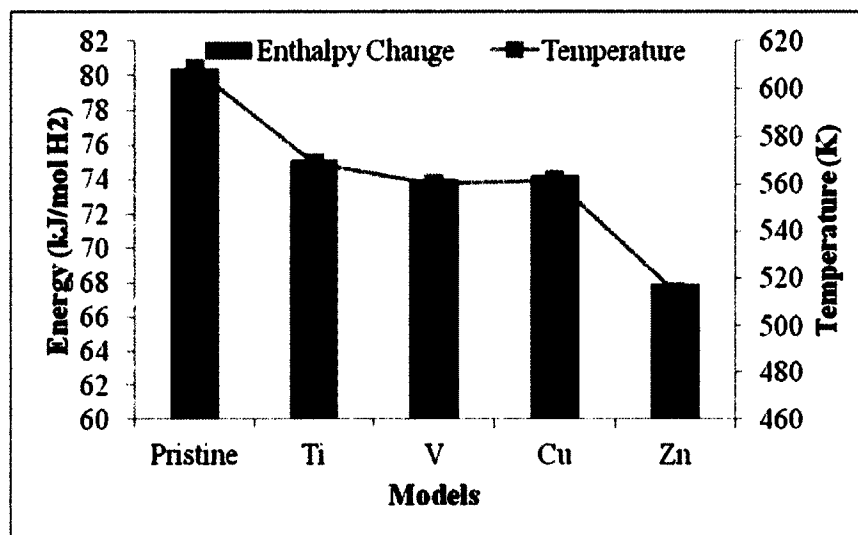


Figure 5-3: Calculated $\Delta H(298\text{ K})$ values for the first decomposition reaction of TM-doped NaMgH₃ crystal structure. The solid gray line represents the calculated decomposition temperature.

From Figure 5-3, the smallest $\Delta H(298\text{ K})$ value corresponds to the Zn-doped model (67.97 kJ/(mol H₂)), while the highest energy for the TM dopants is calculated for the Ti-doped model with an $\Delta H(298\text{ K})$ value of 75.16 kJ/(mol H₂). These calculated $\Delta H(298\text{ K})$ values can assist future experiments on nano-structured NaMgH₃. Even though all the TM dopants are able to decrease the decomposition enthalpy of the NaMgH₃ crystal, it is important to remark that none of these values are close to the desired target (40 kJ/(mol H₂)). The decomposition temperatures are in the range between 608 K and 514 K. As is expected, a large decrease in the decomposition temperature is not reported for these models due to the high calculated enthalpy values. However, as mentioned before, it is important to consider the trends and generalities of these calculations. Here, the Zn dopant shows to be the most effective TM dopant at this

doping concentration, possibly reducing the decomposition temperature by 100 K for the first dehydrogenation step of the NaMgH₃ crystal.

5.1.2 TM-doped NaMgH₃ Supercell

Despite the greater mobility of hydrogen atoms (relative to the MgH₂ crystal), understanding of the effect of the TM-doped NaMgH₃ crystal is a critical step toward its prospective use as hydrogen storage material. To fulfill this need, the search for an optimal Mg-based alloy has primarily been focused on hydride formation enthalpy with addition of TM [55, 58]. However, recently, it has been reported that there exist a correlation between the experimental hydrogen desorption temperature and the cohesive energy values calculated in light complex metal hydrides (LiAlH₄ and NaAlH₄) [174]. In view of the above situation, cohesive energy trends are expected to illustrate the effect of the TM on the hydrogen storage properties of bulk NaMgH₃. Here, cohesive energy is defined as the energy that is released when the crystal is decomposed into single atoms. Hence, the more negative the cohesive energy is, the higher the stability is [175].

It is important to note that the theoretical cohesive energy value often depends on the reference states of elements involved. Therefore, in this work, free neutral atoms are used as a reference to calculate cohesive energies. Note, the model used for these calculations contain 80 atoms. Calculations of cohesive energies (ΔE_{CE}) are then performed according to the following equation:

$$\Delta E_{CE} = [E_{TOT}((TM/Na)Na_{15}Mg_{16}H_{48}) - 15E(Na) - 16E(Mg) - 48E(H) - E(TM)]/80$$

Eq. 5-1

Here, $E_{TOT}((TM/Na)Na_{15}Mg_{16}H_{48})$ is the total energy of the TM-doped or pristine supercell models. Then, $E(Na)$, $E(Mg)$, $E(H)$, and $E(TM)$ are the energies of free neutral

atoms of Na, Mg, H, and TM, respectively. Calculation of atomic energies is obtained by placing the atoms in a 1 nm cube.

The substitution of Na with TM takes place at the center of a supercell model with the following cartesian coordinates: ($x = 5.192$, $y = 5.792$, $z = 5.289$). To simulate the supercell structure, $2 \times 1 \times 2$ units of a NaMgH_3 crystal (to avoid drastic geometry changes arising from the substitution of a Na atom) are used with a total of 80 atoms (see Figure 5-4).

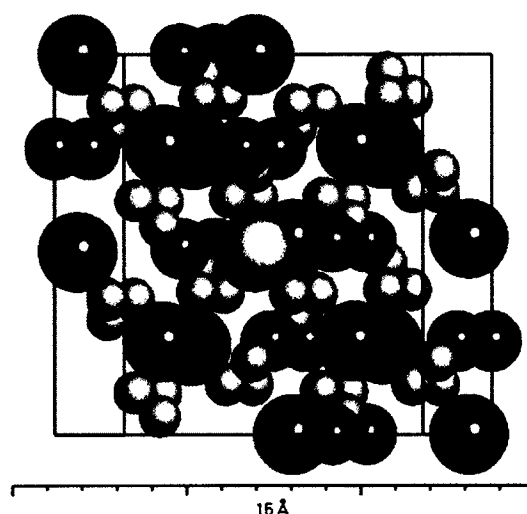


Figure 5-4: Supercell NaMgH_3 model. The yellow sphere represents the substituted Na atom.

As shown in Table 5-2, the cohesive energy values of the Ti-doped (0.74 eV/atom) and Zn-doped (-2.90 eV/atom) models suggest an easier hydrogen release from these models with respect to the pristine hydride. It is important to note that negative cohesive energies for the rest of the models show their energetic stabilization. For the Zn-doped models this stabilization is less than for the pristine model (as indicated by its higher cohesive energy with respect to the pristine hydride). Due to these results (Ti and

Zn as best dopants to destabilize the hydride), it is interesting to analyze the effect of early TM and late TM along the $3d$ periodic block. Herein, the focus is on the effect of early TM such as Ti and V, and the effect of late TM such as Cu and Zn on hydrogen storage properties.

Table 5-2: Cohesive energy per atom for the pristine and $3d$ -TM doped NaMgH₃ supercell.

Models	ΔE_{CE} (eV)
Pristine NaMgH₃	-2.93
Sc-doped NaMgH₃	-2.97
Ti-doped NaMgH₃	0.74
V-doped NaMgH₃	-2.99
Cr-doped NaMgH₃	-2.99
Mn-doped NaMgH₃	-2.98
Fe-doped NaMgH₃	-3.00
Ni-doped NaMgH₃	-2.97
Co-doped NaMgH₃	-2.99
Cu-doped NaMgH₃	-2.94
Zn-doped NaMgH₃	-2.90

The cohesive energy value due to the doping of Ti is 0.74 eV/atom, implying that the Ti-doped NaMgH₃ supercell model is more destabilized than the pristine case where no dopant is inserted. Meanwhile, the cohesive energy value due to the insertion of V and Cu dopants is -2.99 eV/atom and -2.94 eV/atom, respectively. On the other hand, the cohesive energy due to the use of the Zn dopant shows a slightly higher value (relative to the pristine model) of -2.90 eV/atom. This higher cohesive energy value may be related

to the electronic configuration of Zn with its fully occupied orbital states. The local geometry of the TM-doped NaMgH₃ supercell models can provide insight into the stability of the material. Charge distribution schemes are often used to study the relative bonding strength between atoms. Figure 5-5 shows the average distances of the Mg-H, TM-H, and TM-Mg bonds for the pristine and TM-doped NaMgH₃ supercell models at the 6.25% mol doping concentration.

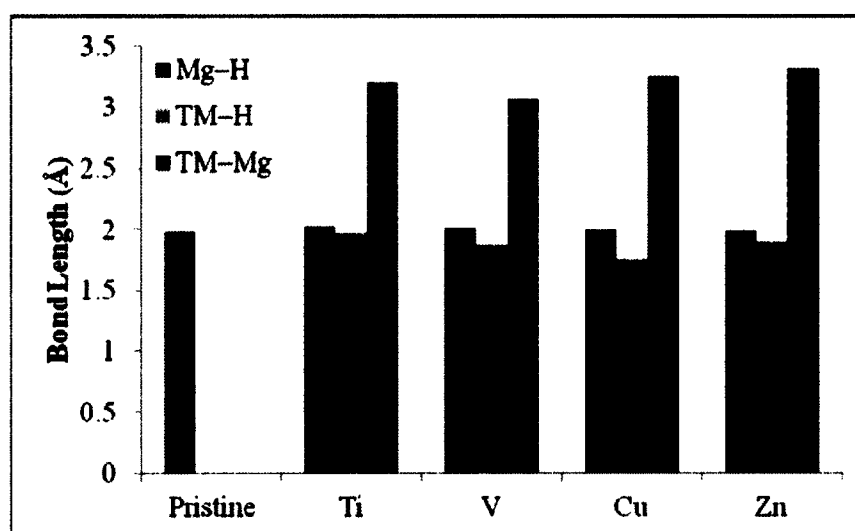


Figure 5-5: Bond distances of the pristine and TM-doped NaMgH₃ supercell models. Bond distances reported are for the nearest neighbors.

From Figure 5-5, it can be seen that the Ti-doped NaMgH₃ supercell model shows the longest Mg-H bond elongation (0.04 Å). Similarly, the V-doped NaMgH₃ supercell model shows a Mg-H bond elongation of 0.03 Å. From Figure 5-5, it can be seen that the late TM show the least elongation of the Mg-H bond. For the Cu-doped model and Zn-doped model, the Mg-H bond elongate slightly: 0.02 Å and 0.01 Å, respectively.

Furthermore, for the TM-H bond distances, the Ti-H average bond distance is 1.97 Å, the V-H average bond distance is 1.87 Å, and the Cu-H average bond distance is

1.76 Å. On the other hand, for the Zn-doped model, the nearest H atoms are located at an average distance of 1.90 Å. In addition, the TM-Mg bond fluctuates; the reported distances are in the range of 3.07 Å (for the V-Mg bond) to 3.32 Å (for the Zn-Mg bond). Likewise, the Ti-Mg and Cu-Mg bonds result in 3.20 Å and 3.25 Å average distances, respectively. It is important to note that the elongation of Mg-H and TM-H bond lengths is suggestive of an easier hydrogen release and consequently reduced hydrogen removal energy.

Table 5-3 shows the Mulliken charge and population analysis for the pristine and TM-doped supercell models. The Mulliken population scheme is a common approach to count the electrons associated with a given atom. Although, it is important to note that the Mulliken population scheme is more qualitative than quantitative, due to the scheme's sensitivity to the atomic basis set employed.

Table 5-3: Mulliken population analysis for the TM-doped NaMgH₃.

Model	Mulliken Charges (<i>e</i>)	Bonds	Overlap Population (<i>e</i>)
(Ti)NaMgH₃	(Ti) -0.14	Ti-Mg	0.03
	(Mg) 0.94	Mg-H	0.03
	(H) -0.53	Ti-H	0.51
	(Na) 0.72		
(V)NaMgH₃	(V) -0.14	V-Mg	0.07
	(Mg) 0.95	Mg-H	0.04
	(H) -0.54	V-H	0.49
	(Na) 0.72		
(Cu)NaMgH₃	(Cu) -0.36	Cu-Mg	-0.03
	(Mg) 0.96	Mg-H	0.04
	(H) -0.54	Cu-H	0.72
	(Na) 0.74		
(Zn)NaMgH₃	(Zn) -0.30	Zn-Mg	-0.05
	(Mg) 0.97	Mg-H	0.04
	(H) -0.54	Zn-H	0.71
	(Na) 0.73		

From Table 5-3, the Mg-H bond is ionic in all the models with an average overlap population charge in the range between $0.03e$ and $0.04e$. Similar ionic bonds are reported for Ti-Mg and V-Mg with average overlap charges of $0.03e$ (for Ti-Mg bonds) and $0.07e$ (for V-Mg bonds). The overlap charge for Cu-Mg and Zn-Mg bonds show an anti-

bonding nature with $-0.03e$ and $-0.05e$ values, respectively. Similarly, for the early TM dopants, the TM-H bonds show an ionic-covalent nature with values ranging from $0.49e$ (for the V-H bond) to $0.51e$ (for the Ti-H bond). On the other hand, the late TM-H bonds (Cu-H and Zn-H) show a more covalent nature with higher average overlap charges of $0.71e$ and $0.72e$, respectively. Similarly, from the calculated Mulliken effective charges one can see that the bonding scheme of the TM-doped supercell models do not exhibit simple ionic or covalent character upon insertion of TM dopants. In fact, the bonding interaction in these supercell models is quite complicated, leading to a possible formation of a TM-Mg_x-H_y structure (where x and y represents the number of Mg and H atoms in the structure). Particularly, the formation of TM-Mg_x-H_y structures is as follows: Ti-Mg₂-H₅, V-Mg₂-H₅, Cu-Mg₂-H₃, and Zn-Mg₂-H₃.

The analysis according to the electron density difference field along the (100) plane (shown in Figure 5-6) reveals the charge redistribution for TM-doped NaMgH₃ supercell models. The electron density difference field is plotted on a color scale of 16 bands. Moreover, the blue region represents a depletion of electrons (positive values) and the red region represents an electron-rich region (negative values). Mixed regions are shown in green. These fields are plotted from $-0.05 e/\text{\AA}^3$ to $0.03 e/\text{\AA}^3$. The charge density difference is obtained in the following manner:

$$\rho_{\text{difference}} = \rho_{\text{TM/bulk}} - \rho_{\text{TM}} - \rho_{\text{bulk}} \quad \text{Eq. 5-2}$$

Here, $\rho_{\text{TM/bulk}}$, ρ_{TM} , and ρ_{bulk} represent the charges corresponding to the TM-doped NaMgH₃ supercell models, the free TM, and the pristine NaMgH₃ supercell model, respectively. All the plots display a dense electron cloud around the H atoms and a weakly smeared cloud connecting to the neighboring atoms.

Therefore, the electron density difference maps show the mixed ionic-covalent bonding of the structure, where the charges are highly localized around the H atoms.

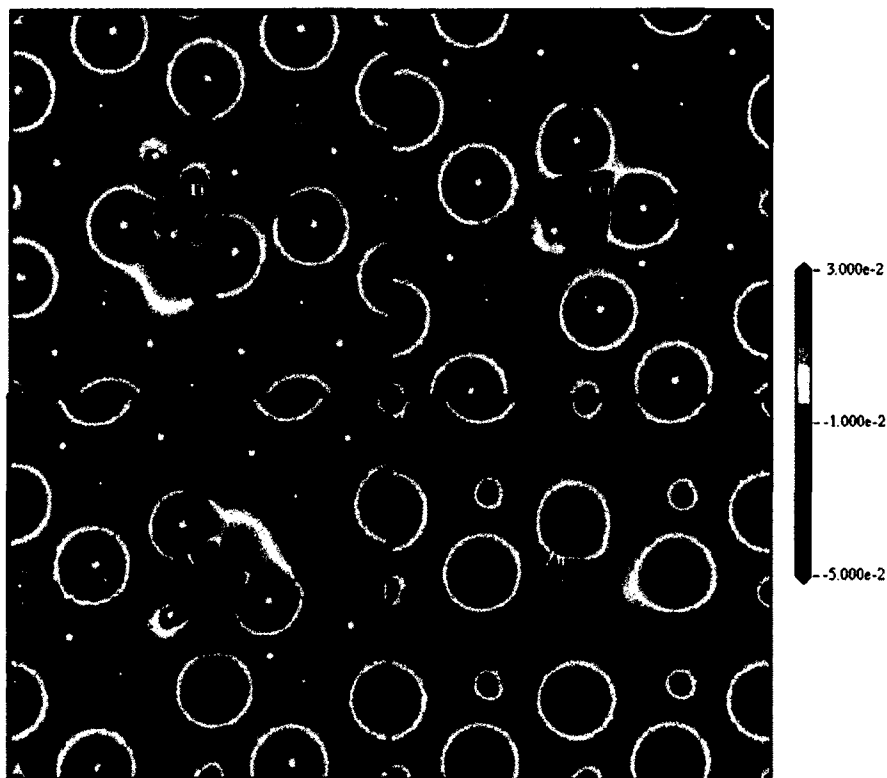


Figure 5-6: Calculated electron difference plots for TM-doped NaMgH_3 supercell models. Here the top-left, top-right, bottom-left, and bottom-right panels represent the electron density difference map for the Ti-doped model, Cu-doped model, V-doped model, and Zn-doped model, respectively.

In addition, maps for Ti and V-doped models show penetration of red and blue regions around their vicinity representing the ionic-covalent nature of their bonds with neighboring atoms. On the other hand, the Cu and Zn-doped models show a depletion of electrons with spherical symmetry along the (001) plane indicative of their ionic bonding with Mg atoms. Moreover, the DOS provides further insight into the bonding and structural stability of TM-doped NaMgH_3 supercell models. It is important to note that DOS plots in this section show the contributions from (*s*), (*p*), or (*d*) orbitals of the

different atoms, resulting in the peaks observed in the conduction and valence bands at different energy levels. The DOS and PDOS plots for TM-doped NaMgH₃ supercell models are shown in

Figure 5-7 through Figure 5-10. From these figures, it is evident that the main difference in the DOS between the pristine NaMgH₃ and the TM-doped NaMgH₃ supercell models is the existence of (*d*) state peaks. Also, the position of these (*d*) state peaks is important for the overall stability of the structure. The most prominent (*d*) peaks are located near the Fermi level (except for the Zn-doped model). For the Zn-doped model, the prominent (*d*) peak is “buried” at the bottom of the valence band at the -9 eV level. In addition, it can be seen from the plots that the main bonding peaks of the valence band for Ti-doped, V-doped, and Zn-doped structures fall within the energy levels of -9 eV to -2 eV. On the other hand, the Cu-doped structure shows the main bonding peaks ranging from -9 eV to 0 eV.

For the Ti-doped structure (see Figure 5-7), the bonding peaks in the valence band mainly originates from the contribution of electrons belonging to the Ti (*d*), Mg (*p*), and H (*s*) orbitals. The (*s-p*) bonding peaks between Mg and H atoms appear in the energy range between -2.0 and -6.0 eV. Therefore, the DOS for Ti can be rationalized in the following way: upon Ti-doping insertion, additional electrons are introduced, resulting in the involvement of Ti (*d*) electrons with H (*s*) electrons. Consequently, fewer electrons are available for Mg-H bonding (confirmed by the elongation in Mg-H bond distances). It is important to note that due to the contribution of electrons belonging to the (*d*) orbital, the band gap is reduced for the Ti-doped model.

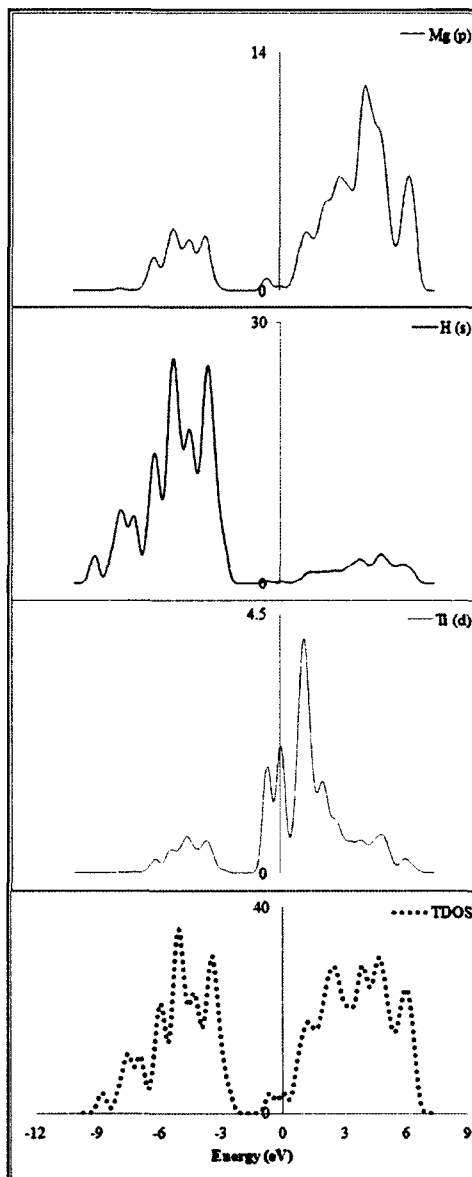


Figure 5-7: From bottom panel to top panel: Total DOS for Ti-doped NaMgH₃ and PDOS for Ti, H, and Mg atoms.

Also, the V-doped structure shows a similar bonding scheme to the Ti-doped model (see Figure 5-8). In the valence band, the bonding peaks between -2.0 eV and -6.0 eV energy levels are contributed mainly by Mg (*p*) and H (*s*) orbitals and a small contribution from V (*d*) orbitals.

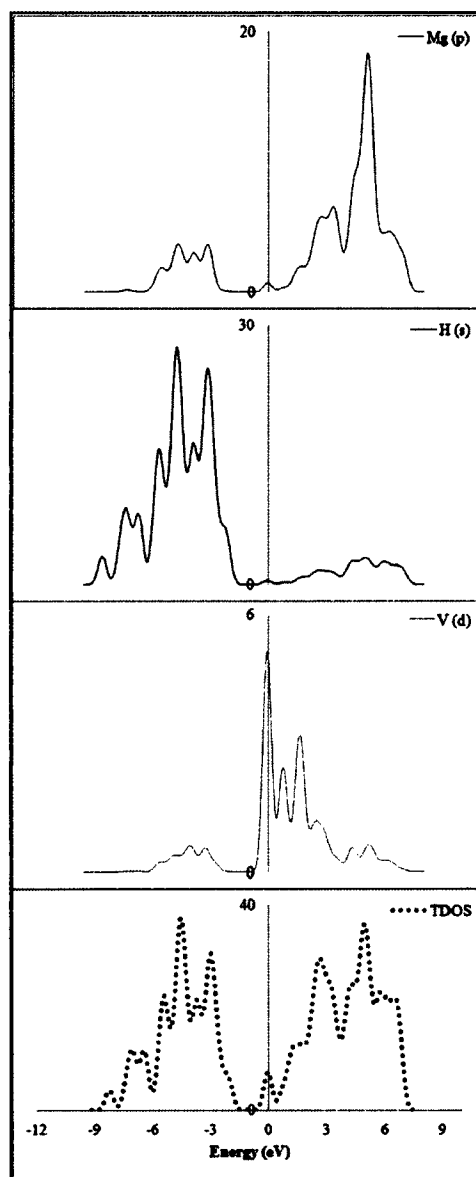


Figure 5-8: From bottom panel to top panel: Total DOS for V-doped NaMgH₃ and PDOS for V, H, and Mg atoms.

From Figure 5-9, Cu (*d*) electrons contribute to the main bonding peaks near the Fermi level. The highest bonding peak, located at -3.0 eV, shows a small contribution from Cu (*d*) orbitals, but it also contains Mg (*p*) and H (*s*) electrons. It is important to note that the Cu-doped model shows no contribution of (*d*) orbitals to the conduction band.

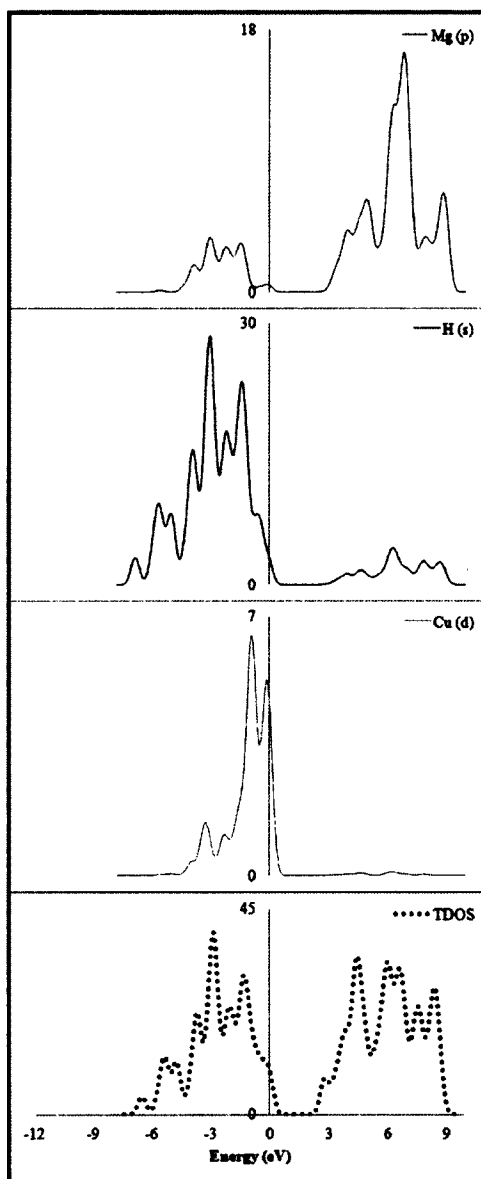


Figure 5-9: From bottom panel to top panel: Total DOS for Cu-doped NaMgH₃ and PDOS for Cu, H, and Mg atoms.

For the Zn-doped model (see Figure 5-10), the main bonding peaks near the Fermi energy are dominated by (*p*) and (*s*) orbitals while the highest bonding peak, located at -6.0 eV as mentioned before, is the result of the bonding between (*d*) and (*s*) orbitals with a very small contribution from the (*p*) orbital. As a consequence, there is less overlap

between the valence states of Zn and Mg (as shown in Zn-Mg nearest neighbor measurements).

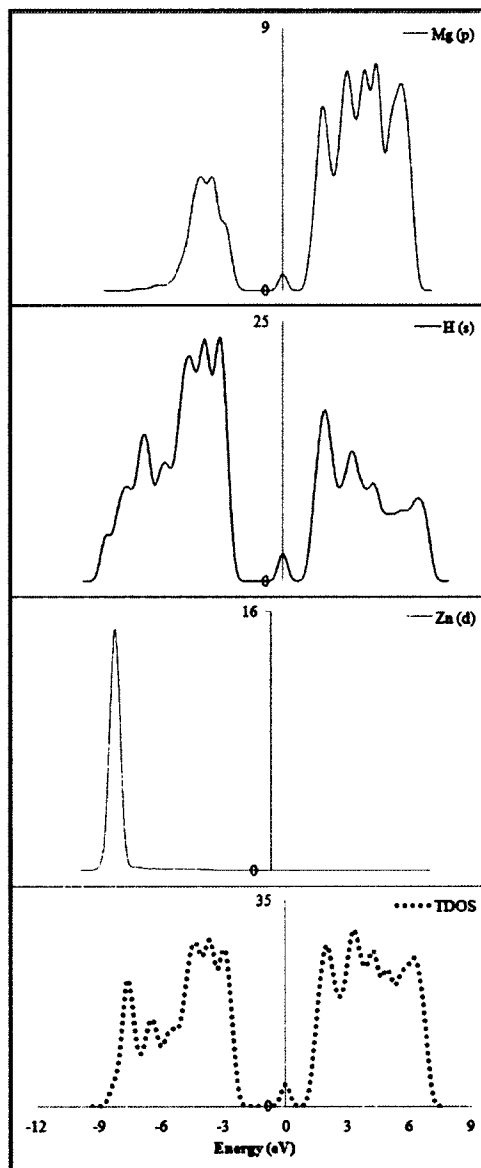


Figure 5-10: From bottom panel to top panel: Total DOS for Zn-doped NaMgH₃ and PDOS for Zn, H, and Mg atoms.

As mentioned previously, Ti-doping causes an elongation in the Mg-H, here, this effect is quantified in terms of hydrogen removal energy. The methodology followed is

similar to the one presented by Dathar *et al.* [178], where it is reported that Ti has a high probability to substitute Na at the bulk and surface lattice sites. In Figure 5-11, yellow spheres represent the Na and Mg atoms that are either removed or substituted. The simulations are done in several steps; first, supercell models are constructed with a Na or Mg atom missing in order to simulate vacancies at the Na and Mg sites, respectively. Then, the preferred site is chosen to perform a Ti substitution (by replacing an atom at the bulk lattice site). Third, the hydrogen removal energy is calculated for the pristine and Ti-doped NaMgH_3 .

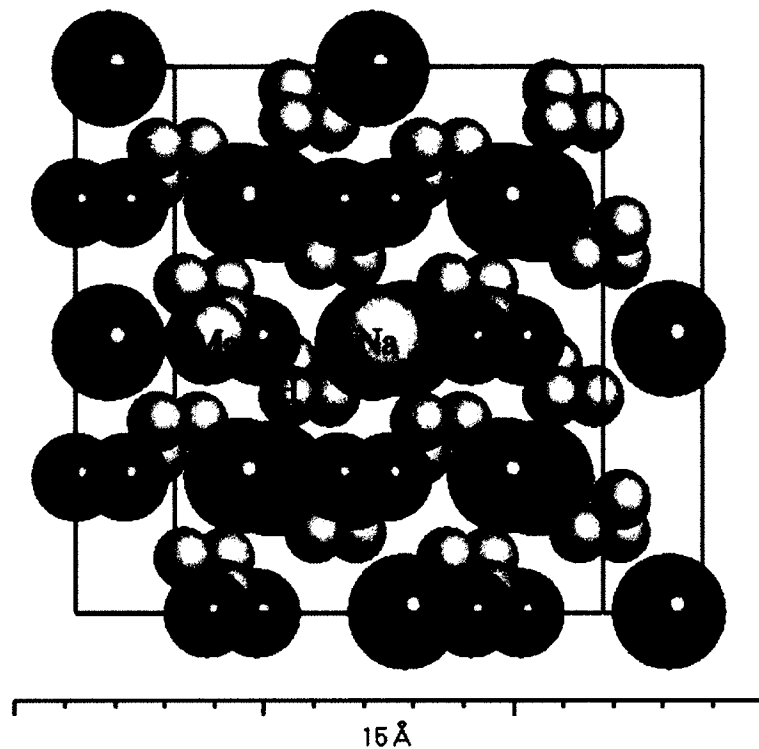


Figure 5-11: Supercell model for NaMgH_3 . The replaced Na, and Mg atoms are shown as yellow spheres.

To determine the energy cost to create these point-defect vacancies (ΔE_{PD}), the total electronic energy of the systems is calculated according to Equation 5-3:

$$\Delta E_{PD} = [E(\text{Na}_{16-x}\text{Mg}_{16-y}\text{H}_{48-z}) + xE(\text{Na}) + yE(\text{Mg}) + z/2E(\text{H}_2)] - [E(\text{Na}_{16}\text{Mg}_{16}\text{H}_{48})]$$

Eq. 5-3

Here, $E(\text{Na}_{16-x}\text{Mg}_{16-y}\text{H}_{48-z})$ is the total energy of the supercell with a Na-vacancy (x), Mg-vacancy (y), or an H-vacancy (z). Here, $E(\text{Na})$ is the total energy of a Na atom, $E(\text{Mg})$ is the total energy of a Mg atom, $E(\text{H}_2)$ is the total energy of an H_2 molecule, and $E(\text{Na}_{16}\text{Mg}_{16}\text{H}_{48})$ corresponds to the total energy of the pristine NaMgH_3 supercell containing 80 atoms. It is important to note that positive values of the above energies imply that energy will be needed to create the vacancies, whereas negative values imply that the reaction is exothermic. The calculated energies to produce a Na-vacancy, Mg-vacancy, and an H-vacancy at a bulk site are 3.91 eV, 7.00 eV, and 1.46 eV, respectively.

Therefore, it is energetically more favorable to create an H-vacancy. The value for the H-vacancy from pristine NaMgH_3 is similar to the value reported by Li *et al.* [86] calculated using the GGA-PBE theory level for Ti-doped Na_3AlH_6 ; where the authors reported a hydrogen removal energy of 1.46 eV. This hydrogen removal energy value can be explained by the similarity in the Mg-H bonding geometry for both hydrides. Also, it is important to note that this result for NaMgH_3 indicates that the Mg-H bond in NaMgH_3 is weaker than the Al-H bond found in NaAlH_4 (as inferred from the higher energy that is required to remove an H atom from NaAlH_4 , 4.0 eV [50]). Regarding the Na-vacancy, it is important to remark that with the cost of 3.91 eV this process appears unlikely, unless other initial effects, such as NaCl formation are considered (due to the use of TiCl_3 as a

dopant) [147]. Similarly, the cost to produce a Mg-vacancy is the highest with a cost of 7.00 eV.

Table 5-4 lists average bond distances between Na-H and Mg-H bonds in the NaMgH₃ supercell in the presence of vacancies located at a bulk site. In this scenario, for the pristine supercell model, the average nearest bond distances for Na-H and Mg-H are 2.50 Å and 2.00 Å, respectively. As a Na-vacancy is created the Na-H average distance is increased to 2.54 Å, and the Mg-H average bond distance is 1.99 Å. Therefore, there is very small structural change in the vicinity of the Na-vacancy. This small structural change is attributed to the strong mixed ionic-covalent bonds in the adjacent MgH₆ octahedral groups that keep the system undistorted. Therefore, these atomic bonds lock the structure at high symmetry, consequently, preventing distortion in the crystal. For the Mg and H-vacancy models, the average lengths of the Na-H and Mg-H bonds remain almost invariant.

Table 5-4: Calculated average bond lengths, point-defect energies, and hydrogen removal energies for pristine, Na-vacancy, Mg-vacancy, and Ti-doped Na₁₆Mg₁₆H₄₈ models are presented at the GGA-PBE theory level.

Average Bond Lengths (Å)	Point-Defect				
	None	Na	Mg	H	Ti-Na(Mg)
Na-H	2.50	2.54	2.50	2.50	2.54
Mg-H	2.00	2.01	2.01	2.00	2.02
Ti-H					1.98
Ti-Mg					2.90
Point-Defect Energy (ΔE_{PD}), eV		3.91	7.00	1.46	1.78/(3.86)
Hydrogen-Removal Energy (ΔE_{HR}), eV		-1.36		1.46	0.76

In order to mimic the substitution of a Na or Mg atom with Ti, 6.25% mol Ti substitution per 1 mole of NaMgH₃ (1 Ti atom per 16 formula units of NaMgH₃) is evaluated. The methodology for the Ti-doped model is similar to the one presented previously. Therefore, the energy cost of the Ti substitution is calculated according to Equation 5-4:

$$\Delta E_{PD} = [E((\text{Ti})\text{Na}_{16-x}\text{Mg}_{16-y}\text{H}_{48}) + xE(\text{Na}) + yE(\text{Mg}) - [E(\text{Na}_{16}\text{Mg}_{16}\text{H}_{48}) + E(\text{Ti})]]$$

Eq. 5-4

Here, $E((\text{Ti})\text{Na}_{16-x}\text{Mg}_{16-y}\text{H}_{48})$ corresponds to the total energy of the Ti doped at the Na site (x) or Mg site (y). Here, $E(\text{Na})$ corresponds to the energy of a single Na atom; $E(\text{Mg})$ corresponds to the energy of a single Mg atom; $E(\text{Na}_{16}\text{Mg}_{16}\text{H}_{48})$ corresponds to the energy of the pristine supercell and $E(\text{Ti})$ corresponds to the energy of a single Ti atom. The calculated substitution energy for the Ti-doped NaMgH₃ supercell model at the Mg site is 3.86 eV; which is too high, therefore this configuration is no longer considered. The calculated substitution energy for the Ti-doped NaMgH₃ supercell model at the Na site is 1.78 eV. This energy cost is less than that necessary to create a Na-vacancy case. The nearest neighbors' average bond lengths for Na-H and Mg-H in the Ti-doped case are 2.54 Å and 2.01 Å, respectively. Both of these bond lengths show an elongation when compared to the pristine and Na-vacancy model (see Table 5-4).

In order to clarify the effects of point-defects on the dehydrogenation properties of NaMgH₃, the hydrogen removal energies (ΔE_{HR}) are calculated. For these simulations the nearest neighbor H atoms are removed to obtain average hydrogen removal energies (ΔE_{HR}) for the following cases: pristine, Na-vacancy and Ti-doped models. It is important to note that the lowering of the hydrogen desorption temperature is attributed to a

reduction in the hydrogen removal energy [50]. For the Ti-doped model, the hydrogen removal energy (ΔE_{HR}) is calculated according to Equation 5-5:

$$\Delta E_{HR} = -[E(\text{TiNa}_{15}\text{Mg}_{16}\text{H}_{47}) - E(\text{TiNa}_{15}\text{Mg}_{16}\text{H}_{48}) - \frac{1}{2}E(\text{H}_2)] \quad \text{Eq. 5-5}$$

Here, $E(\text{TiNa}_{15}\text{Mg}_{16}\text{H}_{48})$ corresponds to the total energy of the Ti-doped system; $E(\text{TiNa}_{15}\text{Mg}_{16}\text{H}_{47})$ corresponds to the energy of the Ti-doped system with a hydrogen atom removed, and $E(\text{H}_2)$ is the total energy of a hydrogen molecule. The energy required to remove a hydrogen atom from the Ti-doped model is found to be $\Delta E_{HR} = 0.76$ eV. The hydrogen removal energy cost for the pristine structure is almost double the amount required by the Ti-doped model. Contrary to the Ti-doped and pristine case, the ΔE_{HR} value for the Na-vacancy is -1.36 eV. Note that it is expected that any hydrogen storage cycle will be endothermic during the hydrogen release, therefore the Na-vacancy model is not favorable for on-board hydrogen release [176].

5.2 Summary

In this chapter, the optimized structure of $\text{Na}_{3/4}\text{TM}_{1/4}\text{MgH}_3$ (TM = Ti, V, Cu, and Zn) are reported for the 25% mol TM doping concentration. Based on these lattice parameters' values of the TM-doped structures, it was shown that the replacement of $\frac{1}{4}$ of Na atoms by Ti, V, Cu, and Zn dopants do not lead to a significant change of the unit cell's volume. The maximum volume change is reported for the Ti-doped model with an approximate 6% decrease in the unit cell volume. For the TM-dopant models, TM dopants attract hydrogen atoms from adjacent Mg atoms and the corresponding Mg-H average bond length is increased. Also, the TM-dopants become coordinated to H atoms in typical octahedral configurations. The contraction of the unit cell volume is attributed to the TM-H bond length contraction.

Moreover, the Free energy values are reported for the 5 K to 800 K temperature range. It was reported that the Free energy values gradually decrease according to the following sequence: $\text{Cu} > \text{Ti} > \text{V} > \text{Zn} > \text{Pristine}$. It was observed that its Free energy values gradually decrease in the following order: $\text{Pristine} < \text{Zn} < \text{V} < \text{Ti} < \text{Cu}$; consequently, it is possible to destabilize the crystal with the addition of TM dopants. Moreover, enthalpy change at 298 K with inclusion of ZPE correction is reported for the first dehydrogenation step for the TM-doped crystalline NaMgH_3 . The largest decrease in the $\Delta H(298 \text{ K})$ value corresponds to the Zn-doped model (67.97 kJ/(mol H_2)). While the highest energy for the TM dopants is calculated for the Ti-doped model with a $\Delta H(298 \text{ K})$ value of 75.16 kJ/(mol H_2). The decomposition temperatures for the TM-doped models are in the range between 608 K and 514 K.

In addition, the calculated cohesive energy of the TM-doped NaMgH_3 supercell model is reported. Overall, it was shown that the Ti-doped NaMgH_3 and Zn-doped NaMgH_3 supercell models are more destabilized than the pristine case where no dopant is inserted. From the measurement of atomic bond distances, it is shown that the Mg-H bond is elongated for the TM-doped models. Similarly, all TM-doped models result in a TM-H bond contraction and attraction of Mg atoms as well. From the charge and population analysis, the overall chemical bonding of the TM doped models is determined.

Here, the Mg-H bond is shown to be ionic and the TM bonds are reported to be ionic-covalent. Therefore, the insertion of TM dopants result in an interference effect at the supercell model that results in a modification of the chemical bonding of the structure. From the analysis of structure and electronic properties, a possible TM-Mg_x-H_y complex structure is identified for most TM-doped models. From the DOS and PDOS

plots, it is shown that the position of (*d*) state peaks is important for the overall stability of the structure. Particularly, it is shown that the most prominent (*d*) peaks are located near the Fermi level.

Also, the effect of point-defects such as Na-vacancy, Mg-vacancy, and H-vacancy is determined in terms of total energy calculations. From these calculations, the point H-vacancy formation is preferred over the creation of the Na-vacancies and Mg-vacancies. In addition, the preferred position of the Ti-dopant within the bulk NaMgH₃ structure is calculated in terms of total energy. From the calculations, it is shown that Ti prefers to substitute an Na atom rather than a Mg atom. It is important to notice that it is more favorable to remove a H atom from the Ti-doped NaMgH₃ model than from the pristine NaMgH₃ model. Finally, it is shown that Ti and Zn dopants are the most effective metals from the 3*d* block to improve the thermodynamics of hydrogen release in this material.

CHAPTER 6

DFT STUDY OF MODIFIED (001) SURFACE

First-principles calculations based on DFT have been carried out to study the hydrogen desorption process from the (001) NaMgH₃ surface. The effects of strain, doping, and co-doping are considered. The effectiveness of these mechanisms is discussed. First, a theoretical investigation of selected TM (Ti, V, Cu, and Zn) substitution energies are carried out to determine if it is feasible to introduce these dopants at the surface and subsurface levels. It is interesting to note that experimental work at the surface level with NaMgH₃ at the moment is lacking. Moreover, DFT-MD simulations are carried out to analyze the structure of the doped material at high temperatures. Finally, activation energies for hydrogen desorption from the (001) surface are also calculated.

6.1 Results

6.1.1 Single Dopant

As mentioned previously, the stability of TM substitution (replacing a Na atom) at the outermost surface and subsurface layers of (001) NaMgH₃ surface models are studied. This is done to determine the preferred layer for dopant insertion at the (001) surface level. It is important to note that to the best of our knowledge, this is the first theoretical

study performed at the surface level for this material. In this dissertation, the substitution energy (E_{sub}) is defined as follows:

$$E_{sub} = [E(TM/Surface) + E(Na) - E(TM) - E(Surface)] \quad \text{Eq. 6-1}$$

Here, $E(TM/Surface)$ is the energy of the TM-doped (001) NaMgH₃ surface, $E(Na)$ is the energy of the substituted Na atom, $E(TM)$ is the energy of the TM in their free neutral state, and $E(Surface)$ is the energy of a pristine (001) NaMgH₃ surface. It is important to remark that a negative substitution energy value imply that TM is preferred in the structure compared to Na in the structure. The calculated substitution energy values for the TM-doped models, arranged by their position in the periodic table, at the outermost and subsurface layers of the (001) surface are shown in Figure 6-1.

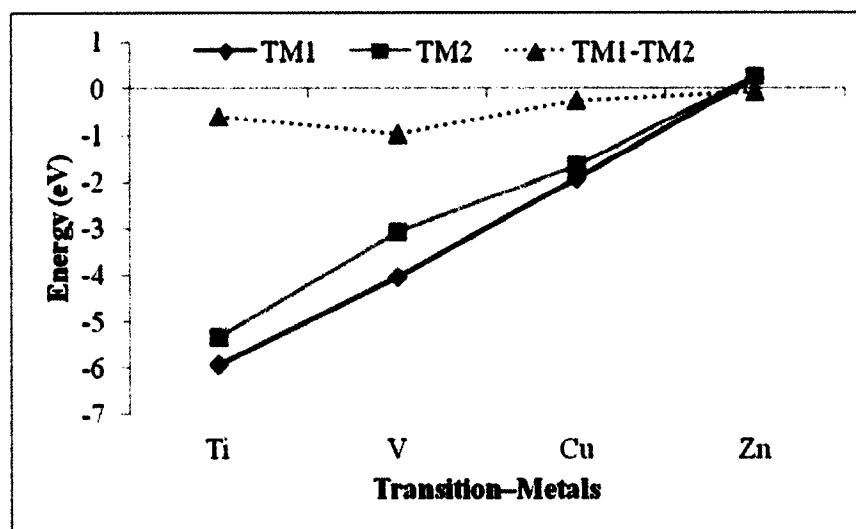


Figure 6-1: The substitutional energies of TM (at Na sites). Black line represents TM-doped at the first layer, gray solid line represents TM-doped in the second layer. The differences between the substitutional energies of TM doped in the first layer, and those doped in the second layer are shown with dotted gray lines.

Here, Ti has a substitution energy value of -5.93 eV at the outermost surface layer and -5.33 eV at the subsurface layer. For V, the substitution energy value is -4.03 eV at

the outermost surface layer and -3.07 eV at the subsurface layer. Similarly, for Cu, the substitution energy value is -1.91 eV at the outermost surface layer and -1.65 eV at the subsurface layer. For Zn, the substitution energy value is 0.23 eV at the outermost surface layer and 0.28 eV at the subsurface layer. Notice that for Ti, V, and Cu dopants the substitution energy values at the first and second layers are all negative. Therefore, substitution of these TM dopants are preferred compared to Na in the structure. On the other hand, the substitution energy value for the Zn-doped models is positive; consequently, Na is preferred over the insertion of a Zn dopant. Moreover, the substitution energy value is more negative for the early TM (Ti and V) and becomes less negative moving to the right of the periodic table and eventually becomes positive for Zn. Overall, by calculating the energy difference between TM at the outermost surface and subsurface (defined as $TM_1 - TM_2$), it is seen that substitution at the outermost surface is preferred (shows a negative energy except for the Zn-doped models). This preferred insertion site can be explained by the open nature of the outermost surface, herein, the focus is on the outermost surface models. This preference of the TM to substitute Na atoms at the outermost surface prompted an investigation of the local geometry of the TM-doped (001) NaMgH₃ surface models.

As shown in Figure 6-2, when TM substitute Na at the outermost surface layer, the early TM and Cu dopants are contracted toward the bulk, forming bonds with surrounding Mg and H atoms. The bond distance contraction towards the bulk and the charge analysis is listed in Table 6-1, where the distances of the nearest neighbors are tabulated (Mg-H, TM-H, and TM-Mg). On the other hand, the Zn-doped model does not show an increased association of the Zn, Mg, and H atoms.

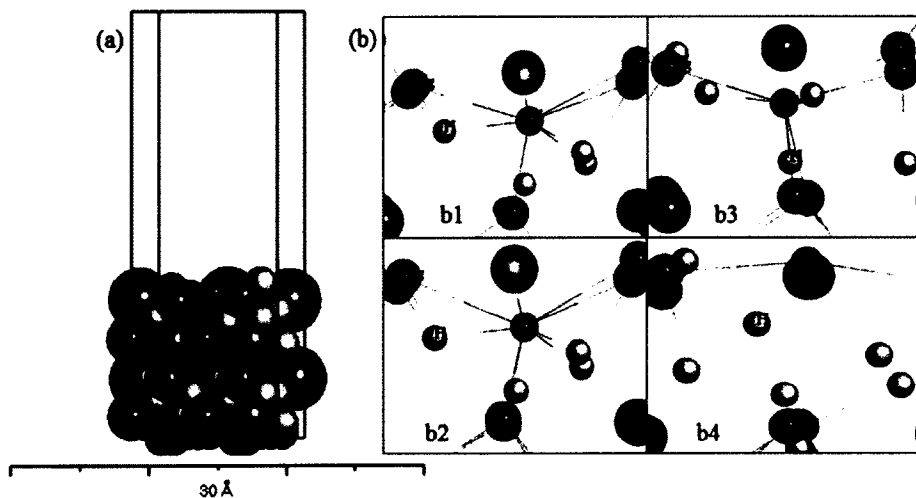


Figure 6-2: (a) Side view of optimized structure of TM-doped (001) NaMgH₃ surface (b) Detailed structure of Ti-Mg_x-H_y complex in the TM-doped (001) NaMgH₃ surface. Panels “b1”, “b2”, and “b3” show the geometry of the Ti-Mg₄-H₄, V-Mg₅-H₄, and Cu-Mg₄-H₃ complexes, respectively. Panel “b4” shows the nearest neighbors of Zn in the Zn-doped model.

In the relaxed Ti-doped structure, Ti has four Mg atoms at an average distance of 2.87 Å and four hydrogen atoms at an average distance of 1.87 Å. Likewise, V has five Mg atoms at an average distance of 2.82 Å and four hydrogen atoms at an average distance of 1.79 Å. Similarly, Cu has four Mg atoms at an average distance of 2.84 Å and three hydrogen atoms at an average distance of 1.70 Å. Notice that for all these dopants, the TM-H and TM-Mg average bond distance measurements are similar. In addition, early TM and Cu dopants show a higher coordination number with neighboring atoms when compared to the Na atom in the pristine model. On the other hand, in the Zn-doped model, the nearest Mg neighbors are located at an average distance of 2.80 Å.

Table 6-1: Average distances for the nearest neighbors for pristine and TM-doped (001) NaMgH₃ surface models. In addition, the average Hirshfeld charges are also listed in this table.

Bond Length (Å)	Pristine	Ti	V	Cu	Zn
Mg-H	1.98	2.00	1.99	1.98	1.98
TM-H		1.87	1.79	1.70	2.72
TM-Mg		2.87	2.82	2.84	2.80
Hirshfeld Analysis (e)					
Mg	0.27	0.25	0.25	0.26	0.25
Na	0.24	0.24	0.24	0.24	0.24
H	-0.17	-0.16	-0.16	-0.16	-0.16
Ti		-0.02			
V			-0.13		
Cu				0.04	
Zn					0.07

These increased association of dopants with Mg and H atoms forms an activated complex referred to as TM-Mg_x-H_y for the sake of simplicity (here, x and y denote the number of Mg and H atoms, respectively). Notice that TM-H bonds are also formed in a complex structure.

The local geometry of the TM-Mg_x-H_y structure is shown in Figure 6-2 for the different TM-doped models. It is interesting to note that our results are well in agreement with the results for MgH₂ reported by Pozzo *et al.* [179] which suggested that the ability of TM-doped surfaces to bind H atoms depend on the position of the TM in the periodic table.

Furthermore, Table 6-1 lists the charge transfers between TM, Mg, and H that take place at the TM-doped (001) NaMgH₃ surface models. Table 6-1 demonstrates that TM dopants disrupt the charge transfer between Mg and H atoms, consequently, debilitating the Mg-H bond. In general, one can speculate that in order to maintain charge neutrality within the TM-Mg_x-H_y complex, TM need to attract Mg and H atoms. On the other hand, the Zn dopant only has two nearest neighbors (all of them Mg atoms). This lack of nearest neighbors is what prompts the low stability of the Zn atom at the surface and subsurface layer of the NaMgH₃ (001) surface.

A deeper understanding of these chemical bonding can be achieved by analyzing the distribution of charges in real space (see Figure 6-3). Figure 6-3 shows the charge density difference of the TM-doped (001) NaMgH₃ surface models. Here, the intensity of the blue region is more noticeable for the late TM. On the other hand, Ti and V-doped surface models show penetration of red areas in their vicinity, indicating an ionic-covalent bonding in these regions. In all models, the charge transfer is accumulated on its nearest neighbor H atoms.

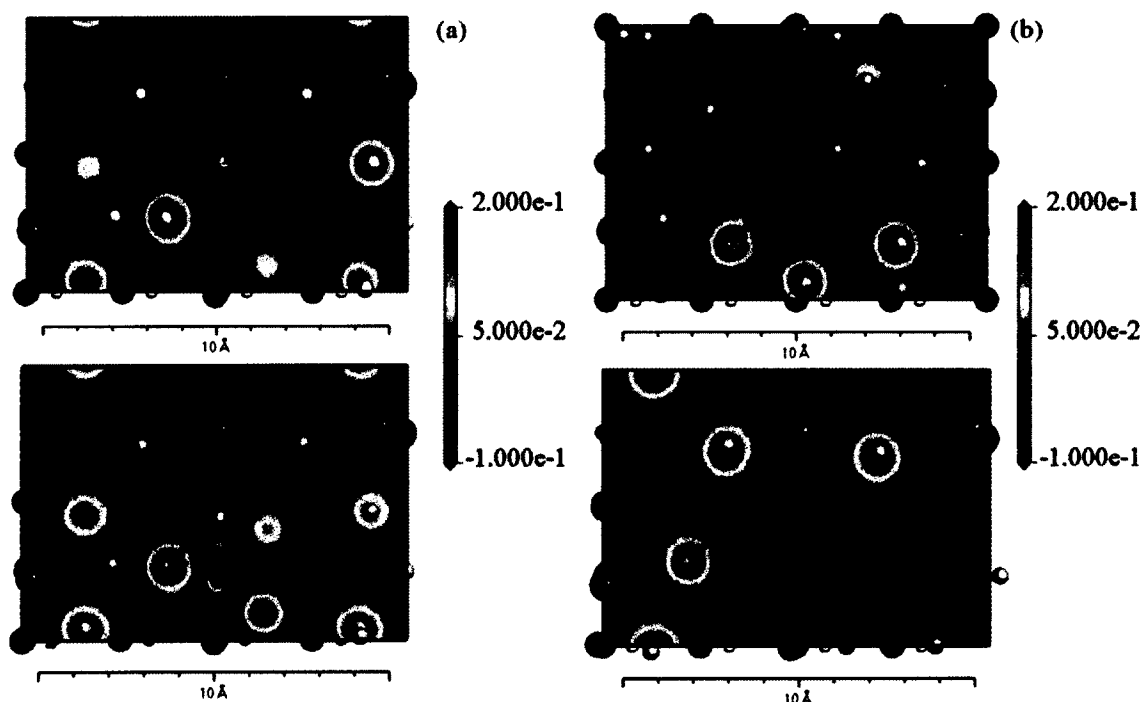


Figure 6-3: Electron density difference of (a) early TM-doped (001) NaMgH₃ surface, and (b) late TM-doped (001) NaMgH₃ surface. The spatial visualization of the electron density difference of (a) and (b) are taken along the (001) plane. Regions in red and blue represent electron-rich and electron-deficient regions, respectively. The range of the charge display is 0.10 $e/\text{\AA}$ to 0.20 $e/\text{\AA}$. A reversed rainbow color scheme with 16 bands was applied.

Therefore, the result of the charge difference analysis is complementary to the obtained Hirshfeld analysis. The effect of the TM on the chemical bonding is in two distinct ways: its bonding character with neighboring hydrogen atoms and its effect on the bonding between neighboring Mg and H atoms. In this respect, there are differences in how early and late TM dopants affect these bonding. In terms of Mg-H bonding, Ti, V, and Cu dopants produce similar Mg-H bond distances (elongated bond distances when compared to the pristine structure). Also, when considering the TM-H bond, all the TM dopants show a strong affinity towards H atoms, consequently debilitating the Mg-H

bond interaction. The weakening of the Mg-H bond can be attributed to the interference effect of TM dopants competing for the charge transfer among Mg and H atoms.

6.1.2 DFT coupled Molecular Dynamics (DFT-MD)

Hydrogen storage systems are subjected to the operation temperatures of the fuel cells. Here, DFT-MD simulations are employed to examine the role of temperature in overcoming energy barriers and hence in structural relaxation in the Ti-doped and Zn-doped models. These simulations can also aid in discovering dehydrogenation pathways. Indeed, through DFT-MD simulations possible, routes for hydrogen release and the dynamic origin of Ti dopants were revealed for the vacancy-mediated dehydrogenation of sodium alanate [180]. For the DFT-MD simulations, wave function and charge density extrapolations are introduced to use a 330 eV energy cutoff in conjunction with a 0.5 femtosecond time step [181, 182]. Temperatures are maintained using Nosé-Hoover chains [158], with configurations belonging to the canonical (N, V, T) ensemble and micro-canonical (N, V, E) ensemble. Nuclear deuterium is used instead of hydrogen in order to set the time step at 0.5 fs for a total simulation time of 3.5 ps at 300 K and 400 K. At each temperature, DFT-MD simulations are performed at the NVE ensemble for 0.5 ps to equilibrate the structure and then a production run in the NVT ensemble for 3 ps. It is important to note that the DFT-MD simulations are stopped until the systems reach an energy convergence of 5 meV/atom.

The Ti and Zn models are chosen for the following reasons. Ti destabilizes the NaMgH₃ hydride and forms an unusual Ti-Mg₄-H₄ complex at the (001) NaMgH₃ surface models. Similarly, the Zn dopant also destabilizes the NaMgH₃ hydride, however, Zn does not form a Zn-Mg_x-H_y complex at the (001) NaMgH₃ surface. On the contrary, Na is

preferred over the substitution of Zn at the outermost layer. For the Ti-doped model, at 0 K, the Ti-Mg bond has an average distance of 2.87 Å and for the Ti-H bond the average distance is 1.87 Å. When the temperature is increased to 300 K (after 4 ps total simulation time), a Ti-Mg₄-H₄ complex is observed where the Ti-Mg bond is elongated (relative to the 0 K structure) to an average distance of 2.96 Å and the Ti-H bond is also elongated to an average distance of 1.96 Å. At the 400 K temperature (after 8 ps total simulation time), Ti attracts additional Mg and H atoms and a Ti-Mg₅-H₇ complex is observed, the Ti-Mg average bond distance is 2.96 Å and the Ti-H average bond is 1.83 Å. Two snapshots of the Ti-Mg_x-H_y complex as it evolves from 300 K (4 ps) to 400 K (8 ps) are shown in Figure 6-4. These two temperatures are selected to study the dynamics of the systems at room temperature and at the PEM fuel cell with higher operating temperature. The snapshots clearly indicate that Ti attracts H atoms from the surrounding Mg atoms. This complex can aid in the hydrogen desorption process by facilitating the Mg-H bond scission.

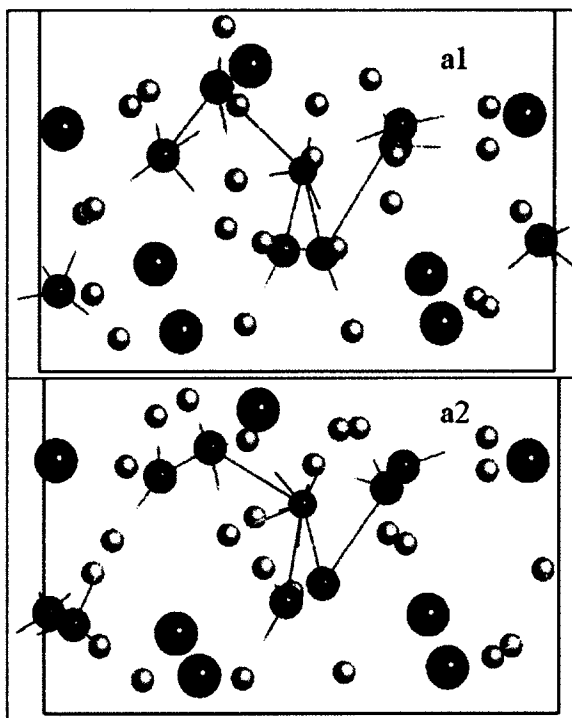


Figure 6-4: Snapshots of the Ti-doped (001) NaMgH₃ surface. Panels “a1” (300 K) and “a2” (400 K) show the structural evolution of the Ti-Mg_x-H_y complex as temperature is increased and time evolves. Snapshots “a1” and “a2” are taken at the end of the 4 ps and 8 ps simulations, respectively. Here, the red sphere represents the Ti dopant. Visualization is performed with a 0.2 CPK value.

Meanwhile, for the Zn-doped model, at 0 K Zn has two Mg atoms as nearest neighbors at an average distance of 2.80 Å. At the 300 K temperature (after 4 ps), the Zn has four Mg atoms as the nearest neighbors at an average distance of 3.27 Å. At the 300 K temperature, the Zn atom bonds with four H atoms at an average distance of 1.72 Å. For the 400 K temperature (after 8 ps), the local geometry of the Zn-doped model remains almost unchanged compared to the geometry of the structure at 300 K, having four Mg atoms as nearest neighbors at a distance of 3.22 Å and bonding with four H atoms at an average distance of 1.72 Å. Two snapshots of the Zn-doped model as it evolves from 300 K (4 ps) to 400 K (8 ps) are shown in Figure 6-5.

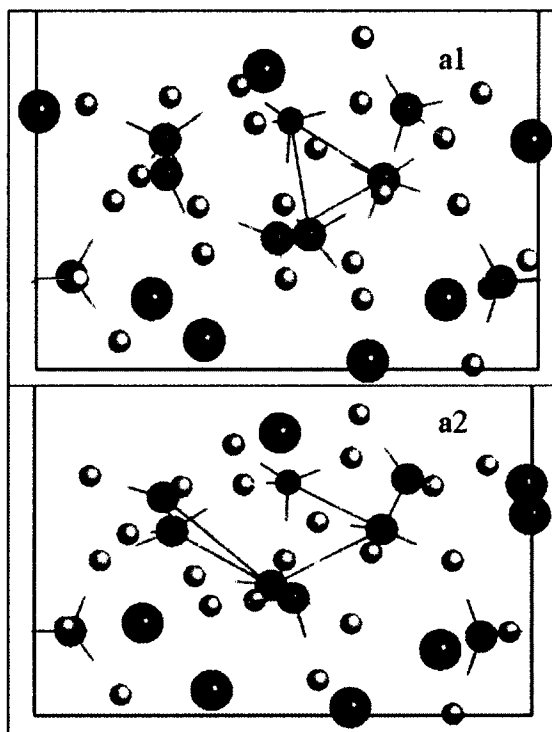


Figure 6-5: Snapshots of Zn-doped (001) NaMgH₃ surface. Panels “a1” (300 K) and “a2” (400 K) show the structural evolution of the surface as temperature is increased, and time evolves. Snapshots “a1” and “a2” are taken at the end of the 4 ps and 8 ps simulations, respectively. Here, the red sphere represents the Zn dopant. Visualization is performed with a 0.2 CPK value.

Notice that the structure for the Zn-doped model differs from the Ti-doped model because it does not form a TM-Mg_x-H_y complex. Therefore, on the basis of these results, it is interesting to investigate the effect of Zn and Ti as co-dopants at the surface of the (001) NaMgH₃ model. The reason for this is as follows. Ti forms a Ti-Mg_x-H_y that assists in weakening the Mg-H bond (speculated due to the elongated Mg-H bond lengths); however, the short Ti-H bonds may cause some difficulties in the dehydrogenation process. On the other hand, Zn mainly has H atoms as the nearest neighbors; therefore, Zn as a co-dopant may debilitate the Ti-H bond (by attracting some of the H atoms bonded to Ti), resulting in an even lower dehydrogenation barrier.

6.1.3 Hydrogen Removal Energy

The hydrogen removal energy of the pristine and TM-doped (001) NaMgH₃ surface is calculated using first-principles calculations. The hydrogen removal energy is defined as follows:

$$\Delta E_{HR} = [E((\text{TM}/\text{Na})\text{Na}_{15}\text{Mg}_{16}\text{H}_{48}) - E((\text{TM}/\text{Na})\text{Na}_{15}\text{Mg}_{16}\text{H}_{48-z}) - \frac{1}{2}E(\text{H}_2)]$$

Eq. 6-2

Here, $E((\text{TM}/\text{Na})\text{Na}_{15}\text{Mg}_{16}\text{H}_{48})$ is the energy of the pristine or TM-doped (001) NaMgH₃ surface, $E((\text{TM}/\text{Na})\text{Na}_{15}\text{Mg}_{16}\text{H}_{48-z})$ is the energy of the pristine or TM-doped (001) NaMgH₃ surface with one or two H removed, and $E(\text{H}_2)$ is the energy of a hydrogen molecule placed in a 1 nm cube. Here, z indicates the number of H removed from the model.

Due to the possible formation of the TM-Mg_x-H_y complex, the hydrogen desorption energies are calculated as a function of H positions. Different arrangements of H desorption at the (001) outermost surface and subsurface layers are investigated. These arrangements for the pristine (001) NaMgH₃ surface model are as follows (see Figure 6-6):

1. One H₂ molecule missing from different Mg atoms at the outermost surface (H-Mg Mg-H) (H1-H2).
2. One H₂ molecule missing from the same Mg atoms at the outermost surface (H-Mg-H) (H1-H3).
3. Single H atom missing from the outermost surface and originally attached to a Mg atom (Single H/outer) (H4).

4. Single H atom missing from the subsurface site and originally attached to a Mg atom (Single H/subsurface) (H5).

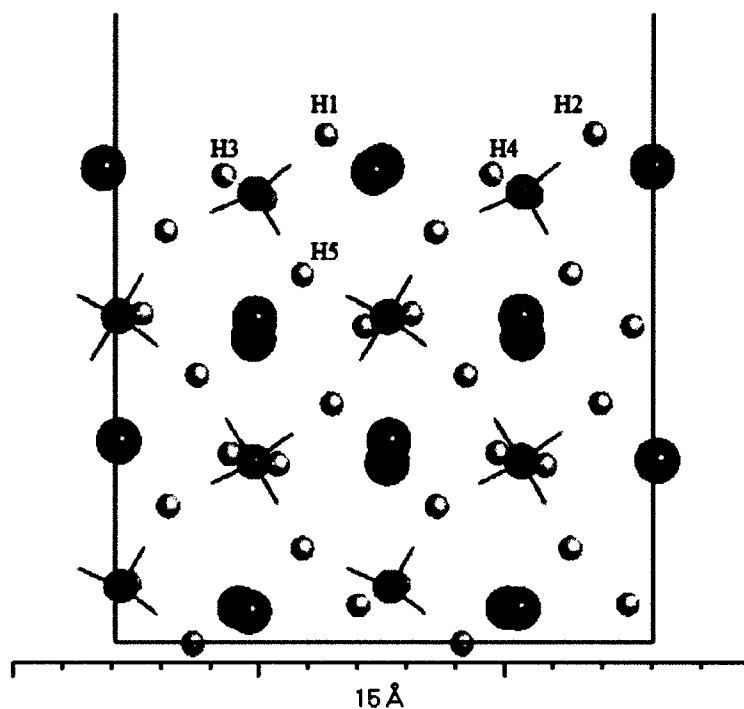


Figure 6-6: GGA-PBE relaxed structure of the pristine (001) NaMgH₃ surface, showing the positions of the H atoms being removed. Here, removed H atoms as H₂ molecules are labeled as H1, H2, and H3. Similarly, removed H atoms as single H atoms are labeled as H4 and H5. Visualization is performed with a 0.2 CPK value.

The arrangements for the TM-doped (001) NaMgH₃ surface model is as follows (see Figure 6-7):

1. One H₂ molecule missing from different Mg atoms at the outermost surface (H-Mg Mg-H) (H1-H3).
2. One H₂ molecule missing from same Mg atoms at the outermost surface (H-Mg-H) (H1-H4).

3. One H_2 molecule missing from TM and Mg atoms. Here, the H atom attached to TM does not form bonds with other atoms (H-TM-H-Mg) (H4-H5).
4. One H_2 molecule missing from TM and Mg atoms. Here the H atom attached to TM forms bonds with other Mg atoms (Mg-H-TM-H-Mg) (H4-H6).

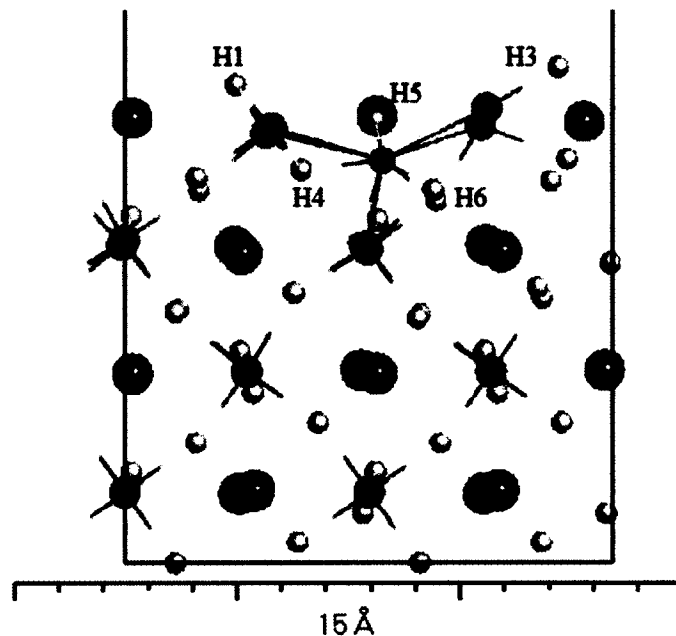


Figure 6-7: GGA-PBE relaxed structure of the TM-doped (001) $NaMgH_3$ surface, showing the positions of the H atoms being removed as H_2 molecules. Visualization is performed with a 0.2 CPK value.

Hydrogen desorption energies due to the removal of hydrogen molecules from different positions are shown in Figure 6-8. In the pristine model, the energy cost to remove H_2 molecules from the same Mg atom at the outermost surface is 1.01 eV. Meanwhile, the energy cost to remove one H_2 from different Mg atoms at the outermost surface is 0.75 eV. Moreover, the energy cost to remove single H atoms from the outermost surface and subsurface sites is 2.33 eV and 2.49 eV, respectively. These results

show that hydrogen desorption does not occur in atomic form. Therefore, the associative H_2 desorption has to be considered for this material.

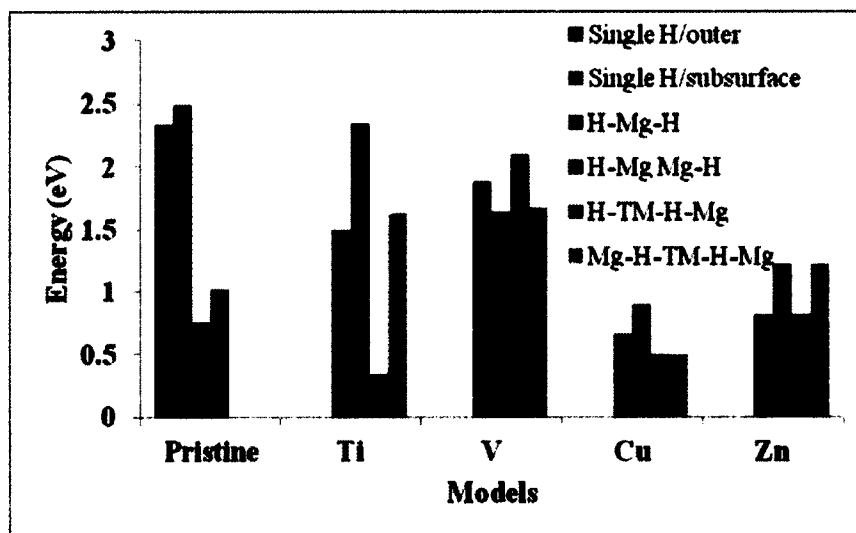


Figure 6-8: Hydrogen removal energy values for pristine and TM-doped (001) $NaMgH_3$ surface models.

Moreover, to remove one H_2 from the same MgH_6 octahedral unit is more costly than the desorption from different MgH_6 octahedral units. When the (001) $NaMgH_3$ surface is doped with TM, the H_2 desorption energy increases significantly for the early TM when the TM are not involved in the desorption process, that is, when one H_2 is removed from adjacent MgH_6 octahedral units to the TM.

On the other hand, in this same scenario, the H_2 desorption energy decreases significantly for the late TM. For the early TM, the increase in H_2 desorption energy is from 1.50 to 2.34 eV. Meanwhile, for the late TM, the H_2 desorption energy decrease is from 1.23 to 0.67 eV. Therefore, based on the results presented so far, it seems logical to test the scenario where the TM are involved in the dehydrogenation process in two distinct ways. First, H_2 is removed from the TM, where one of the H atoms is only

bonded to the TM dopant. Second, H₂ is removed from the TM and an adjacent MgH₆ octahedral unit (here, the H atoms are shared among the TM and Mg atoms).

From these scenarios, the H₂ removal energy decreases when H₂ is desorbed from the TM that does not share any H atoms. This is true for all TM except for V (resulting in an energy cost of 2.10 eV). However, for the rest of the TM, the energy cost is reduced in the range of 0.34 to 0.82 eV. Particularly, for the Ti-doped model this energy cost is favorable (0.34 eV) when compared to the pristine model (0.75 eV). However, the combinative desorption of hydrogen atoms (from Ti and adjacent MgH₆ octahedral units) has an energy cost of 1.63 eV. From these results, it can be concluded that hydrogen removal from the Ti-doped model is energetically favorable over the desorption from the pristine (001) NaMgH₃ surface.

In order to understand the origin of the reduced desorption energy of hydrogen from the Ti-doped (001) NaMgH₃ surface, the optimized Ti-doped model with a removed H₂ molecule, is analyzed. Figure 6-9 shows that the removal of a H₂ molecule (with one H atom bounded just with Ti) causes adjacent hydrogen atoms of the neighboring Mg-H bonds to associate with the Ti atom. In this relaxed structure, Ti assists in forming a Ti-Mg₅-H₅ (similar to the complex found with the DFT-MD simulations). Here, the average Ti-H bond distance is 1.90 Å and the average Ti-Mg bond is 3.09 Å. Notice that these average bond distances are elongated when compared to the Ti-doped structure with no H₂ removed (average Ti-H bond distance is 1.87 and the average Ti-Mg bond distance is 2.87 Å).

Furthermore, this movement of hydrogen atoms during H₂ removal indicates that the barrier for hydrogen diffusion in this Ti-Mg_x-H_y complex structure is low. These

hydrogen movement to the vicinity of the Ti atom aids in sustaining the hydrogen desorption process until the hydrogen atoms in the $\text{Ti-Mg}_x\text{-H}_y$ complex structure becomes depleted. Therefore, with the introduction of a Ti dopant, a new pathway for hydrogen desorption is opened. The results from these studies will help to establish the dehydrogenation mechanism for the (001) NaMgH_3 surface.

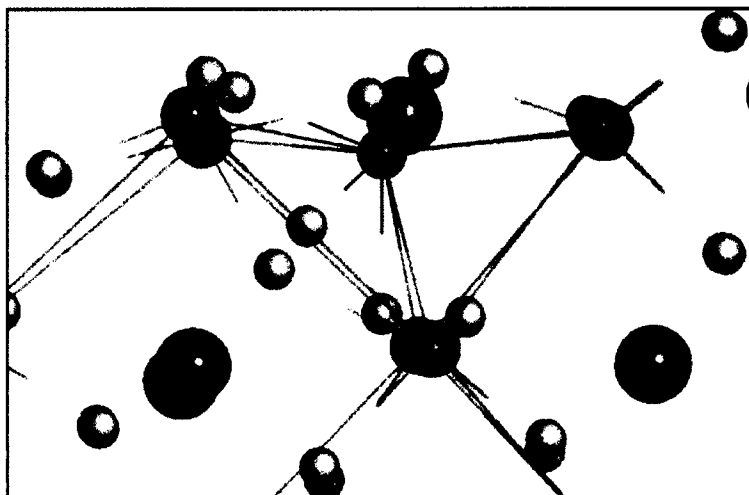


Figure 6-9: The Local geometry of the Ti-doped (001) NaMgH_3 surface slab. Here, the color convention is same as previous figures. Red spheres denote the Ti substituted at the surface Na site. Visualization is performed with a 0.2 CPK value.

6.1.4 Strain Effect on (001) NaMgH_3 Surface

The surface studies presented until now, employed the technique of TM doping to improve hydrogen storage properties. In this section, the biaxial homogeneous mechanical strain on the (001) NaMgH_3 surface is also applied. Once the optimized lattice constants are determined, the lattice constants are modified from -5% (compression) to 5% (elongation) along the x and y directions of the (001) NaMgH_3 surface in order to represent uniform biaxial strain effect on the surface. Figure 6-10

gives the total energy curve of the (001) NaMgH₃ surface under applied strain. The stability of the surface can be associated with its total energy, where a lower total energy indicates a more stable surface and higher energy indicates a destabilized surface. As shown in Figure 6-10, the (001) NaMgH₃ surface is stabilized when it experiences a biaxial compressive or tensile strain (except for the 5% elongation). It is important to notice that the total energy in the strain due to the elongation is more pronounced than that of the compressive strain because of the higher total energy shown for the strain elongation models. When the 5% elongation is applied in the x and y directions of the surface, the lattice constants become $a = 11.497 \text{ \AA}$ and $b = 8.074 \text{ \AA}$. Herein, for all strained models, the 5% elongation of the lattice parameters in the x and y directions is applied.

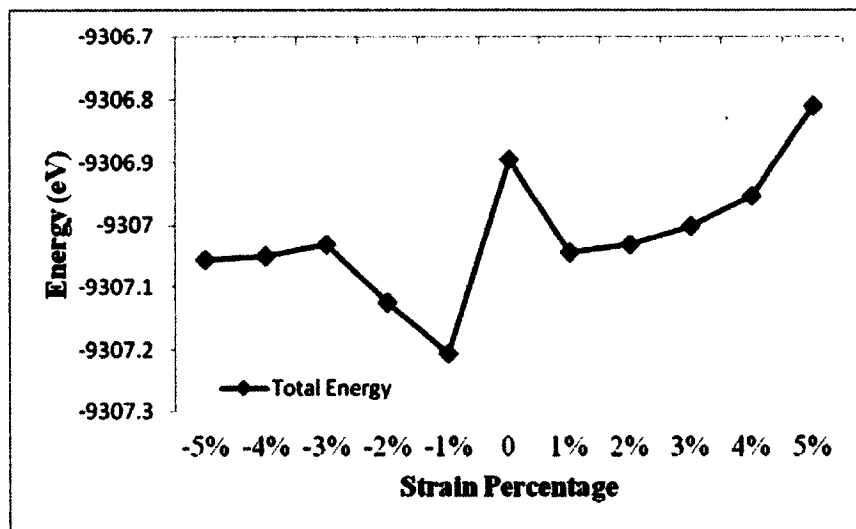


Figure 6-10: Total energy curves for the (001) NaMgH₃ surface when it is subjected to different strain percentages.

From Figure 6-10, one can speculate that it is easier to remove hydrogen from strained (elongated) surfaces.

In order to quantify the effect of the strain, the hydrogen removal energy of the (001) NaMgH₃ surface with 5% mechanical elongation is calculated in the following manner:

$$\Delta E_{HR} = -[E(\text{Na}_{16}\text{Mg}_{16}\text{H}_{46}) - E(\text{Na}_{16}\text{Mg}_{16}\text{H}_{48}) - E(\text{H}_2)] \quad \text{Eq. 6-2}$$

Here, $E(\text{Na}_{16}\text{Mg}_{16}\text{H}_{46})$ is the energy of the strained surface with one H₂ molecule removed, $E(\text{Na}_{16}\text{Mg}_{16}\text{H}_{48})$ is the energy of the pristine strained surface and $E(\text{H}_2)$ is the energy of the H₂ molecule. Similarly, for the Ti-doped surface with 5% elongation of the lattice parameters, the following equation is used:

$$\Delta E_{HR} = -[E(\text{TiNa}_{15}\text{Mg}_{16}\text{H}_{46}) - E(\text{TiNa}_{15}\text{Mg}_{16}\text{H}_{48}) - E(\text{H}_2)] \quad \text{Eq. 6-3}$$

Here, $E(\text{TiNa}_{15}\text{Mg}_{16}\text{H}_{46})$ is the energy of the Ti-doped strained surface with an H₂ molecule removed, $E(\text{TiNa}_{15}\text{Mg}_{16}\text{H}_{48})$ is the energy of the Ti-doped strained surface, and $E(\text{H}_2)$ is the energy of the H₂ molecule. It is important to note that negative and positive values represent exothermic and endothermic reactions, respectively. Here, the hydrogen molecules removed belong to the outermost surface and subsurface sites.

Table 6-2 shows the reduction in the hydrogen removal cost caused by the Ti-doped-strained (001) NaMgH₃ surface. It is clear from Table 6-2 that the mechanical elongation of the lattice parameters has an effect on the hydrogen removal cost. For the pristine-strained model, the energies are -0.83 eV at the outermost surface site and -0.31 eV at the subsurface site. Therefore, the hydrogen removal reaction becomes exothermic without the need to introduce any TM as doping agents.

Table 6-2: Hydrogen Removal Energy (ΔE_{HR}) for the strained and Ti-doped (001) surface models.

Hydrogen Removal Energy (ΔE_{HR}) (eV)		
Models	Outermost Surface	Subsurface
Pristine-strained	-0.83	-0.58
Ti-doped-strained	-0.12	-0.31

However, even when the (001) surface is doped with TM, the hydrogen removal reaction is exothermic when one H_2 is removed from the subsurface and outermost surface sites. Here, the Ti-doped model shows energy values of -0.31 eV and -0.12 eV at the subsurface and outermost surface sites, respectively. These results are in sharp contrast with calculated hydrogen removal energies without strain, where the hydrogen removal energy cost is positive, hence an endothermic process. As mentioned previously, it is expected that any hydrogen storage cycle will be endothermic during the hydrogen release. Due to this limitation, calculations from these models are not pursued.

Figure 6-11 shows the optimized structure for the Ti-doped-strained (001) $NaMgH_3$ surface model after H_2 is removed. In this model, Ti forms bonds with six nearby H atoms at an average distance of 1.87 Å and five Mg atoms at an average distance of 3.09 Å. When compared to the strain free Ti-doped surface slab, this model has two additional Mg and H atoms. However, the Ti-doped-strained (001) $NaMgH_3$ surface shows an elongated Ti-Mg bond distance (3.09 Å) when compared to the strain free Ti-doped surface slab (2.84 Å). Therefore, it is speculated that at the Ti-doped-strained (001) $NaMgH_3$ surface slab, the formation of a Ti- H_y complex structure is preferred over the formation of a Ti- Mg_x-H_y complex structure.

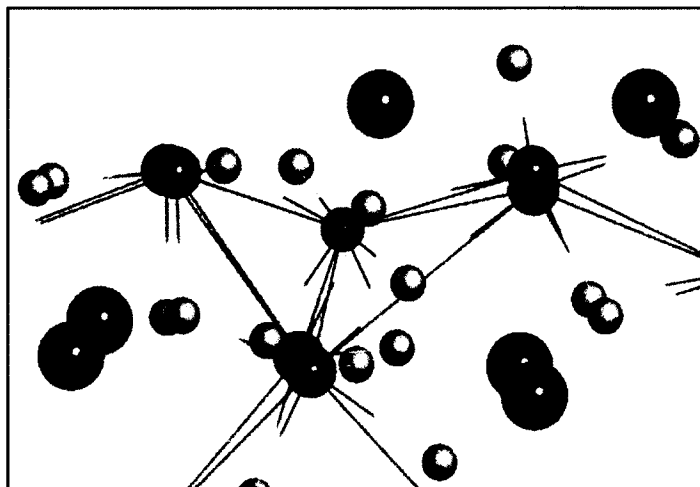


Figure 6-11: Side view of the optimized structure of the Ti-doped-strained (001) NaMgH₃ surface. Visualization is performed with a 0.2 CPK value.

6.1.5 The Stability of Co-dopants at the (001) NaMgH₃ Surface

Even though TM-doped metals inserted at the first layer are energetically preferable, it is interesting to analyze the combination of early TM and late TM. For this work, Ti and Zn dopants as co-dopants are studied (see Figure 6-12), the two TM that show the highest and lowest stability at the (001) NaMgH₃ surface model, respectively. In addition, Zn dopant is selected because according to the results presented in the previous section, it is the only dopant among the ones studied in this chapter that shows a difference energy of less than 0.20 eV in its two configurations (substituting Na at first and second layers). This difference in energy could be beneficial to the interaction of these dopants with other dopants in the first layer or second layer and could assist to further stabilize other dopants [77].

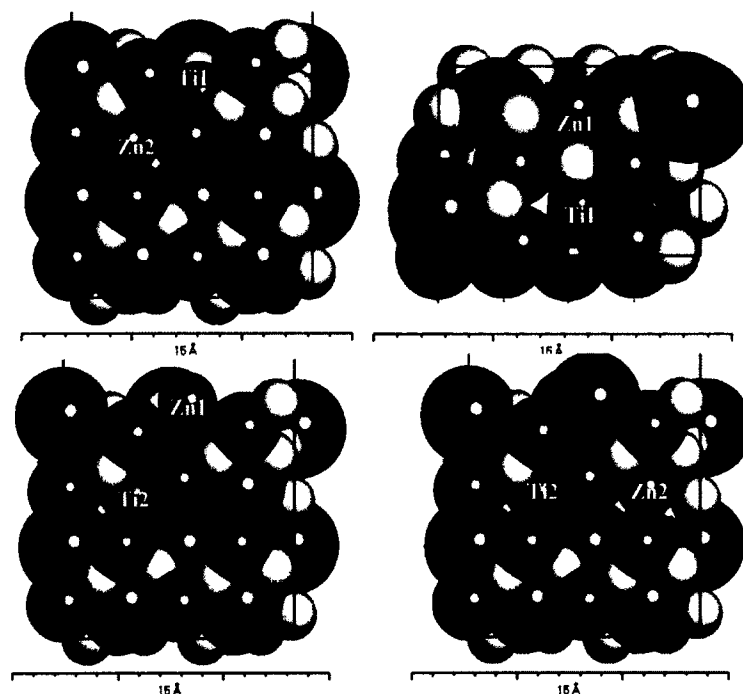


Figure 6-12: Side views of possible configurations of co-doped (001) NaMgH₃ surfaces. Here, the top-left, top-right, bottom-left, and bottom-right panels show the Ti₁Zn₂, Ti₁Zn₁, Ti₂Zn₁, and Ti₂Zn₂ configurations, respectively.

The stability of the configurations is analyzed by the substitution energy defined as follows:

$$E_{sub} = E(\text{TiZn}/(001)\text{Surface}) + 2E(\text{Na}) - E(\text{Ti}) - E(\text{Zn}) - E[(001)\text{Surface}] \quad \text{Eq. 6-4}$$

Here, $E(\text{TiZn}/(001)\text{Surface})$ is the energy of the Ti and Zn-doped (001) NaMgH₃ surface, $E(\text{Na})$, $E(\text{Ti})$, and $E(\text{Zn})$ are the energies of Na, Ti and Zn atoms, respectively.

For all the considered configurations, the substitutional energies of Ti and Zn co-doped at the (001) surface are shown in Figure 6-13.

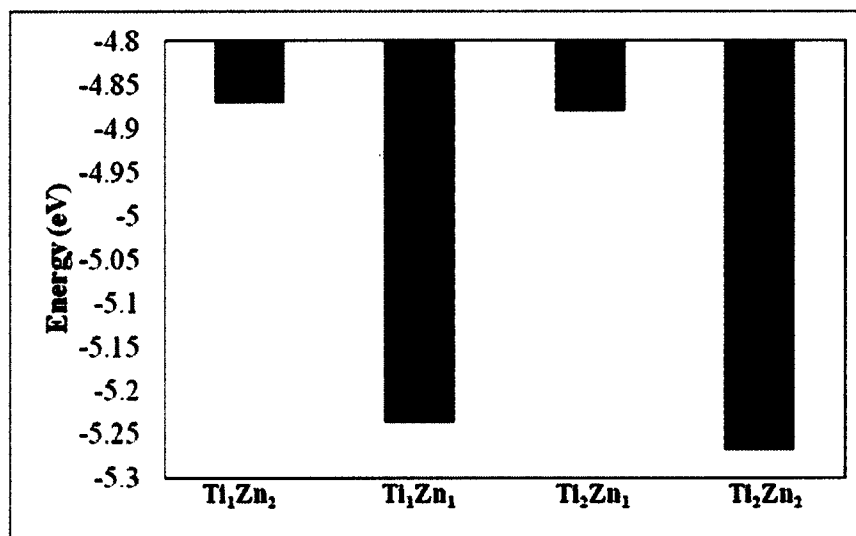


Figure 6-13: The substitutional energies of TM co-doped at the NaMgH₃ (001) surface.

From Figure 6-13, it is clear that the preferred configuration is when Ti and Zn are co-doped at the same surface layer (Ti_1Zn_1 or Ti_2Zn_2 configurations), whether it is at the outermost or subsurface layer. For these calculations, Ti_1Zn_1 and Ti_2Zn_2 configurations have similar E_{sub} values of -5.27 eV and -5.24 eV, respectively. Notice that when compared to the case where a single Ti replaces a Na atom at the outermost surface, the E_{sub} value for the Ti_2Zn_2 configuration is slightly higher by 0.02 eV. The co-dopant configurations are more stable than single V, Cu, and Zn doping. The Ti_1Zn_1 configuration is used to study the dehydrogenation kinetics of the co-doped (001) NaMgH₃ surface.

6.1.6 Dehydrogenation Kinetics at the (001) NaMgH₃ Surface

In this section, the kinetic barrier for hydrogen desorption from the (001) surface is studied using DFT calculations, LST/QST and NEB methods. The results show that the diffusion of H atoms plays an important role in the dehydrogenation mechanism at this

surface. Moreover, the mechanism for hydrogen desorption is discussed for the Ti and Ti/Zn co-doped (001) NaMgH₃ surface as well.

Two main H₂ desorption configurations are studied.

1. The configuration where H atoms are bounded directly to Mg/TM atoms and recombine to desorb as a H₂ molecule.
2. Second, the configuration where H atoms are bounded to two different MgH₆ octahedral units and recombine to desorb as a H₂ molecule.

As mentioned previously, NEB calculations using 10 images are performed in order to investigate the activation process for direct associative H₂ desorption from the (001) NaMgH₃ surface. To validate the results, a calculation for H₂ desorption from the pristine (001) surface is carried out first. For the direct recombination of a H₂ molecule (placed at 5 Å normal to the surface) when H atoms are bounded to an MgH₆ octahedral unit at the subsurface site, we find that the kinetic barrier is 1.16 eV and we also find that the diffusion of the H₂ molecule to the surface has a kinetic barrier of 0.65 eV. Notice that this diffusion process is lower than the activation energy value of 0.98 eV for hydrogen hopping reported by Shane *et al.* [36]. It is important to note that the initial NEB is a linear interpolation between a relaxed configuration representing the (001) surface and a final relaxed configuration in which the H₂ molecule is desorbed above the surface at a 5 Å distance.

Therefore, the linear interpolation is an approximation to a direct desorption process. However, when the minimum energy path is obtained, no such process is found (see Figure 6-14). Instead, the minimum energy path is broken into several processes. First, one of the H atoms move to an adjacent MgH₆ octahedral unit while the other H

atom remains bonded to the original MgH_6 octahedral unit. Then, both H atoms move, where one H atom moves to bond with the outermost MgH_6 octahedral unit and the other H atom forms a H_2 molecule with an adjacent H atom. Next, the H atom breaks apart from this H_2 molecule and moves to an adjacent MgH_6 octahedral unit at the surface site. One H atom diffuses across the surface and bonds to an adjacent MgH_6 octahedral unit (with an activation barrier of 1.16 eV). Finally, when both H atoms are bonded to the adjacent MgH_6 octahedral units (see Figure 6-14, panel 6), the H atoms desorb as a H_2 molecule.

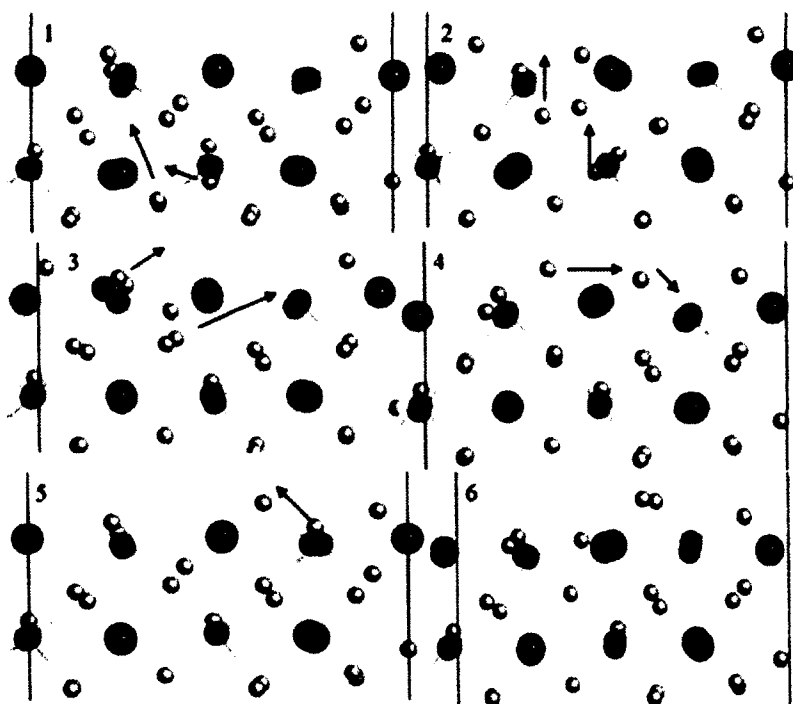


Figure 6-14: The minimum energy path for H_2 desorption from a subsurface site at the (001) NaMgH_3 surface. The yellow spheres represent the H atoms. Visualization is performed with a 0.1 CPK value.

Next, the configuration in which the H_2 desorbs from the recombination of H atoms bounded to two different MgH_6 octahedral units at the surface is tested. Figure 6-

15 shows that the H_2 desorption process from two different MgH_6 octahedral units located at the surface is less convoluted than the previous case where a H_2 molecule is removed from a MgH_6 octahedral unit at the subsurface site.. Here, the atoms are already bonded at adjacent MgH_6 octahedral units and we find that the kinetic barrier for this process is 1.72 eV. These simulations show that the preferred dehydrogenation pathway at the (001) $NaMgH_3$ surface is the recombination of H atoms (bonded to the same MgH_6 octahedral unit) into H_2 molecules. However, the kinetic barrier remains high. Next, this pathway will be tested for the Ti-doped model.

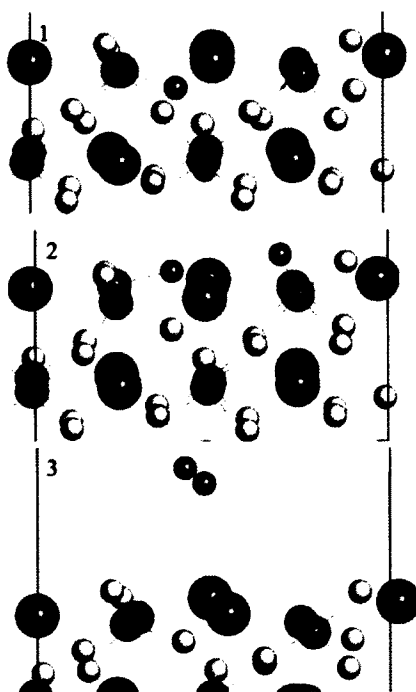


Figure 6-15: The minimum energy path for H_2 desorption from H recombination at the (001) $NaMgH_3$ surface. The yellow spheres represent the H atoms at the subsurface and the orange spheres represent H atoms at the surface. Visualization is performed with a 0.2 CPK value.

Figure 6-16 shows the reaction pathway for H_2 desorption from two H atoms bonded to the Ti dopant. We find that the H_2 desorption from this Ti-doped surface

follows a sequential mechanism with an energy cost of 4.25 eV (see Figure 6-16 and panel 4). Notice that for this dehydrogenation process, the Ti dopant attracts an additional H atom before desorbing the H₂ molecule. Therefore, before H₂ desorbs the Ti dopant has five adjacent H atoms at an average bond distance of 1.64 Å. Notice that this bond distance is decreased in comparison with other Ti-doped models studied in this work. The sequential H₂ desorption mechanism coupled with the average bond distance explains the high kinetic barrier to desorb the H₂ molecule from the Ti-doped model.

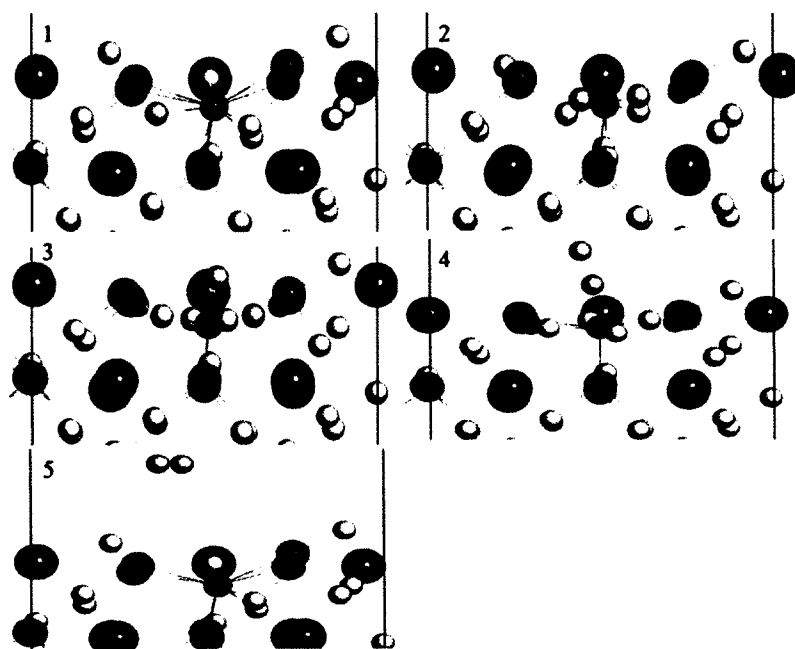


Figure 6-16: The minimum energy path for H₂ desorption from H recombination at the Ti-doped (001) NaMgH₃ surface. The yellow spheres represent the H atoms that recombine into a H₂ molecule. The red sphere represents the Ti atom. Visualization is performed with a 0.2 CPK value.

Moreover, in Figure 6-16, it is shown that a Ti-Mg_x-H_y is formed at the (001) surface and this complex can serve as a precursor structure that aids in hydrogen desorption. However, it is shown that in order to desorb a H₂ molecule from the Ti-doped

model, the Ti atom attracts an additional H atom before releasing H atoms sequentially in order to form a H₂ molecule.

However, due to this excess of H atoms around the vicinity of the Ti dopant, it is difficult to overcome the energy barrier to desorb a H₂ molecule. Therefore, even though the Ti dopant weakens the Mg-H bond, to remove a H₂ molecule from a Ti dopant carries a high energy cost. Therefore, a mechanism that may aid in the desorption of a H₂ molecule is to co-dope the hydride with a Zn dopant (Figure 6-17). We find that the calculated kinetic barrier of H₂ desorption when the (001) surface is co-doped with Ti and Zn is 0.42 eV.

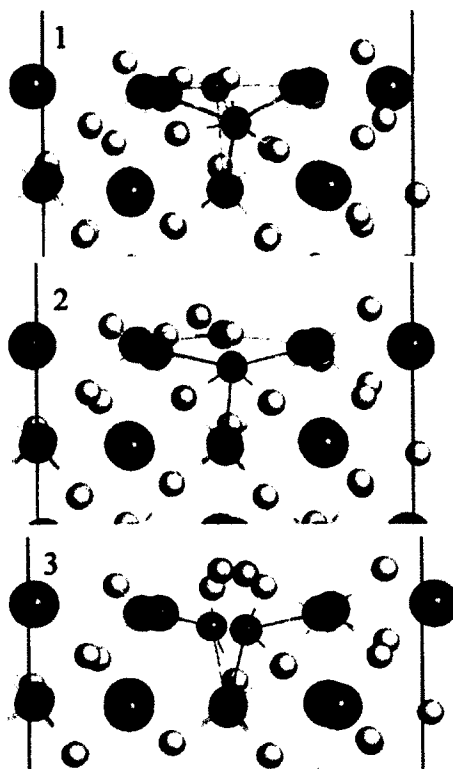


Figure 6-17: The minimum energy path for H₂ desorption from H recombination at the Ti/Zn-doped (001) surface of NaMgH₃. The yellow spheres represent the H atoms that recombine into an H₂ molecule. The red sphere represents the Ti atom and the dark blue sphere represents the Zn atom. Visualization is performed with a 0.2 CPK value.

The Ti atom is surrounded by five H atoms at an average bond distance of 1.88 Å. Therefore, the introduction of the Zn dopant allows the Ti-H bond to elongate (when compared to the Ti-doped model) and reduce the kinetic barrier of H₂ desorption. Notice that the dehydrogenation cost for this model (0.42 eV or 40 kJ/(mol H₂)) meets the technical target established by the US-DOE for hydrogen desorption. These results show that the combined use of a Ti dopant and a Zn dopant is the best configuration for reducing the energy cost to release hydrogen from the (001) NaMgH₃ surface.

6.2 Summary

The stability of TM substitution of Na atoms at the outermost surface and subsurface layers of (001) NaMgH₃ surface models are reported by means of substitution energy. From the substitution energies, it is reported that all TM dopants prefer to substitute a Na atom at the outermost (001) NaMgH₃ surface. From the calculations, it is shown that Ti has the most negative substitution energy with a value of -5.93 eV. That is, Ti is the TM dopant that would be the most stable at the outermost (001) surface upon substitution of a Na atom. On the other hand, from the substitution energies, it is shown that a Zn dopant prefers to segregate at both Na sites.

In terms of geometry, it is found that early TM and Cu dopants are contracted towards the bulk upon insertion on the (001) surface. This contraction leads to a possible formation of a TM-Mg_x-H_y complex structure. The results suggest that the ability of TM dopants to bind with H atoms depend on the position of the TM in the periodic table. From the charge analysis, it is seen that TM dopants disrupt the charge transfer between Mg and H atoms, consequently debilitating the Mg-H bond and showing a strong affinity

towards H atoms. Therefore, the TM-Mg_x-H_y complex structure and interference effect of TM dopants are still present at the (001) NaMgH₃ surface.

From the *ab-initio* molecular dynamic simulations, it is shown that Ti attracts additional Mg and H atoms and a Ti-Mg_x-H_y complex is observed, the Ti-Mg average bond distance is 2.96 Å and the Ti-H average bond is 1.83 Å. At 400 K, after 8 ps, the local geometry of the Zn-doped model has four Mg atoms as the nearest neighbors at a distance of 3.22 Å and bonds with four H atoms at an average distance of 1.72 Å.

However, the Zn-doped model differs from the Ti-doped model because it does not form a TM-Mg_x-H_y complex. Due to the possible formation of the TM-Mg_x-H_y complex, the hydrogen desorption energies are calculated as a function of H positions. In the pristine model, the energy cost to remove H₂ molecules from the same MgH₆ octahedral unit at the outermost surface is 1.01 eV. Meanwhile, the energy cost to remove H₂ from different MgH₆ octahedral units at the outermost surface is 0.75 eV. Similarly, the energy cost to remove single H atoms from the outermost surface and subsurface sites is 2.33 eV and 2.49 eV, respectively. From these results, it is concluded that hydrogen desorption does not occur in atomic form at the pristine (001) NaMgH₃ surface. An important point is that to remove H₂ from the same MgH₆ octahedral unit is more costly than to remove H₂ from different MgH₆ octahedral units. For the scenario where hydrogen is removed from TM-doped models, it is easier to remove hydrogen molecules that result from the following combination: H atom bonded solely with TM and H atom shared among TM and MgH₆ octahedral units. Particularly, for the Ti-doped model this energy cost is 0.34 eV.

Meanwhile, the combinative desorption of hydrogen atoms (from Ti and adjacent Mg) has an energy cost of 1.63 eV. Therefore, with the introduction of a Ti dopant, a new pathway for hydrogen desorption is opened. Moreover, the total energy curve of the (001) NaMgH₃ surface under applied strain percentages is presented. We find that the 5% mechanical strain elongation results in the higher total energy of the model; therefore, this elongation is applied at the (001) NaMgH₃ surface. It is important to remark that a mechanical elongation is preferred over a mechanical compression in order to destabilize the system. The hydrogen removal energy of the (001) NaMgH₃ surface under applied strain is calculated for the pristine model and the Ti-doped model. It is shown that at the outermost surface and subsurface sites, the hydrogen removal process proceeds in an exothermic reaction, therefore not meeting the requirements set by the US-DOE.

The combination of Ti and Zn dopants as co-dopants at the (001) NaMgH₃ surface models are calculated in terms of substitution energy calculations. We find that the preferred site for the simultaneous insertion of Ti and Zn dopants is at the same surface later, particularly, the outermost Na site with an E_{sub} value of -5.27 eV. The kinetic barrier for hydrogen desorption from the (001) surface is studied using DFT calculations, LST/QST, and NEB methods. For the pristine model, the direct recombination of a H₂ molecule has a kinetic barrier of 1.16 eV. We find that the diffusion of the H₂ molecule to the surface has a kinetic barrier of 0.65 eV. The recombination for the H₂ molecule is not a direct desorption process; on the contrary, the minimum energy path is broken into several processes. From the MEP calculations, it is shown that lateral diffusion across the surface has the highest activation energy for the desorption process (1.16 eV). Furthermore, we find that when a H₂ molecule bonded at

an adjacent MgH_6 octahedral unit is desorbed, the kinetic barrier for this process is 1.72 eV. Consequently, from the dehydrogenation kinetics, we find that the preferred site for H_2 desorption is when H_2 is recombined from desorption from the same MgH_6 octahedral unit. The energy cost for the removal of a H_2 molecule from the Ti-doped surface is 4.25 eV. The high energy cost is attributed to the sequential mechanism that takes place when H_2 is desorbed from a Ti-doped structure. We find that the calculated kinetic barrier of H_2 desorption when the (001) surface is co-doped with Ti and Zn is 0.42 eV. These results show that the combined use of a Ti dopant and a Zn dopant is the best configuration for reducing the energy cost to release hydrogen from the (001) NaMgH_3 surface.

CHAPTER 7

CONCLUSIONS AND FUTURE WORK

7.1 Conclusions

Hydrogen is an attractive energy carrier for hydrogen-based fuel cells for on-board vehicle applications. However, one of the biggest impediments to implement this technology is the lack of a suitable hydrogen storage material. The hydrogen storage system should be cost-effective, safe, and it should provide with appropriate charge/discharge rates of hydrogen within the storage tank.

Currently, solid materials with high hydrogen content show promising characteristics for safe means of hydrogen storage. However, most solid-state materials release hydrogen at high temperatures. Several mechanisms are currently being studied to mitigate these problems. In this regard, materials containing magnesium such as sodium magnesium hydride (NaMgH_3) have attracted attention as a hydrogen storage material due to its high volumetric capacity, however, this material also release hydrogen at high temperatures (670 K). In the recent past, it has been demonstrated that introducing impurities to the material modifies properties in such a way that it can greatly improve the thermodynamics and kinetics of hydrogen desorption.

The main goal of this dissertation is to address the fundamental aspects of hydrogen storage by utilizing computer simulations, particularly, density functional

theory (DFT) and DFT-based calculations. The main findings of this dissertation in terms of the objectives are summarized:

1. Structural, electronic, vibrational, vibrational-based, and mechanical properties of the pristine NaMgH₃ crystal structure.

- For the NaMgH₃ crystal structure, the calculated average distance for Na-Mg, Mg-H and Na-H bonds are 3.33 Å, 1.98 Å, and 2.28 Å, respectively. The average Na-Mg-Na angle is calculated to be approximately 68°. The tilting angle of the Mg-H₆ octahedral group in the optimized unit cell is 13.68°. The values for the calculated lattice parameters are well in agreement with experimental findings.
- The DOS and PDOS plots show that the crystal structure of NaMgH₃ has a band gap value of approximately 3.50 eV. From the DOS and PDOS plots, a stronger interaction due to (*s-p*) hybridization is visible at the higher region of the valence band; which extends from -3.00 eV up to the Fermi level. From the combined analysis of the electronic properties, an ionic-covalent chemical bonding is found for this crystal. From the Hirshfeld analysis, the charges for Mg atoms in NaMgH₃ crystal can be attributed to the electron transfer towards H atoms, resulting in a negative value of the H atomic charge. This redistribution of the electron cloud is attributed to the ionic-covalent nature of the chemical bonding between the Mg and H atoms.
- From the vibrational analysis, three frequency bands are identified. The lowest frequency band is dominated by the motion of the heavy atoms, the middle-frequency band is attributed to the MgH₆ octahedral group tilt and the higher frequency bands are dominated by H vibrations due to the symmetric and

asymmetric Mg-H stretch. Relevant thermodynamic properties such as H , G , S , and C_m are reported as functions of temperature. Here, the calculated free energy values are reported from the 5 K to 800 K temperature range. In this study, free energy values decrease as the temperature of the crystal is increased from 5 K to 800 K. On the other hand, H and S values increase continuously as the temperature is increased. For the heat capacity, the calculated value ($490 \text{ J mol}^{-1} \text{ K}^{-1}$) follows the Dulong–Petit rule for solids.

- From the thermodynamics of the first step decomposition, the enthalpy change and standard enthalpy formation are calculated. The values for the enthalpy change, and standard formation are calculated as $81.43 \text{ kJ}/(\text{mol H}_2)$ and 139.8 kJ/mol , respectively. From these values, the calculated decomposition temperature is calculated to be 664 K. These results are important since they contribute to the wealth of experimental and computational results available for this material. From the study of mechanical properties, it was determined that the NaMgH_3 crystal exhibits large elastic anisotropy along the (001) plane due to the intercalated bonding of Na, Mg, and H atoms along this plane.
2. The effect on thermodynamics, electronic structure, and energetics of TM acting as doping agents at two different doping concentrations.
- The replacement of $\frac{1}{4}$ of Na atoms by Ti, V, Cu, and Zn dopants do not lead to a significant change of the unit cell volume. The maximum volume change is reported for the Ti-doped model with an approximate 6 % decrease in the unit cell volume. For the TM-dopant models, TM dopants attract hydrogen atoms from adjacent Mg atoms and the corresponding Mg-H average bond length is increased.

Also, the TM-dopants become coordinated to H atoms in typical octahedral configuration. The contraction of the unit cell volume is attributed to the TM-H bond length contraction.

- The Free energies are reported for the 5 K to 800 K temperature range. It was reported that Free energy values gradually decrease according to the following sequence: Cu > Ti > V > Zn > Pristine. The calculated Free energy values show that the thermal stabilities of the doped crystal gradually decrease in the following order: Pristine < Zn < V < Ti < Cu; consequently, it is possible to destabilize the crystal with addition of TM dopants. Moreover, enthalpy change at 298 K with inclusion of ZPE correction was reported for the first dehydrogenation step for TM-doped crystalline NaMgH₃. The largest decrease in $\Delta H(298\text{ K})$ value corresponds to the Zn-doped model (67.97 kJ/(mol H₂)). The highest energy for the TM dopants is calculated for the Ti-doped model with an $\Delta H(298\text{ K})$ value of 75.16 kJ/(mol H₂). The decomposition temperatures for the TM-doped models are in the range of 608 K–514 K.
- The calculated cohesive energy of the TM-doped NaMgH₃ supercell model is reported. Overall, it was shown that the Ti and Zn-doped NaMgH₃ supercell models are more destabilized than the pristine case where no dopant is inserted. From the measurement of atomic bond distances, it is shown that the Mg-H bond is elongated for the TM-doped models. Similarly, Ti, V, and Cu-doped models result in a TM-H bond contraction and attraction of Mg atoms, as well. From the charge and population analysis, the overall chemical bonding of the TM-doped models is determined.

- The Mg-H bond was shown to be ionic and the Ti-H and V-H bonds are reported to be ionic-covalent. The insertion of TM dopants results in an interference effect at the supercell model that results in weakening of the Mg-H bond. From the analysis of structure and electronic properties, a possible TM-Mg_x-H_y complex structure is identified for most TM-doped models. From the DOS and PDOS plots, it is shown that the position of (*d*) state peaks is important for the overall stability of the structure. Particularly, it is shown that the most prominent (*d*) peaks are located near the Fermi level.
 - The effect of point-defects such as Na-vacancy, Mg-vacancy and H-vacancy is determined in terms of total energy calculations. From these calculations, the H-vacancy formation is preferred over the creation of Na-vacancies and Mg-vacancies. In addition, the preferred position of the Ti-dopant within the bulk NaMgH₃ structure is calculated in terms of total energy. From these calculations, it is shown that Ti prefers to substitute a Na atom rather than an Mg atom. It is important to notice that it is more favorable to remove an H atom from the vicinity of a Ti atom than from the vicinity of a Na atom, Na-vacancy or H-vacancy.
3. Effect of selected TM-doping on (001) NaMgH₃ surface. Particular focus is directed towards the preferred TM and co-dopant combination to be inserted into the surface, dynamic evolution at high temperatures of TM-doped (001) NaMgH₃ surface, effect of applied strain on hydrogen storage properties, and hydrogen desorption from the pristine and modified-(001) NaMgH₃ surface.

- The stability of TM substitution of Na atoms at the outermost surface and subsurface layers of (001) NaMgH₃ surface models are reported by means of substitution energy. From the substitution energies, it is reported that all TM dopants prefer to substitute a Na atom at the outermost surface of (001) NaMgH₃. From these calculations, it is shown that Ti has the most negative substitution energy with a value of -5.93 eV. That is, Ti is the TM dopant that would be the most stable at the outermost (001) surface upon substitution of a Na atom. On the other hand, from the substitution energies, it is shown that the Na atom is preferred over the substitution of a Zn dopant.
- Early TM and Cu dopants are contracted towards the bulk upon insertion on the (001) surface. This contraction leads to a possible formation of a TM-Mg_x-H_y complex structure. The results suggest that the ability of TM dopants to bind with H atoms depend on the position of the TM in the periodic table. From the charge analysis, it is seen that TM dopants disrupt the charge transfer between Mg and H atoms; consequently, debilitating the Mg-H bond and showing a strong affinity towards H atoms. Therefore, the TM-Mg_x-H_y complex structure and interference effect of TM dopants are still present at the (001) NaMgH₃ surface.
- From the *ab-initio* molecular dynamic simulations, it is shown that Ti attracts additional Mg and H atoms and a TM-Mg₅-H₇ complex is observed, the Ti-Mg average bond distance is 2.96 Å and the Ti-H average bond is 1.83 Å. Therefore, for the Ti-doped model the TM-Mg_x-H_y complex structure is formed at high temperatures.

- Due to the possible formation of the TM-Mg_x-H_y complex structure, the hydrogen desorption energies are calculated as a function of H positions. In the pristine model, the energy cost to remove H₂ molecules from the same Mg atom at the outermost surface is 1.01 eV. Meanwhile, the energy cost to remove H₂ from different Mg atoms at the outermost surface is 0.75 eV. Similarly, the energy cost to remove single H atoms from the outermost surface and subsurface sites is 2.33 eV and 2.49 eV, respectively. From these results, it is concluded that hydrogen desorption does not occur in atomic form at the pristine (001) NaMgH₃ surface. An important point is that to remove H₂ from the same Mg atom is more costly than the desorption from different Mg atoms. For the scenario where hydrogen is removed from TM dopants, it is easier to remove hydrogen molecules that result from the following combination: H atom bonded solely with TM and H atom shared among TM and Mg atoms. Particularly, for the Ti-doped model this energy cost is favorable (0.34 eV) when compared to the pristine model (0.75 eV). Meanwhile, the combinative desorption of hydrogen atoms (from Ti and adjacent Mg) has an energy cost of 1.63 eV. Therefore, with the introduction of a Ti dopant, a new pathway for hydrogen desorption is opened.
- The total energy curve of the (001) NaMgH₃ surface under applied strain is presented. We find that the 5% elongation of lattice parameters along the x and y directions results in a model with higher total energy; therefore, 5% is the preferred strain elongation percentage to be applied at the (001) NaMgH₃ surface along the x and y directions. It is important to remark that a mechanical elongation is preferred over a mechanical compression in order to destabilize the

system. The hydrogen removal energy from the (001) NaMgH₃ surface due to a 5% mechanical elongation along x and y directions is calculated for the pristine and the Ti-doped model.

- The combination of Ti and Zn dopants as co-dopants at the (001) NaMgH₃ surface models is calculated in terms of substitution energy calculations. We find that the preferred site for the simultaneous insertion of Ti and Zn dopants is the outermost Na site with an E_{sub} value of -5.27 eV. The kinetic barrier for hydrogen desorption from the (001) surface is studied using DFT calculations, LST/QST, and NEB methods. We find that for the pristine model, the direct recombination of a H₂ molecule has a kinetic barrier of 1.16 eV. The diffusion of the H₂ molecule to the surface has a kinetic barrier of 0.65 eV. The recombination for the H₂ molecule is not a direct desorption process; on the contrary, the minimum energy path is broken into several processes. From the MEP calculations, it is shown that lateral diffusion across the surface has the highest activation energy for the desorption process (1.16 eV). When a H₂ molecule is removed from adjacent MgH₆ octahedral units, the kinetic barrier for this process is 1.72 eV. Consequently, from the dehydrogenation kinetics, the preferred site for H₂ desorption is when H₂ is recombined after desorbing from the same MgH₆ octahedral unit. The energy cost for the removal of a H₂ molecule from the Ti-doped structure is 4.25 eV. The high energy cost is attributed to the sequential mechanism that takes place when H₂ is desorbed from a Ti-doped site. We find that the calculated kinetic barrier of H₂ desorption when the (001) surface is co-doped with Ti and Zn is 0.42 eV. These results show that other mechanisms

besides single TM-doping are favorable for improving the hydrogen storage properties of NaMgH₃. These results show that the combined use of a Ti dopant and a Zn dopant is the best configuration for reducing the energy cost to release hydrogen from the (001) NaMgH₃ surface.

7.2 Future Work

Computational materials science is playing a fundamental role in the development of energy storage and energy conversion systems. Particularly, the development of efficient computational infrastructure, codes, and faster high performance computers is increasing the connection between simulations and experimental studies. For the energy storage application, *ab-initio* studies have the potential to aid in the design of systems that utilize hydrogen as an energy carrier. For the wide-scale use of hydrogen as an energy carrier, the main challenge is to design a solid-state material capable of storing hydrogen in a safe and optimal manner.

In this dissertation, periodic boundary conditions (PBC) are used to study the hydrogen storage properties (thermodynamics and kinetics) of NaMgH₃ in periodic infinite models. To improve the hydrogen storage properties, it would be interesting to perform a DFT study of NaMgH₃ nano-clusters. For instance, Majzoub *et al.* [177] reported a direct decomposition for NaAlH₄ due to the cluster size effect. The stability order of TM-doped NaMgH₃ can be reversed due to the shape and composition of the nano-clusters.

Furthermore, future developments in catalysts are key for engineering a hydrogen storage material. The search for a proper catalyst or destabilization scheme in order to facilitate hydrogen release from hydrogen storage materials is still open. Although we

find that the use of dopants such as Ti and Zn results in a destabilized structure and a low kinetic barrier for hydrogen release in NaMgH_3 , it is essential to develop low-cost catalysts of high performance [178].

In this respect, carbon nano-materials (single-walled carbon nanotubes and graphene sheets) are promising materials that could be used as catalysts to facilitate hydrogen release for on-board hydrogen storage applications [179]. Indeed, carbon-based nanostructures for hydrogen storage show promising results [176, 177].

Similar computational techniques used in this dissertation can be applied in order to study the fundamental mechanism behind the catalytic effects of carbon nano-materials. To achieve this, nano-cluster models constructed from the NaMgH_3 unit cell can be used to study the interaction of these clusters with various sites of the exposed graphene or single-walled carbon nanotube models. The use of defective and doped-carbon nano-materials is also an interesting approach that merits investigation.

Moreover, in order to take in consideration more realistic PEM fuel cell operating conditions, possible combination of *ab-initio* studies with other methods such as Kinetic Monte Carlo (KMC) simulations can be conducted in the future. This multi-scale modelling will allow the use of a larger scale study that can be used to know more about the hydrogen storage desorption kinetics. Particularly it would be interesting to study the hydrogen diffusion in a co-doped model similar to the one presented in this dissertation.

REFERENCES

- [1] Weidenkaff A. *Majumdar puts materials in the context of energy systems*. MRS Bulletin. 2013;38:448-9.
- [2] Bose S, Kuila T, Nguyen TXH, Kim NH, Lau K-t, Lee JH. *Polymer membranes for high temperature proton exchange membrane fuel cell: Recent advances and challenges*. Progress in Polymer Science. 2011;36:813-43.
- [3] Züttel A. *Materials for hydrogen storage*. Materials Today. 2003;6:24-33.
- [4] Rönnebro ECE, Majzoub EH. *Recent advances in metal hydrides for clean energy applications*. MRS Bulletin. 2013;38:452-8.
- [5] Andrews J, Shabani B. *Re-envisioning the role of hydrogen in a sustainable energy economy*. International Journal of Hydrogen Energy. 2012;37:1184-203.
- [6] Klebanoff L. *Hydrogen Storage Technology: Materials and Applications*. Boca Raton: Taylor & Francis; 2012.
- [7] Zuttel A. *Hydrogen storage methods*. Naturwissenschaften. 2004;91:157-72.
- [8] Varin RA, Czujko T, Wronski ZS. *Nanomaterials for Solid State Hydrogen Storage*. New York: Springer; 2009.
- [9] Fichtner M. *Nanotechnological Aspects in Materials for Hydrogen Storage*. Advanced Engineering Materials. 2005;7:443-55.
- [10] Durbin DJ, Malardier-Jugroot C. *Review of hydrogen storage techniques for on board vehicle applications*. International Journal of Hydrogen Energy. 2013;38:14595-617.
- [11] Frenette G, Forthoffer D. *Economic & commercial viability of hydrogen fuel cell vehicles from an automotive manufacturer perspective*. International Journal of Hydrogen Energy. 2009;34:3578-88.
- [12] Veziroglu A, Macario R. *Fuel cell vehicles: State of the art with economic and environmental concerns*. International Journal of Hydrogen Energy. 2011;36:25-43.

- [13] Satyapal S, Petrovic J, Read C, Thomas G, Ordaz G. *The U.S. Department of Energy's National Hydrogen Storage Project: Progress towards meeting hydrogen-powered vehicle requirements*. Catalysis Today. 2007;120:246-56.
- [14] Klebanoff LE, Keller JO. *5 Years of hydrogen storage research in the U.S. DOE Metal Hydride Center of Excellence (MHCoe)*. International Journal of Hydrogen Energy. 2013;38:4533-76.
- [15] Michel KJ, Ozoliņš V. *Recent advances in the theory of hydrogen storage in complex metal hydrides*. MRS Bulletin. 2013;38:462-72.
- [16] Ritter JA, Ebner AD, Wang J, Zidan R. *Implementing a hydrogen economy*. Materials Today. 2003;6:18-23.
- [17] U.S. Department of Energy H, Fuel Cell and Infrastructure Technologies: FY, 2003 Annual Progress Report.
- [18] Grochala W, Edwards PP. *Thermal decomposition of the non-interstitial hydrides for the storage and production of hydrogen*. Chemical Reviews. 2004;104:1283-315.
- [19] Shanahan KL, Klein JE. *Reversible and irreversible passivation of a La-Ni-Al alloy*. Journal of Alloys and Compounds. 2010;496:91.
- [20] Yang J, Sudik A, Wolverton C, Siegel DJ. *High capacity hydrogen storage materials: attributes for automotive applications and techniques for materials discovery*. Chemical Society Reviews. 2010;39:656-75.
- [21] Dathara GKP, Mainardi DS. *Structure and dynamics of Ti-Al-H compounds in Ti-doped NaAlH₄*. Molecular Simulation. 2008;34:201-10.
- [22] Bogdanović B, Schwickardi M. *Ti-doped alkali metal aluminium hydrides as potential novel reversible hydrogen storage materials*. Journal of Alloys and Compounds. 1997;253-254:1-9.
- [23] Bogdanović B, Felderhoff M, Kaskel S, Pommerin A, Schlichte K, Schüth F. *Improved hydrogen storage properties of Ti-doped sodium alanate using titanium nanoparticles as doping agents*. Advanced Materials. 2003;15:1012-5.
- [24] Chaudhuri S, Muckerman JT. *First-Principles Study of Ti-Catalyzed Hydrogen Chemisorption on an Al Surface: A Critical First Step for Reversible Hydrogen Storage in NaAlH₄*. The Journal of Physical Chemistry B. 2005;109:6952-7.
- [25] Pottmaier D, Pinatel ER, Vitillo JG, Garroni S, Orlova M, Baró MD, et al. *Structure and thermodynamic properties of the NaMgH₃ perovskite: A comprehensive study*. Chemistry of Materials. 2011;23:2317-26.

- [26] Yvon K, Bertheville B. *Magnesium based ternary metal hydrides containing alkali and alkaline-earth elements*. Journal of Alloys and Compounds. 2006;425:101-8.
- [27] Khowash PK, Rao BK, McMullen T, Jena P. *Electronic structure of light metal hydrides*. Physical Review B - Condensed Matter and Materials Physics. 1997;55:1454-8.
- [28] Vajeeston P, Ravindran P, Fjellvåg H. *A new series of high hydrogen content hydrogen-storage materials: A theoretical prediction*. Journal of Alloys and Compounds. 2007;446-447:44-7.
- [29] Wu H, Zhou W, Udovic TJ, Rush JJ, Yildirim T. *Crystal Chemistry of Perovskite-Type Hydride NaMgH₃: Implications for Hydrogen Storage*. Chemistry of Materials. 2008;20:2335-42.
- [30] Hahn T. *International Tables for Crystallography, Space-Group Symmetry*. Weinheim: Wiley; 2005.
- [31] Klaveness A, Swang O, Fjellvåg H. *Formation enthalpies of NaMgH₃ and KMgH₃: A computational study*. EPL (Europhysics Letters). 2006;76:285.
- [32] Callaway J. *Quantum theory of the solid state*. New York: Academic Press; 1974.
- [33] Corey RB, Pauling L. *Molecular Models of Amino Acids, Peptides, and Proteins*. Review of Scientific Instruments. 1953;24:621-7.
- [34] Reshak AH, Shalaginov MY, Saeed Y, Kityk IV, Auluck S. *First-Principles Calculations of Structural, Elastic, Electronic, and Optical Properties of Perovskite-type KMgH₃ Crystals: Novel Hydrogen Storage Material*. The Journal of Physical Chemistry B. 2011;115:2836-41.
- [35] Bouhadda Y, Kheloufi N, Bentabet A, Boudouma Y, Fenineche N, Benyalloul K. *Thermodynamic functions from lattice dynamic of KMgH₃ for hydrogen storage applications*. Journal of Alloys and Compounds. 2011;509:8994-8.
- [36] Shanes DT, Corey RL, Bowman Jr RC, Zidan R, Stowe AC, Hwang SJ, et al. *NMR studies of the hydrogen storage compound NaMgH₃*. Journal of Physical Chemistry C. 2009;113:18414-9.
- [37] Bertheville B, Herrmannsdörfer T, Yvon K. *Structure data for K₂MgH₄ and Rb₂CaH₄ and comparison with hydride and fluoride analogues*. Journal of Alloys and Compounds. 2001;325:L13-L6.
- [38] Ikeda K, Kogure Y, Nakamori Y, Orimo S. *Reversible hydriding and dehydriding reactions of perovskite-type hydride NaMgH₃*. Scripta Materialia. 2005;53:319-22.

- [39] Komiya K, Morisaku N, Rong R, Takahashi Y, Shinzato Y, Yukawa H, *et al.* *Synthesis and decomposition of perovskite-type hydrides, $MMgH_3$ ($M=Na, K, Rb$).* Journal of Alloys and Compounds. 2008;453:157-60.
- [40] Sheppard DA, Paskevicius M, Buckley CE. *Thermodynamics of Hydrogen Desorption from $NaMgH_3$ and Its Application As a Solar Heat Storage Medium.* Chemistry of Materials. 2011;23:4298-300.
- [41] Reardon H, Mazur N, Gregory DH. *Facile synthesis of nanosized sodium magnesium hydride, $NaMgH_3$.* Progress in Natural Science: Materials International. 2013;23:343-50.
- [42] Ikeda K, Kogure Y, Nakamori Y, Orimo S. *Formation region and hydrogen storage abilities of perovskite-type hydrides.* Progress in Solid State Chemistry. 2007;35:329-37.
- [43] Hohenberg P, Kohn W. *Inhomogeneous Electron Gas.* Physical Review. 1964;136:B864-B71.
- [44] Kohn W, Sham LJ. *Self-Consistent Equations Including Exchange and Correlation Effects.* Physical Review. 1965;140:A1133-A8.
- [45] Xiao XB, Tang BY, Liao SQ, Peng LM, Ding Wj. *Thermodynamic and electronic properties of quaternary hydrides $Li_xNa_{1-x}MgH_3$.* Journal of Alloys and Compounds. 2009;474:522-6.
- [46] Hao S, Sholl DS. *Role of Schottky Defects in Hydrogen and Metal Diffusion in NaH , MgH_2 , and $NaMgH_3$.* The Journal of Physical Chemistry Letters. 2010;1:2968-73.
- [47] Hao S, Sholl DS. *Selection of dopants to enhance hydrogen diffusion rates in MgH_2 and $NaMgH_3$.* Applied Physics Letters. 2009;94.
- [48] Miwa K, Ohba N, Towata S-i, Nakamori Y, Orimo S-i. *First-principles study on lithium borohydride $LiBH_4$.* Physical Review B. 2004;69:245120.
- [49] Du AJ, Smith SC, Yao XD, Lu GQ. *Role of Lithium Vacancies in Accelerating the Dehydrogenation Kinetics on a $LiBH_4(010)$ Surface: An Ab Initio Study.* The Journal of Physical Chemistry C. 2007;111:12124-8.
- [50] Araújo CM, Li S, Ahuja R, Jena P. *Vacancy-mediated hydrogen desorption in $NaAlH_4$.* Physical Review B - Condensed Matter and Materials Physics. 2005;72.
- [51] Majzoub EH, Gross KJ. *Titanium-halide catalyst-precursors in sodium aluminum hydrides.* Journal of Alloys and Compounds. 2003;356-357:363-7.

- [52] Sun D, Kiyobayashi T, Takeshita HT, Kuriyama N, Jensen CM. *X-ray diffraction studies of titanium and zirconium doped NaAlH₄: elucidation of doping induced structural changes and their relationship to enhanced hydrogen storage properties*. Journal of Alloys and Compounds. 2002;337:L8-L11.
- [53] Anton DL. *Hydrogen desorption kinetics in transition metal modified NaAlH₄*. Journal of Alloys and Compounds. 2003;356-357:400-4.
- [54] Song Y, Guo ZX, Yang R. *Influence of selected alloying elements on the stability of magnesium dihydride for hydrogen storage applications: A first-principles investigation*. Physical Review B. 2004;69:094205.
- [55] Vegge T, Hedegaard-Jensen LS, Bonde J, Munter TR, Nørskov JK. *Trends in hydride formation energies for magnesium-3d transition metal alloys*. Journal of Alloys and Compounds. 2005;386:1-7.
- [56] Novaković N, Grbović Novaković J, Matović L, Manasijević M, Radisavljević I, Paskaš Mamula B, *et al.* *Ab initio calculations of MgH₂, MgH₂:Ti and MgH₂:Co compounds*. International Journal of Hydrogen Energy. 2010;35:598-608.
- [57] Tian M, Shang C. *Nano-structured MgH₂ catalyzed by TiC nanoparticles for hydrogen storage*. Journal of Chemical Technology and Biotechnology. 2011;86:69-74.
- [58] Zeng XQ, Cheng LF, Zou JX, Ding WJ, Tian HY, Buckley C. *Influence of 3d transition metals on the stability and electronic structure of MgH₂*. Journal of Applied Physics. 2012;111:093720.
- [59] Hoang K, Janotti A, Van de Walle CG. *Decomposition mechanism and the effects of metal additives on the kinetics of lithium alanate*. Physical Chemistry Chemical Physics. 2012;14:2840-8.
- [60] Kang XD, Wang P, Cheng HM. *In situ formation of Ti hydride and its catalytic effect in doped NaAlH₄ prepared by milling NaH/Al with metallic Ti powder*. International Journal of Hydrogen Energy. 2007;32:2943-8.
- [61] Ismail M, Zhao Y, Yu XB, Dou SX. *Improved hydrogen storage performance of MgH₂-NaAlH₄ composite by addition of TiF₃*. International Journal of Hydrogen Energy. 2012;37:8395-401.
- [62] Suttisawat Y, Rangsunvigit P, Kitiyanan B, Kulprathipanja S. *Effect of co-dopants on hydrogen desorption/absorption of HfCl₄- and TiO₂-doped NaAlH₄*. International Journal of Hydrogen Energy. 2008;33:6195-200.

- [63] Kang X, Wang P, Cheng H. *Impact of preparation conditions on hydrogen storage performance of metallic Ti-doped NaAlH₄*. Rare Metals. 2006;25:266-72.
- [64] Akinori T, Hiroshi O, Tamio I. *First-principles study of hydrogen vacancies in sodium alanate with Ti substitution*. Journal of Physics: Condensed Matter. 2010;22:205503.
- [65] Wang P, Kang XD, Cheng HM. *Dependence of H-storage performance on preparation conditions in TiF₃ doped NaAlH₄*. Journal of Alloys and Compounds. 2006;421:217-22.
- [66] Weidenthaler C, Pommerin A, Felderhoff M, Bogdanovic B, Schuth F. *On the state of the titanium and zirconium in Ti- or Zr-doped NaAlH₄ hydrogen storage material*. Physical Chemistry Chemical Physics. 2003;5:5149-53.
- [67] Wang P, Jensen CM. *Preparation of Ti-Doped Sodium Aluminum Hydride from Mechanical Milling of NaH/Al with Off-the-Shelf Ti Powder*. The Journal of Physical Chemistry B. 2004;108:15827-9.
- [68] Wang J, Ebner AD, Zidan R, Ritter JA. *Synergistic effects of co-dopants on the dehydrogenation kinetics of sodium aluminum hydride*. Journal of Alloys and Compounds. 2005;391:245-55.
- [69] Du J, Wang Z, Niu Y, Huang T, Li Z, et al. *Strain variation on the reaction tank of high hydrogen content during hydrogen absorption-desorption cycles*. International Journal of Hydrogen Energy. 2013;38:2347-51.
- [70] Jorge Jr AM, Prokofiev E, Ferreira de Lima G, Rauch E, Veron M, Botta WJ, et al. *An investigation of hydrogen storage in a magnesium-based alloy processed by equal-channel angular pressing*. International Journal of Hydrogen Energy. 2013;38:8306-12.
- [71] Surya VJ, Iyakutti K, Mizuseki H, Kawazoe Y. *Modification of graphene as active hydrogen storage medium by strain engineering*. Computational Materials Science. 2012;65:144-8.
- [72] Tang J-J, Yang X-B, Chen M, Zhu M, Zhao Y-J. *First-Principles Study of Biaxial Strain Effect on Hydrogen Adsorbed Mg(0001) Surface*. The Journal of Physical Chemistry C. 2012;116:14943-9.
- [73] Gandia LM, Arzamedi G, Dieguez PM. *Renewable Hydrogen Technologies: Production, Purification, Storage, Applications and Safety*: Elsevier Science; 2013.
- [74] Graetz J. *New approaches to hydrogen storage*. Chemical Society Reviews. 2009;38:73-82.

- [75] Jain IP, Jain P, Jain A. *Novel hydrogen storage materials: A review of lightweight complex hydrides*. Journal of Alloys and Compounds. 2010;503:303-39.
- [76] Wang Q, Chen Y, Wu C, Tao M. *Catalytic effect and reaction mechanism of Ti doped in NaAlH₄: A review*. Chin Sci Bull. 2008;53:1784-8.
- [77] Chen M, Cai Z-Z, Yang X-B, Zhu M, Zhao Y-J. *Theoretical study of hydrogen dissociation and diffusion on Nb and Ni co-doped Mg(0001): A synergistic effect*. Surface Science. 2012;606:L45-L9.
- [78] Wang L-L, Johnson DD. *Hydrogen Desorption from Ti-Doped MgH₂(110) Surfaces: Catalytic Effect on Reaction Pathways and Kinetic Barriers*. The Journal of Physical Chemistry C. 2012;116:7874-8.
- [79] Reich JM, Wang L-L, Johnson DD. *Surface and Particle-Size Effects on Hydrogen Desorption from Catalyst-Doped MgH₂*. The Journal of Physical Chemistry C. 2012;116:20315-20.
- [80] Pozzo M, Alfè D. *Dehydrogenation of pure and Ti-doped Na₃AlH₆ surfaces from first principles calculations*. International Journal of Hydrogen Energy. 2011;36:15632-41.
- [81] Wu G, Zhang J, Li Q, Wu Y, Chou K, Bao X. *Dehydrogenation kinetics of magnesium hydride investigated by DFT and experiment*. Computational Materials Science. 2010;49:S144-S9.
- [82] Tsuda M, Agerico Diño W, Nakanishi H, Kasai H. *Ab Initio Study of H₂ Desorption from Magnesium Hydride MgH₂ Cluster*. Journal of the Physical Society of Japan. 2004;73:2628-30.
- [83] Du AJ, Smith SC, Yao XD, Lu GQ. *Ab initio studies of hydrogen desorption from low index magnesium hydride surface*. Surface Science. 2006;600:1854-9.
- [84] Hanada N, Ichikawa T, Fujii H. *Catalytic Effect of Nanoparticle 3d-Transition Metals on Hydrogen Storage Properties in Magnesium Hydride MgH₂ Prepared by Mechanical Milling*. The Journal of Physical Chemistry B. 2005;109:7188-94.
- [85] Hanada N, Ichikawa T, Isobe S, Nakagawa T, Tokoyoda K, Honma T, et al. *X-ray Absorption Spectroscopic Study on Valence State and Local Atomic Structure of Transition Metal Oxides Doped in MgH₂*. The Journal of Physical Chemistry C. 2009;113:13450-5.
- [86] Li S, Jena P, Ahuja R. *Effect of Ti and metal vacancies on the electronic structure, stability, and dehydrogenation of Na₃AlH₆: Supercell band-structure formalism and gradient-corrected density-functional theory*. Physical Review B. 2006;73:214107.

- [87] Dai JH, Song Y, Yang R. *Intrinsic mechanisms on enhancement of hydrogen desorption from MgH₂ by (001) surface doping*. International Journal of Hydrogen Energy. 2011;36:12939-49.
- [88] Meunier M. *Industrial Applications of Molecular Simulations*. Boca Raton: CRC Press; 2012.
- [89] LeSar R. *Introduction to Computational Materials Science: Fundamentals to Applications*. New York: Cambridge University Press; 2013.
- [90] Rai B. *Molecular Modeling for the Design of Novel Performance Chemicals and Materials*. Boca Raton: CRC Press; 2012.
- [91] Segall MD, Lindan PJD, Probert MJ, Pickard CJ, Hasnip PJ, Clark SJ, et al. *First-principles simulation: ideas, illustrations and the CASTEP code*. Journal of Physics: Condensed Matter. 2002;14:2717-44.
- [92] Milman V, Refson K, Clark SJ, Pickard CJ, Yates JR, Gao SP, et al. *Electron and vibrational spectroscopies using DFT, plane waves and pseudopotentials: CASTEP implementation*. Journal of Molecular Structure: THEOCHEM. 2010;954:22-35.
- [93] Delley B. *From molecules to solids with the DMol³ approach*. The Journal of Chemical Physics. 2000;113:7756-64.
- [94] Delley B. *An all-electron numerical method for solving the local density functional for polyatomic molecules*. The Journal of Chemical Physics. 1990;92:508-17.
- [95] Lusk MT, Mattsson AE. *High-performance computing for materials design to advance energy science*. MRS Bulletin. 2011;36:169-74.
- [96] Kohanoff J. *Electronic structure calculations for solids and molecules*. New York: Cambridge University Press; 2006.
- [97] Lieb EH, Simon B. *The Thomas-Fermi Theory of atoms, molecules and solids*. Advances in Mathematics. 1977; 23:22-116.
- [98] Thomas LH. *The calculation of atomic fields*. Mathematical Proceedings of the Cambridge Philosophical Society. 1927;23:542-8.
- [99] O'Regan DD. *Optimised Projections for the Ab Initio Simulation of Large and Strongly Correlated Systems*. New York: Springer; 2011.
- [100] Brázdová V, Bowler DR. *Atomistic Computer Simulations: A Practical Guide*. Weinheim: Wiley-VCH; 2013.

- [101] Sokalski WA. *Molecular Materials with Specific Interactions - Modeling and Design: Modeling and Design*. Dordrecht: Springer London, Limited; 2007.
- [102] Kaxiras E. *Atomic and Electronic Structure of Solids*. New York: Cambridge University Press; 2003.
- [103] Levy M. *Universal variational functionals of electron densities, first-order density matrices, and natural spin-orbitals and solution of the v -representability problem*. Proceedings of the National Academy of Sciences. 1979;76:6062-5.
- [104] Levy M. *Electron densities in search of Hamiltonians*. Physical Review A. 1982;26:1200-8.
- [105] Sholl D, Steckel JA. *Density Functional Theory: A Practical Introduction*. Hoboken: Wiley; 2011.
- [106] Lee JG. *Computational Materials Science: An Introduction*. Boca Raton: CRC Pr, Taylor & Francis; 2011.
- [107] Lewars E. *Computational Chemistry: Introduction to the Theory and Applications of Molecular and Quantum Mechanics*. Dordrecht: Springer; 2003.
- [108] Ramachandran KI, Deepa G, Namboori K. *Computational Chemistry and Molecular Modeling: Principles and Applications*. New York: Springer; 2008.
- [109] Perdew JP, Schmidt K. *Jacob's ladder of density functional approximations for the exchange-correlation energy*. AIP Conference Proceedings. 2001;577:1-20.
- [110] Shevlin SA, Guo ZX. *Density functional theory simulations of complex hydride and carbon-based hydrogen storage materials*. Chemical Society Reviews. 2009;38:211-25.
- [111] Vosko SH, Wilk L, Nusair M. *Accurate spin-dependent electron liquid correlation energies for local spin density calculations: a critical analysis*. Canadian Journal of Physics. 1980;58:1200-11.
- [112] Perdew JP, Wang Y. *Accurate and simple analytic representation of the electron-gas correlation energy*. Physical Review B. 1992;45:13244-9.
- [113] Gunnarsson O, Jones RO. *Density Functional Calculations for Atoms, Molecules and Clusters*. Physica Scripta. 1980;21:394.
- [114] Perdew JP, Burke K, Ernzerhof M. *Generalized Gradient Approximation Made Simple*. Physical Review Letters. 1996;77:3865-8.

- [115] Politzer P, Seminario JM. *Density Functional Theory: A Tool for Chemistry*. Amsterdam: Elsevier; 1995.
- [116] Ziegler T. *Approximate density functional theory as a practical tool in molecular energetics and dynamics*. Chemical Reviews. 1991;91:651–67.
- [117] Becke AD. *Density-functional exchange-energy approximation with correct asymptotic behavior*. Physical Review A. 1988;38:3098-100.
- [118] Hofmann P. *Surface Physics: An Introduction*. Weinheim: Wiley-VCH; 2013.
- [119] Kasap SO. *Principles of Electronic Materials and Devices*. New York: McGraw-Hill; 2006.
- [120] Ghouri MM, University LT. *A Computational Study on Novel Carbon-based Lithium Materials for Hydrogen Storage and the Role of Carbon in Destabilizing Complex Metal Hydride*. Ruston: Louisiana Tech University; 2009.
- [121] Vanderbilt D. *Soft self-consistent pseudopotentials in a generalized eigenvalue formalism*. Physical Review B. 1990;41:7892-5.
- [122] Payne MC, Teter MP, Allan DC, Arias TA, Joannopoulos JD. *Iterative minimisation techniques for ab initio total-energy calculations: molecular dynamics and conjugate gradients*. Reviews of Modern Physics. 1992;64:1045-97.
- [123] Pack JD, Monkhorst HJ. *"Special points for Brillouin-zone integrations"—a reply*. Physical Review B. 1977;16:1748-9.
- [124] Wiesendanger R. *Scanning Probe Microscopy: Analytical Methods*. New York: Springer; 1998.
- [125] Hirshfeld FL. *Bonded-atom fragments for describing molecular charge densities*. Theoret Chim Acta. 1977;44:129-38.
- [126] Mulliken RS. *Electronic population analysis on LCAO-MO molecular wave functions*. Journal of Chemical Physics. 1955;10:1833-40.
- [127] Sanchez-Portal D, Artacho E, Soler JM. *Projection of plane-wave calculations into atomic orbitals*. Solid State Communications. 1995;95:685-90.
- [128] Demtröder W. *Molecular Physics*. Weinheim: Wiley-VCH; 2008.
- [129] Kittel C. *Introduction to Solid State Physics*. Fifth ed. Weinheim: Wiley; 1976.
- [130] Ashcroft NW, Mermin ND. *Solid State Physics*. Philadelphia: Holt, Rinehart and Winston; 1976.

- [131] Clark SJ, Segall MD, Pickard CJ, Hasnip PJ, Probert MIJ, Refson K, *et al.* *First principles methods using CASTEP*. Zeitschrift für Kristallographie - Crystalline Materials. 2005;220:567-70.
- [132] Wu Z, Cohen RE. *More accurate generalized gradient approximation for solids*. Physical Review B. 2006;73:235116.
- [133] Tran F, Laskowski R, Blaha P, Schwarz K. *Performance on molecules, surfaces, and solids of the Wu-Cohen GGA exchange-correlation energy functional*. Physical Review B. 2007;75:115131.
- [134] Paier J, Hirschl R, Marsman M, Kresse G. *The Perdew--Burke--Ernzerhof exchange-correlation functional applied to the G2-1 test set using a plane-wave basis set*. The Journal of Chemical Physics. 2005;122:234102-13.
- [135] Head JD, Zerner MC. *A Broyden-Fletcher-Goldfarb-Shanno optimization procedure for molecular geometries*. Chemical Physics Letters. 1985;122:264-70.
- [136] Fonseca Guerra C, Handgraaf J-W, Baerends EJ, Bickelhaupt FM. *Voronoi deformation density (VDD) charges: Assessment of the Mulliken, Bader, Hirshfeld, Weinhold, and VDD methods for charge analysis*. Journal of Computational Chemistry. 2004;25:189-210.
- [137] Mulliken RS. *Electronic Population Analysis on LCAO-MO Molecular Wave Functions. II. Overlap Populations, Bond Orders, and Covalent Bond Energies*. The Journal of Chemical Physics. 1955;23:1841-6.
- [138] Du AJ, Smith SC, Lu GQ. *Role of charge in destabilizing AlH_4 and BH_4 complex anions for hydrogen storage applications: Ab initio density functional calculations*. Physical Review B. 2006;74:1934051-4.
- [139] Moysés Araújo C, Li S, Ahuja R, Jena P. *Vacancy-mediated hydrogen desorption in $NaAlH_4$* . Physical Review B. 2005;72:165101-6.
- [140] Lee EK, Cho YW, Yoon JK. *Ab-initio calculations of titanium solubility in $NaAlH_4$ and Na_3AlH_6* . Journal of Alloys and Compounds. 2006;416:245-9.
- [141] Liu J, Ge Q. *A First-Principles Analysis of Hydrogen Interaction in Ti-Doped $NaAlH_4$ Surfaces: Structure and Energetics*. Journal of Physical Chemistry B. 2006;110:25863-8.
- [142] Arroyo y de Dompablo ME, Ceder G. *First principles investigations of complex hydrides AMH_4 and A_3MH_6 ($A=Li, Na, K, M=B, Al, Ga$) as hydrogen storage systems*. Journal of Alloys and Compounds. 2004;364:6-12.

- [143] Løvvik OM, Opalka SM. *Density functional calculations of Ti-enhanced NaAlH₄*. Physical Review B. 2005;71: 1-10.
- [144] Chaudhuri S, Graetz J, Ignatov A, Reilly JJ, Muckerman JT. *Understanding the Role of Ti in Reversible Hydrogen Storage as Sodium Alanate: A Combined Experimental and Density Functional Theoretical Approach*. Journal of American Chemical Society. 2006;128:11404-15.
- [145] Chaudhuri S, Muckerman JT. *First-Principles Study of Ti-Catalyzed Hydrogen Chemisorption on an Al Surface: A Critical First Step for Reversible Hydrogen Storage in NaAlH₄*. Journal of Physical Chemistry B. 2005;109:6952-7.
- [146] Li S, Jena P, Ahuja R. *Effect of Ti and metal vacancies on the electronic structure, stability, and dehydrogenation of Na₃AlH₆: Supercell band-structure formalism and gradient-corrected density-functional theory*. Physical Review B. 2006;73:2141071-7.
- [147] Ozolins V, Majzoub EH, Udovic TJ. *Electronic Structure and Rietveld Refinement Parameters of Ti-doped Sodium Alanates*. Journal of Alloys and Compounds. 2004;375:1-10.
- [148] Vegge T. *Equilibrium structure and Ti-catalyzed H₂ desorption in NaAlH₄ nanoparticles from density functional theory*. Physical Chemistry Chemical Physics. 2006;8:4853–61.
- [149] Montanari B, Harrison NM. *Lattice dynamics of TiO₂ rutile: influence of gradient corrections in density functional calculations*. Chemical Physics Letters. 2002;364:528-34.
- [150] Klaveness A, Fjellvåg H, Kjekshus A, Ravindran P, Swang O. *A semi-empirical approach to accurate standard enthalpies of formation for solid hydrides*. Journal of Alloys and Compounds. 2009;469:617-22.
- [151] Felderhoff M, Klementiev K, Grunert W, Spliethoff B, Tesche B, Bellosta von Colbe JM, et al. *Combined TEM-EDX and XAFS studies of Ti-doped sodium alanate*. Physical Chemistry Chemical Physics. 2004;6:4369-74.
- [152] Zhang J, Zhou YC, Ma ZS, Sun LQ, Peng P. *Strain effect on structural and dehydrogenation properties of MgH₂ hydride from first-principles calculations*. International Journal of Hydrogen Energy. 2013;38:3661-9.
- [153] Tanveer H, Abir De S, Tuhina Adit M, Weiwei S, Rajeev A. *Strain and doping effects on the energetics of hydrogen desorption from the MgH₂ (001) surface*. EPL (Europhysics Letters). 2013;101:27006.

- [154] Ehrenson S. *Analysis of least motion paths for molecular deformations*. Journal of the American Chemical Society. 1974;96:3778-84.
- [155] Govind N, Petersen M, Fitzgerald G, King-Smith D, Andzelm J. *A generalized synchronous transit method for transition state location*. Computational Materials Science. 2003;28:250-8.
- [156] Tutuianu M. *Quantum Mechanical Modeling of Surface Reactions in Storage Catalytic Converters*. Heidelberg: Rupertus-Carola University; 2007.
- [157] Arias T, Payne MC, Joannopoulos JD. *Ab initio molecular dynamics: Analytically continued energy functionals and insights into iterative solutions*. Physical Review Letters. 1992;69:1077-80.
- [158] Alfe D. *Ab initio molecular dynamics, a simple algorithm for charge extrapolation*. Computational Physics Communications. 1999;118:31-3.
- [159] Marx D, Hutter J. *Ab Initio Molecular Dynamics: Basic Theory and Advanced Methods*. New York: Cambridge University Press; 2009.
- [160] Nosé S. *A molecular dynamics method for simulations in the canonical ensemble*. Molecular Physics. 1984;52:255-68.
- [161] Rönnebro E, Noréus D, Kadir K, Reiser A, Bogdanovic B. *Investigation of the perovskite related structures of NaMgH₃, NaMgF₃ and Na₃AlH₆*. Journal of Alloys and Compounds. 2000;299:101-6.
- [162] Bouamrane A, Laval JP, Soulie JP, Bastide JP. *Structural characterization of NaMgH₂F and NaMgH₃*. Materials Research Bulletin. 2000;35:545-9.
- [163] Machayekhi B, Chevallier J, Theys B, Besson JM, Weill G, Syfosse G. *Influence of hydrostatic pressure on the diffusion of hydrogen in n-GaAs: Si*. Solid State Communications. 1996;100:821-4.
- [164] Lozano GA, Bellosta von Colbe JM, Bormann R, Klassen T, Dornheim M. *Enhanced volumetric hydrogen density in sodium alanate by compaction*. Journal of Power sources. 2011;196:9254-9.
- [165] Bouhadda Y, Fenineche N, Boudouma Y. *Hydrogen storage: Lattice dynamics of orthorhombic NaMgH₃*. Physica B: Condensed Matter. 2011;406:1000-3.
- [166] Dathar GKP, University LT. *Computational Study of Pristine and Titanium-doped Sodium Alanates for Hydrogen Storage Applications*. Ruston: Louisiana Tech University; 2009.

- [167] Klaveness A, Swang O, Fjellvag H. *Formation enthalpies of NaMgH₃ and KMgH₃: A computational study*. Europhysics Letters. 2006;76:285-90.
- [168] Batalovic K, Radakovic J, Belosevic-Cavor J, Koteski V. *Transition metal doping of Mg₂FeH₆ - a DFT insight into synthesis and electronic structure*. Physical Chemistry Chemical Physics. 2014;16:12356-61.
- [169] Bouhadda Y, Bououdina M, Fenineche N, Boudouma Y. *Elastic properties of perovskite-type hydride NaMgH₃ for hydrogen storage*. International Journal of Hydrogen Energy. 2013;38:1484-9.
- [170] Patil SKR, Khare SV, Tuttle BR, Bording JK, Kodambaka S. *Mechanical stability of possible structures of PtN investigated using first-principles calculations*. Physical Review B. 2006;73:104118.
- [171] Baroni S, de Gironcoli S, Dal Corso A, Giannozzi P. *Phonons and related crystal properties from density-functional perturbation theory*. Reviews of Modern Physics. 2001;73:515-62.
- [172] Man C-S, Huang M. *A Simple Explicit Formula for the Voigt-Reuss-Hill Average of Elastic Polycrystals with Arbitrary Crystal and Texture Symmetries*. J Elast. 2011;105:29-48.
- [173] Vajeeston P, Ravindran P, Kjekshus A, Fjellvåg H. *First-principles investigations of the MMgH₃ (Na, K, Rb, Cs) series*. Journal of Alloys and Compounds. 2008;450:327-37.
- [174] Uesugi T, Takigawa Y, Higashi K. *Elastic constants of AlLi from first principles*. Materials transactions. 2005;46:1117.
- [175] Zhai H, Li X, Du J. *First-Principles Calculations on Elasticity and Anisotropy of Tetragonal Tungsten Dinitride under Pressure*. Materials transactions. 2012;53:1247-51.
- [176] Pedicini R, Schiavo B, Rispoli P, Saccà A, Carbone A, Gatto I, et al. *Progress in polymeric material for hydrogen storage application in middle conditions*. Energy. 2014;64:607-14.
- [177] Majzoub EH, Zhou F, Ozoliņš V. *First-Principles Calculated Phase Diagram for Nanoclusters in the Na–Al–H System: A Single-Step Decomposition Pathway for NaAlH₄*. The Journal of Physical Chemistry C. 2011;115:2636-43.
- [178] Qian Z, Hudson MSL, Raghubanshi H, Scheicher RH, Pathak B, Araújo CM, et al. *Excellent Catalytic Effects of Graphene Nanofibers on Hydrogen Release of Sodium alanate*. The Journal of Physical Chemistry C. 2012;116:10861-6.

- [179] Xu L, Ge Q. *Effect of defects and dopants in graphene on hydrogen interaction in graphene-supported NaAlH₄*. International Journal of Hydrogen Energy. 2013;38:3670-80.